

# **Transverse Isotropic Multiscale Muscle Phantom for MR Elastography**

BY

MARTINA GUIDETTI

B.S., Politecnico di Milano, Milan, Italy, 2014

M.S., Politecnico di Milano, Milan, Italy, 2016

THESIS

Submitted as partial fulfillment of the requirements  
for the degree of Master of Science in Bioengineering  
in the Graduate College of the  
University of Illinois at Chicago, 2017

Chicago, Illinois

Defense Committee:

Thomas J. Royston, Chair and Advisor  
Dieter Klatt  
Pasquale Vena, Politecnico di Milano

To Marco

## ACKNOWLEDGMENTS

First and foremost, I would like to express my sincere gratitude to Prof. Thomas J. Royston for bringing me into the world of MRE and always motivating me to do my best.

Moreover, I want to thank Prof. Pasquale Vena for his constant guidance and support throughout my master thesis.

My deepest gratitude goes to Prof. Dieter Klatt for his valuable insight, instructive comments and suggestions in MRE field.

Many thanks to Harish Palnitkar, Altaf Khan, Brian Henry, Kaya T. Yasar and the whole Acoustics and Vibrations Laboratory (UIC) for their indications and suggestions on the experimental and computational procedures.

The financial support of the National Institutes of Health (Grant # AR071162) is acknowledged.

Thanks to Antonio for being the person he has become to me.

Finally, my utmost gratitude goes to my parents for their moral and practical support during my whole academic career helping me in overcoming the setbacks and adversities during these years through their optimism.

MG

## TABLE OF CONTENTS

<b><u>CHAPTER</u></b>	<b><u>PAGE</u></b>
<b>1. INTRODUCTION .....</b>	<b>1</b>
<b>2. MAGNETIC RESONANCE ELASTOGRAPHY (MRE) .....</b>	<b>5</b>
2.1 Steps in MRE .....	5
2.1.1 Excitation.....	5
2.1.2 Wave images acquisition .....	6
2.1.3 Shear modulus estimation.....	11
<b>3. ANATOMY AND PHYSIOLOGY OF SKELETAL MUSCLE .....</b>	<b>12</b>
3.1 Anisotropy and fractal structure of skeletal muscle.....	12
3.2 Fibers and sarcomeres .....	13
3.3 Muscle proteins .....	14
3.3.1 Mechanical behavior.....	15
<b>4. MECHANICAL WAVES AND INVERSE AND DIRECT PROBLEMS IN MRE.....</b>	<b>17</b>
4.1 Longitudinal and transverse waves .....	18
4.2 Introduction to the inverse problem .....	19
4.3 Equation of motion for an isotropic linear continuum.....	20
4.3.1 Scalar Helmholtz inversion .....	22
4.3.2 Algebraic Inversion of the Differentia Equations (AIDE) .....	22
4.3.3 Limitations of inversion algorithms .....	24
4.4 Wave equation for an anisotropic viscoelastic medium .....	24
4.5 Direct problem, continuum formulation .....	29
<b>5. VISCOELASTIC RHEOLOGICAL MODELS.....</b>	<b>30</b>
5.1 Basic rheological elements .....	30
5.2 Complex modulus estimation for some linear viscoelastic models .....	31
5.2.1 Maxwell model .....	32
5.2.2 Voigt model .....	33
5.3 Fractional viscoelasticity and springpot model.....	34
5.3.1 Fractional Voigt model .....	37

## TABLE OF CONTENTS (continued)

<b>6.</b>	<b>MATERIALS AND METHODS.....</b>	<b>38</b>
6.1	Sample preparation .....	38
6.1.1	Internal phantom construction for anisotropic sample .....	38
6.1.2	External matrix construction for anisotropic sample.....	39
6.1.3	Assembling of the external matrix with the internal phantom .....	39
6.2	Electro-mechanical setup and mechanical actuation .....	41
6.3	Computational simulation of MRE experiments .....	45
<b>7.</b>	<b>RESULTS AND DISCUSSION.....</b>	<b>49</b>
7.1	Homogeneous and isotropic gelatin.....	49
7.2	Homogeneous and isotropic PVA.....	55
7.3	Spandex fibers.....	61
7.4	Transverse isotropic phantom with 4 fibers.....	62
7.5	Transverse isotropic phantom with higher number of fibers .....	66
7.6	Transverse isotropic phantom with high number of fibers .....	72
<b>8.</b>	<b>CONCLUSION AND FUTURE DEVELOPMENTS .....</b>	<b>78</b>
	<b>CITED LITERATURE .....</b>	<b>81</b>
	<b>VITA .....</b>	<b>86</b>

## LIST OF TABLES

<u>TABLE</u>	<u>PAGE</u>
I: CONSTITUTIVE EQUATIONS DESCRIBING STRESS-STRAIN RELATIONS OF ELEMENTARY VISCOELASTIC MODELS WHERE $E$ AND $\eta$ ARE RESPECTIVELY THE ELASTICITY CONSTANT AND THE DAMPING COEFFICIENT. ....	30
II: SUMMATION RULES IN LINEAR VISCOELASTICITY TO FORM COMPLEX MODELS COMPOSING THE SUB-RHEOLOGICAL ELEMENTS. $\sigma_K$ AND $\varepsilon_K$ ARE RESPECTIVELY THE STRESS AND THE STRAIN OF SUB- RHEOLOGICAL ELEMENTS.....	32
III: SETTING PARAMETERS FOR MRE EXPERIMENT.....	42
IV:COMPARISON BETWEEN COMPUTATIONAL (ON THE LEFT) AND EXPERIMENTAL (ON THE RIGHT) WAVE IMAGES FOR HOMOGENEOUS AND ISOTROPIC GELATIN. ....	53
V:COMPARISON BETWEEN COMPUTATIONAL (ON THE LEFT) AND EXPERIMENTAL (ON THE RIGHT) WAVE IMAGES FOR HOMOGENEOUS AND ISOTROPIC GELATIN. ....	59
VI:COMPARISON BETWEEN COMPUTATIONAL (ON THE LEFT) AND EXPERIMENTAL (ON THE RIGHT) WAVE IMAGES FOR ANISOTROPIC PHANTOM WITH 4 FIBERS. ....	63
VII: COMPUTATIONAL WAVE IMAGES FOR ANISOTROPIC PHANTOM WITH INTERMEDIATE NUMBER OF FIBERS.....	69
VIII: COMPUTATIONAL WAVE IMAGES FOR ANISOTROPIC PHANTOM WITH HIGH NUMBER OF FIBERS. ....	74

## LIST OF FIGURES

<b><u>FIGURE</u></b>	<b><u>PAGE</u></b>
1: Experimental setup used for transmitting geometrically-focused shear waves for MRE.....	2
2: Schematic diagram of steps in magnetic resonance elastography. Provided by Prof Dieter Klatt. ....	5
3: Synchronization of MEG with mechanical excitation signal. ....	7
4: The direction of the MEG defines the direction along which the component of the displacement of voxels is measured. ....	7
5: Representation of $M_t$ , transverse magnetization (MR signal), in presence of external main magnetic field $B_0$ parallel to z-axis. ....	9
6: Visualization of some voxels displacement in the ROI. In a single voxel spins are assumed to be stationary so that they vibrate with the same phase. ....	10
7: Hierarchical levels in skeletal muscle tissue. "Skeletal muscle" photo montage created by Raul654 and Rama, licensed under PD-USGov, GFDL. ....	13
8: Tension developed by a sarcomere with respect to the length of the sarcomere. ....	15
9: Ideal experiments to quantify the shear moduli of a transverse isotropic material having fibers in $x_3$ direction: the planes of symmetry are about $x_3$ axis and the plane of isotropy is in $x_1$ - $x_2$ plane. First two experiments allow for the evaluation of $\mu_{  }$ , while the third returns $\mu_{\perp}$ . ....	27
10: Maxwell Model. ....	32
11: Voigt Model. ....	33
12: Springpot model (single fractional element). ....	34

13: The Springpot model can be seen as an element whose behavior approaches a spring or a dashpot for $\alpha$ that respectively goes to 0 or to 1. ....	35
14: The parameters $\mu\alpha$ (viscoelastic connectivity) and $\alpha$ (matrix geometry) of the Springpot model can be seen as describing the structural properties of the material: while $\mu\alpha$ is akin to an ordinary stiffness, $\alpha$ describes the matrix geometry: values of $\alpha$ closer to 1 indicate a more organized and structured material. Provided by Ingolf Sack. ....	36
15: Fractional Voigt model. ....	37
16: Picture of the anisotropic phantom inside the test tube. Externally the transparent gelatin matrix, inside the PVA matrix with four Spandex fibers inside positioned horizontally. ....	40
17: Schematization of the model for anisotropic phantom reported in Figure 16. Externally the transparent gelatin matrix, inside the PVA matrix with four Spandex fibers inside positioned horizontally. ....	40
18: Exemplificative example in which geometrical focusing phenomenon is visible. ....	43
19: Screenshot of MRE deviant software for MRE experiments postprocessing in which 8 line profiles crossing the center spaced of $22.5^\circ$ are taken [49]. ....	44
20: Model of an axisymmetric cylinder with radius of 4 mm for homogeneous isotropic gelatin. ....	46
21: Mesh of 10324 triangular elements with 5304 vertices for model of an axisymmetric cylinder with radius of 4 mm for homogeneous isotropic gel. ....	46
22: 3D model for anisotropic phantom with four fibers. ....	47
23: Mesh of 1131198 tetrahedral and 53112 triangular elements for anisotropic phantom with four fibers. ....	48
24: Experimental displacement profiles for homogeneous and isotropic gelatin in direction perpendicular to the slice plane along the diameter of the test tube. ....	49



25: Identified values of $\mu_R$ and $\mu_I$ versus frequency for homogeneous and isotropic gelatin (see section 6.2). .....	50
26: Curve fitting of the experimental data of $\mu_R$ for homogeneous and isotropic gelatin with a parabolic curve. ....	51
27: Curve fitting of the experimental data of $\mu_I$ for homogeneous and isotropic gelatin with a parabolic curve. ....	51
28: Computational displacement profiles for homogeneous and isotropic gelatin in direction perpendicular to the slice plane along the radius of the test tube. ....	55
29: Experimental displacement profiles for homogeneous and isotropic PVA in direction perpendicular to the slice plane along the diameter of the test tube. ....	56
30: $\mu_R$ and $\mu_I$ curves in function of frequency for homogeneous and isotropic PVA. ....	56
31: Curve fitting of the experimental data of $\mu_R$ for homogeneous and isotropic PVA with a parabolic curve. ....	57
32: Curve fitting of the experimental data of $\mu_I$ for homogeneous and isotropic PVA with a parabolic curve. ....	57
33: Computational displacement profiles for homogeneous and isotropic PVA in direction perpendicular to the slice plane along the radius of the test tube. ....	61
34: Stress-strain plot for Spandex fibers. ....	61
35: MRI slice of anisotropic phantom with 4 fibers taken in order to see the position of the fibers. ....	62
36: Computational displacement profiles in direction perpendicular to the slice plane along the diameter of the test tube for anisotropic phantom with 4 fibers (direction parallel to fibers). ....	65

37: Computational displacement profiles in direction perpendicular to the slice plane along the diameter of the test tube for anisotropic phantom with 4 fibers (direction perpendicular to fibers).....	66
38: 3D model of the anisotropic phantom with an intermediate number of fibers. ....	67
39: Mesh of the 3D model for the anisotropic phantom with an intermediate number of fibers.....	68
40: Computational displacement profiles in direction perpendicular to the slice plane along the diameter of the test tube for anisotropic phantom with intermediate number of fibers (direction perpendicular to fibers). ....	71
41: Computational displacement profiles in direction perpendicular to the slice plane along the diameter of the test tube for anisotropic phantom with intermediate number of fibers (direction parallel to fibers). ....	71
42: 3D model of the anisotropic phantom with high number of fibers.....	72
43: Mesh of the 3D model for the anisotropic phantom with high number of fibers. ....	73
44: Computational displacement profiles in direction perpendicular to the slice plane along the diameter of the test tube for anisotropic phantom with high number of fibers (direction perpendicular to fibers). ....	76
45: Computational displacement profiles in direction perpendicular to the slice plane along the diameter of the test tube for anisotropic phantom with high number of fibers (direction parallel to fibers). ....	76

## **LIST OF ABBREVIATIONS**

MRE	Magnetic Resonance Elastography
MRI	Magnetic Resonance Imaging
FE	Finite Element
MEG	Motion Encoding Gradient
ROI	Region Of Interest
DOF	Degree Of freedom

## SUMMARY

Magnetic Resonance Elastography (MRE) is a noninvasive imaging technique employed to assess biological tissues properties (shear stiffness) by inducing mechanical wave propagation in the region of interest.

For skeletal muscles, an abnormal stiffness indicates various diseases like spasticity, Duchenne muscular dystrophy and hyperthyroidism. Thus, muscle mechanical properties characterization becomes fundamental to a better understanding of the mechanisms accountable for muscle adaptation and the function of muscle, potentially allowing one to follow treatment effects in time. The challenge in employing MRE on muscular tissue is to characterize a non-homogeneous, viscoelastic, and anisotropic material through an inversion algorithm based on the underlying equations of wave motion, so as to obtain distribution of the shear stiffness of the material from the map of its displacement fields.

The chosen approach to improve MRE data acquisition protocols is to develop phantoms that realistically simulate properties of soft tissues. This work deals with the optimization of the mechanical and geometrical properties of a phantom that has to show both viscoelastic and anisotropic characteristics similar to those of skeletal muscle when subject to a MRE experiment.

A phantom with known and controllable anisotropic viscoelastic properties similar to striated skeletal muscle is developed using a polyvinyl alcohol (PVA) solution 10% w/v in which are positioned four fibers made of Spandex. Then this phantom is immersed in gelatin solution 10% w/v and put in a test tube for MRE multi-frequency experiments.

A finite element (FE) model of the same phantom is realized in Solidworks and imported into Comsol Multiphysics in order to simulate a virtual MRE experiment and then compare the experimental results with the computational ones. Once the FE model has been validated, it can be used to rapidly simulate more complex structures that are closer in design to striated muscle. The simulations can elucidate the relationship between the multiscale geometric features of muscle and its relevant macroscopic viscoelastic and anisotropic properties as detected through the MRE technique.

# CHAPTER 1

## INTRODUCTION

As the macroscopic mechanical properties of a biological tissue are sensitive to changes of their micro-structural and compositional properties brought on by injury and disease, measurement of these macroscopic properties can be used to detect altered pathological states, for instance fibrosis, inflammation, malignancies or tissue breakdown associated with degenerative diseases, or to monitor response to therapy[1].

The use of mechanical properties as parameter for diagnosis has been developed from the traditional practice of palpation, a diagnostic tool used to assess the presence of stiffer areas in the felt tissue.

Despite its high sensitivity due to the wide range of values (more than eight orders of magnitude) of the shear stiffness in body tissues, palpation can be only performed on superficial organs, and also has the limits of being a qualitative, subjective and highly operator dependent technique [2] .

Dynamic elastographic imaging methods were introduced as a mean to map the inhomogeneous spatial distribution of tissue stiffness. The most recent advances of elastography-based techniques allow assessment of shear stiffness of the tissue and its spatial distribution. This has been achieved utilizing magnetic resonance, ultrasound and photonic imaging modalities.

Dynamic MR Elastography (MRE) is an in-vivo non-invasive dynamic elasticity imaging technique of “palpation by imaging” that emulates the traditional procedure of palpation allowing direct visualization of usually low audible frequency shear wave propagation deep in tissue-like materials through harmonic or periodic mechanical excitation and consequent quantitative assessment of local values of shear modulus of tissues [3] (Figure 1).

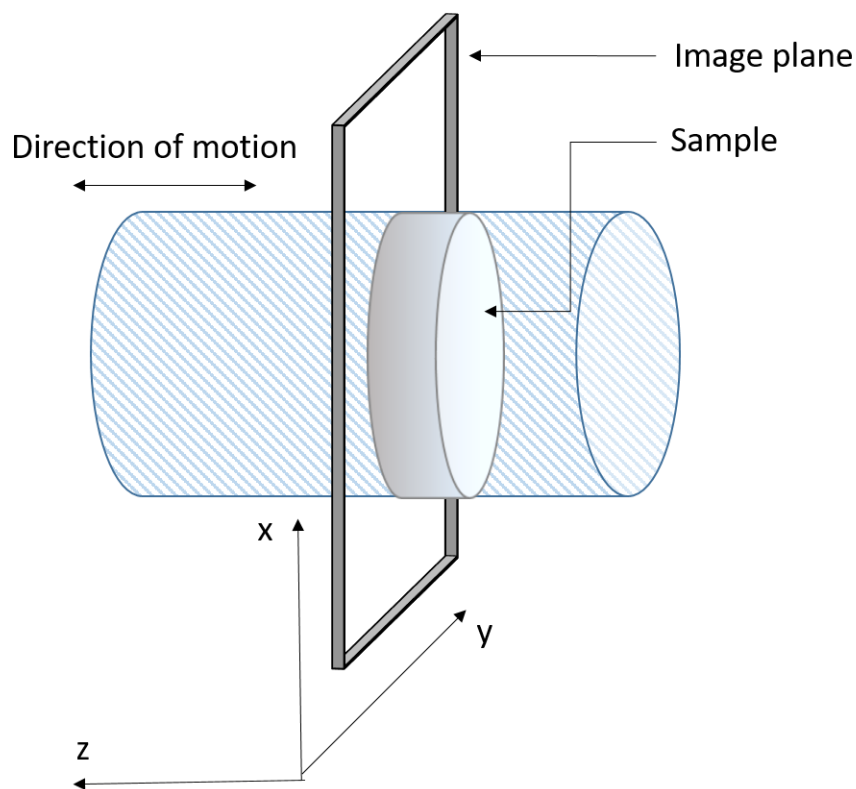


Figure 1: Experimental setup used for transmitting geometrically-focused shear waves for MRE.

The aforementioned harmonic excitation is employed in order to detect stiffer areas in biological tissues by the study of mechanical wave propagation inside the body tissues. Considering the wavelength of the propagating wave, it is possible to relate it to the stiffness of the tissue since, the stiffer a material is, the faster a wave will propagate through it, and thus the longer its wavelength will be. The sensitivity of wavelength to changes in elasticity is used to map heterogeneities of elasticity, since local variations of wavelengths correspond to local variations of shear modulus.

Dynamic MRE can be used to robustly quantify rheological behavior, elasticity and viscosity, by spanning a wide frequency range for the dynamic loading. This procedure resembles the rheometer testing used for studying viscoelastic properties of materials. For this reason, dynamic MRE can be considered as an “in vivo rheometry” technique to study the microstructure of a tissue[4].

While MRE has been studied with respect to its applications on a wide range of different tissues, such as liver [2], brain [5] or breast [2], the present work will be focused on elastography application to the skeletal muscle: indeed, not much is known about skeletal muscle viscoelastic properties *in vivo*, and the possibility to characterize non-invasively this tissue could be fundamental for diagnosis or monitoring of several diseases, such as spasticity, Duchenne muscular dystrophy and hyperthyroidism [6] [7], that affect muscle functionality [3] [8].

Moreover, the relationship between the macroscopic shear waves motion and local viscoelasticity of the material is well understood for homogeneous and isotropic materials, but not in the case of an anisotropic and heterogeneous medium with complex microstructure [2]. Few elastography studies can be found that deal with the relationship between the effectively measured viscoelastic constants and the tissue's microstructure [4].

Assessment of anisotropic mechanical properties of muscle could be useful in diagnosing pathological changes in muscle stiffness resulting from disease, blunt trauma, overuse, or as secondary complications of surgery, radiotherapy, immobilization, stroke, or spinal cord injury with implications for reduced range of motion, chronic pain, discoordination, and increased rate of injury [7].

Though there is a long history of measuring joint stiffness, there are currently no validated methods for directly non-invasively quantifying *in vivo* intrinsic muscle stiffness independent from neurally-mediated changes in muscle activation and contributions from soft tissues, or disambiguating contributions from the active and passive elements in a muscle [9]. Moreover, the relationship between velocity of shear waves and local stiffness of the material is well understood for homogeneous and isotropic materials, but not in case of anisotropic materials with complex composite microstructure [10] [11] [12].

One of the approaches to improve MRE data acquisition protocols is to develop phantoms that realistically simulate properties of soft tissues [13]. While phantoms have traditionally been used to validate medical imaging techniques, the fabrication of a phantom that can simulate skeletal muscular tissue in a MRE test has peculiar requirements, namely that it must be both anisotropic and with composite microstructure [14].

The goal of the presented study is the development of a realistic computational finite element (FE) model of skeletal muscle that captures its macroscopic, microscopic and multiscale fractal features such that it can

be used to optimally design and interpret experimental measurements acquired using MRE. The clinically-driven overarching hypothesis is that, by understanding the truly multiscale and fractal muscle structure, one can correlate changes in underlying microstructure brought on by disease, trauma or therapy to MRE measurements of the macroscopic anisotropic mechanical wave motion. To accomplish this goal, we begin by developing and studying, both computationally and experimentally, a simplified anisotropic muscle tissue phantom with minimal composite structure in the form of stiffened parallel fibers. If the FE modeling approach can be validated by accurately simulating the MRE experiment for this simple phantom, then the FE modeling approach can be used to construct more complex and realistic muscle-like phantoms. Through their simulation we expect to gain insights into the optimal design of the MRE experiment, including measured data post processing, for real muscle tissue and to quantify the limitations one faces in discerning microstructure at scales below the image resolution from macroscopic measurements[4].



## CHAPTER 2

### MAGNETIC RESONANCE ELASTOGRAPHY (MRE)

MRE's rationale is based on the following classic approach of materials' science: by applying a known stress and measuring the resultant strain it is possible to estimate the elastic modulus of a sample. Alternative methods involve the use of multiple measurements using different values of stress or varying between dynamic or static stress. This is the approach followed by most of elasticity imaging techniques. Based on temporal characteristics of the excitation, the stimulus can be classified as static or quasi-static (as for example manual palpation) and dynamic (as for example magnetic resonance elastography [3] [15]) elasticity assessment technique.

Using an imaging technique it is possible to observe the resulting strain distribution as a consequence of an applied stress. In this way the parameters that reflect the mechanical properties can be estimated.

#### 2.1 Steps in MRE

In deeper detail, MRE gets information about the viscoelasticity or dynamic stiffness of tissue through three basic steps: excitation, wave images acquisition and shear modulus identification (Figure 2).

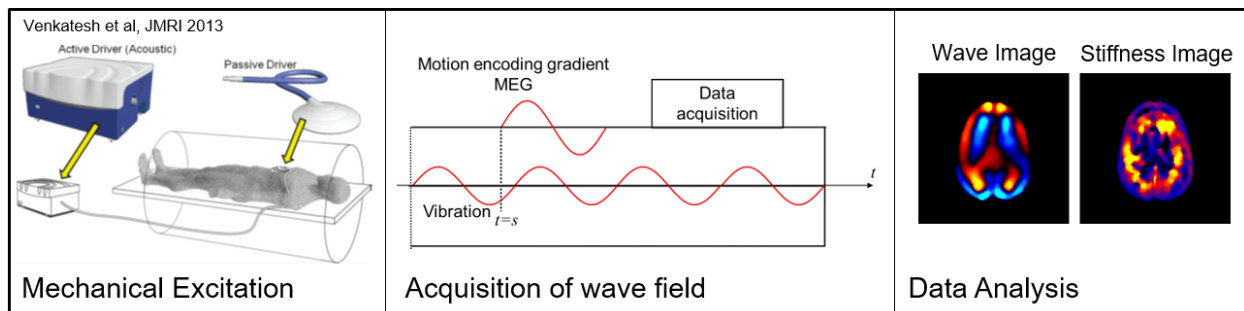


Figure 2: Schematic diagram of steps in magnetic resonance elastography. Provided by Prof Dieter Klatt.

##### 2.1.1 Excitation

Shear waves are sent in the tissue using external drivers (frequency range of 10-16,000 Hz) [16] [17] [18] [19].

A signal generator synchronized to and triggered by the magnetic resonance pulse sequence produces the electrical signal for external driver devices. Subsequently, before going to the mechanical driver, it is amplified using an audio amplifier.

Shear waves are obtained by applying harmonic displacement on the surface of the tissue along the direction tangent to the surface itself. The displacements are obtained through a piezoelectric driver or using focused ultrasound [20].

The resulting spatial resolution increments with the frequency of the propagating waves; but, since shear waves at high frequency are attenuated more than waves at low frequency, up to the point where they become undetectable, a compromise should be found between the Signal to Noise Ratio and image resolution.

### **2.1.2 Wave images acquisition**

Since MRE purpose is to detect the wave propagation in the region of interest (ROI), it is necessary to encode the motion of each voxel during said propagation acquiring MR images. This is made possible by switching on, in addition to ordinary MRI gradients described in Appendix A, a Motion Encoding Gradient (MEG), when the wave propagation has reached a stationary condition so that it is possible to assume a harmonic vibration during motion encoding [21] [3].

This MEG (Figure 3) is imposed along a specific direction, with frequency encoding gradient, before read out phase, and has to be started synchronously with the mechanical excitation from vibration generator; it is thus necessary to employ a programmable trigger signal.

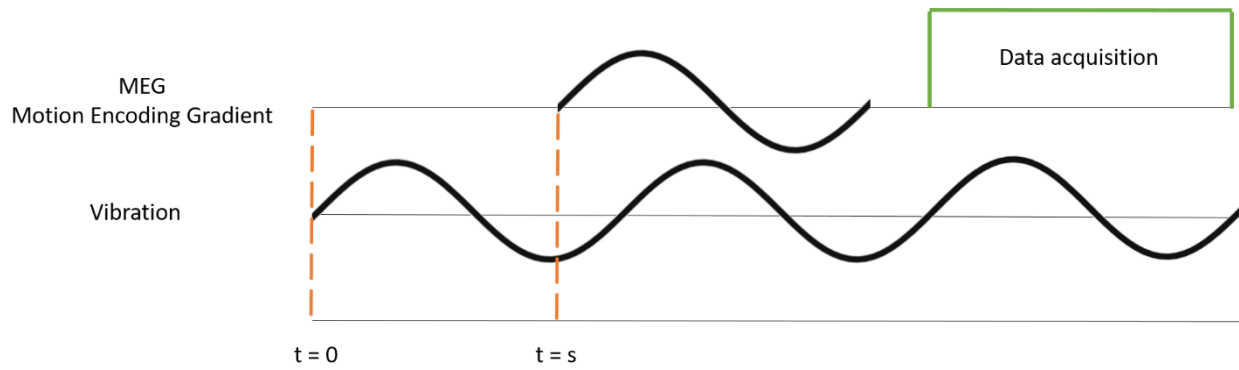


Figure 3: Synchronization of MEG with mechanical excitation signal.

By changing the axes on which the motion-sensitizing gradients are placed, it is possible to encode motion in any direction into the phase of MR image (Figure 4).

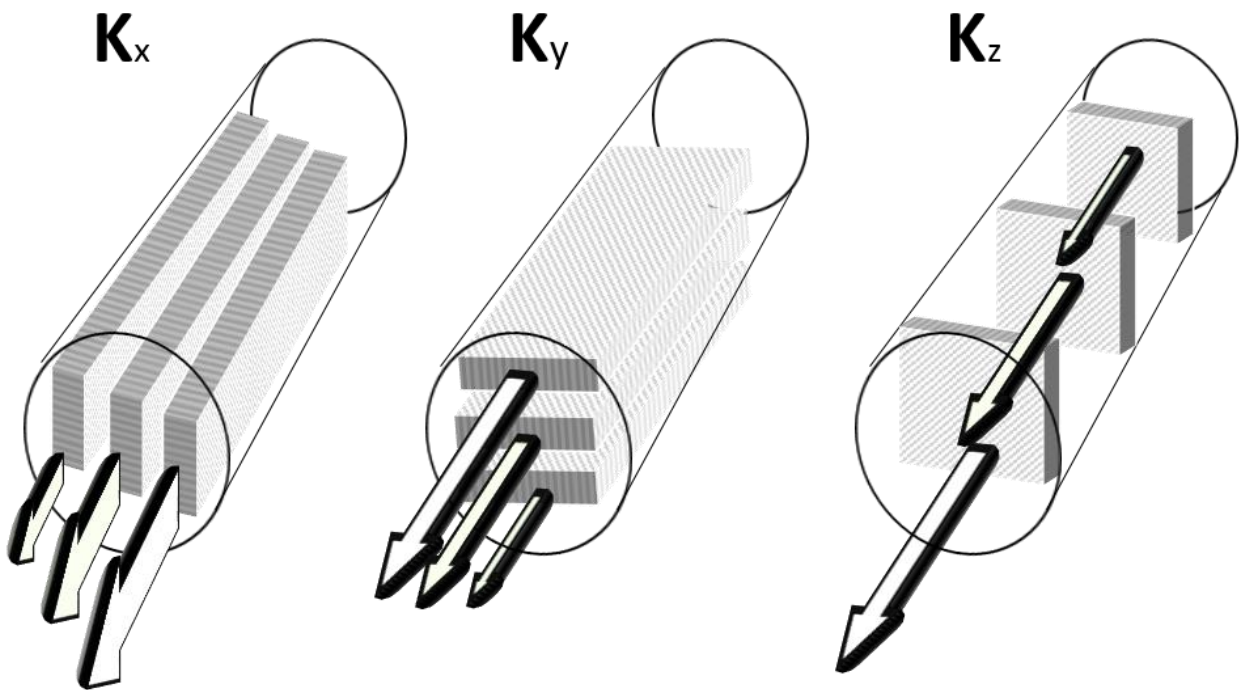


Figure 4: The direction of the MEG defines the direction along which the component of the displacement of voxels is measured.

The MEG is usually characterized by a sinusoidal, trapezoidal or step function, always bipolar and symmetric, started at a given start time  $t=s$  and lasting for a certain period of time  $\tau_K = \frac{2\pi q}{\omega_K}$ , where  $q$  is the MEG number of cycles and  $\omega_K$  the angular frequency of MEG.

If MEG is defined as harmonic encoding gradient with initial phase  $\theta_K = -\omega_K s$  as initial condition:

$$K(t) = K_0 \sin(\omega_K t + \theta_K) \quad (2.1)$$

and the vibration deflection can be described by the following sinusoidal function:

$$u_n(t, \mathbf{x}) = u_n(r) \sin(\omega_n t + \theta_n) \quad (2.2)$$

where the index  $n$  is used in case of multi-frequency signal so that

$$u(t, \mathbf{x}) = \sum u_n(t, \mathbf{x}) \quad (2.3)$$

then the phase of the transverse macroscopic magnetization  $M_T$ , in function of the MEG start time  $s$  is described by:

$$\varphi(s, \mathbf{x}) = \int \omega_L dt = \gamma \int B(t, \mathbf{x}) = \gamma \int K(t) \cdot u(t, \mathbf{x}) dt = \gamma \int_s^{s+\tau_K} K(t) \cdot u(t, \mathbf{x}) dt \quad (2.4)$$

where  $\omega_L$  is the Larmor frequency,  $B$  is the magnetic field and  $\gamma$  is the gyromagnetic ratio.

Solving the integral, a harmonic function is still obtained:

$$\varphi_n(s, \mathbf{x}) = \varphi_n^0 \sin(\omega_n s + \theta_n + \Delta\theta_n) \quad (2.5)$$

where  $\varphi_n^0$ ,  $\omega_n$  are constant terms and  $\Delta\theta_n$  is the constant phase shift.

Thus, the only unknown to be determined is  $\theta_n$ , that is the initial phase of the mechanical vibration.

The global phase of MR signal can be obtained by summation of the phase associated to each frequency:

$$\varphi(s, \mathbf{x}) = \sum \varphi_n(s, \mathbf{x}) \quad (2.6)$$

Setting the phase offset between the MEG and the mechanical excitation, it is possible to obtain the wave images at various phase offsets equally spaced during a cycle. Thus, performing conventional MR imaging, the harmonic component at a specific frequency can be recovered, given, at each point, the phase and amplitude of the harmonic displacement, relative to an arbitrary point taken as zero [22].

To quantify in how many radians one meter of the displacement amplitude is encoded in the MR signal phase the encoding efficiency is defined as:

$$\xi_n = \frac{\varphi_n^0}{u_n} \quad (2.7)$$

In a multi-frequency experiment, Discrete Fourier Transform of the phase signal  $\varphi(s, \mathbf{x})$  must be performed to identify the Nyquist frequency in order to apply the Shannon theorem for the temporal sampling of the signal. In this way, the temporal resolution will be high enough to capture all the frequencies of interest.

Once this is done, it will be possible to derive the displacement field (of the order of  $\mu\text{m}$ )  $u(t, \mathbf{x})$  by scaling the MR phase signal  $\varphi(s, \mathbf{x})$  by the encoding efficiency  $\xi_n$ .

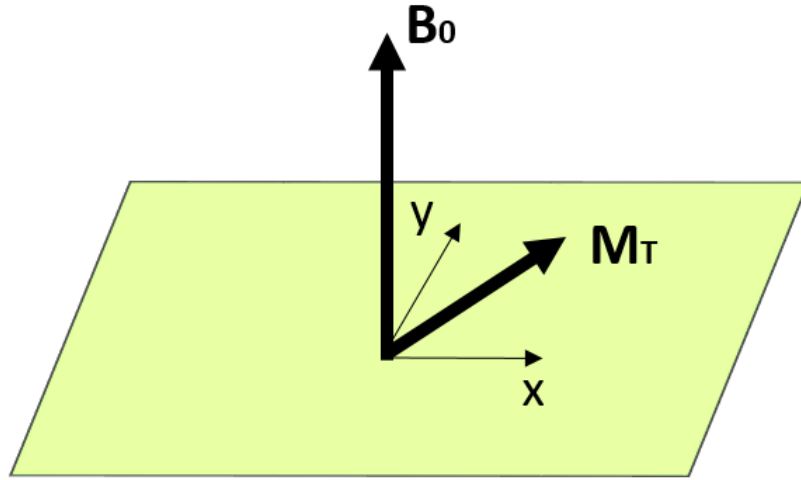


Figure 5: Representation of  $M_t$ , transverse magnetization (MR signal), in presence of external main magnetic field  $B_0$  parallel to z-axis.

A key feature of the MRE is that an intravoxel coherent motion is considered. Looking at the vibration of the voxels, while the voxel moves, the position of the individual spins relative to the voxel is static; intravoxel spins show the same precessing macroscopic magnetization being in phase within one voxel thus precessing coherently.

Therefore, any spin precessing motion causes a measurable phase shift in the MR signal in the presence of these motion-sensitizing gradients.

The displacement for each voxel can be obtained measuring the phase shift (Figure 6), and directly represents the wave propagation inside the sample, knowing that the phase of the tissue harmonically vibrating and its displacement are directly proportional [2].

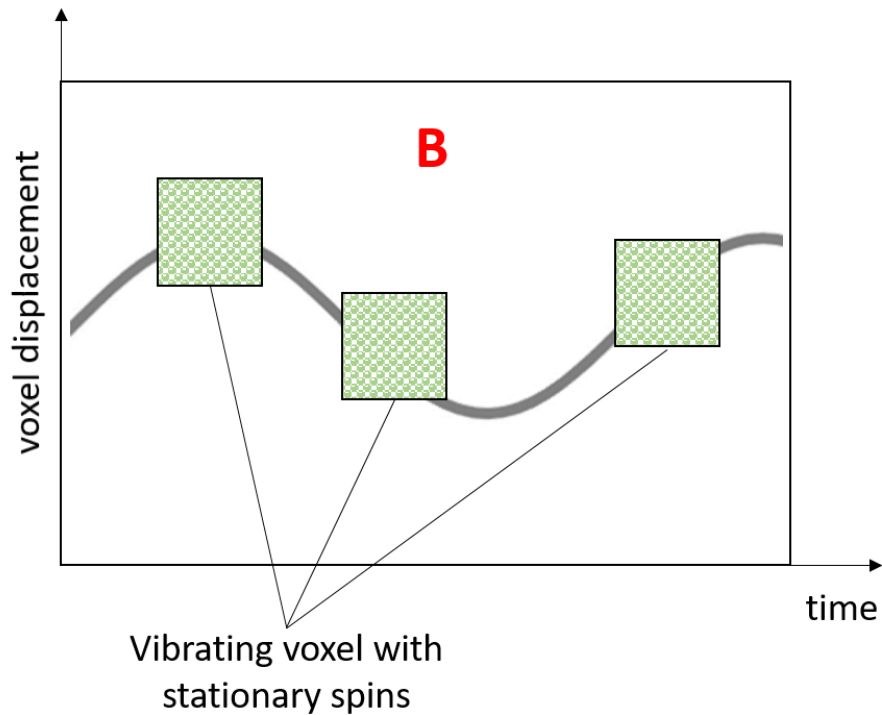


Figure 6: Visualization of some voxels displacement in the ROI. In a single voxel spins are assumed to be stationary so that they vibrate with the same phase.

In the case of a shear wave the voxels move perpendicular to the wave propagation direction. An equal mechanical vibration phase in different voxels results as the same phase of MRI signal  $M_T$ . It is possible to encode voxel vibration, obtaining initial phase of the mechanical vibration, by reading the phase of  $M_T$  signal using MEG. The MEG can thus be seen as a snapshot of the mechanical wave.

The acoustic strain wave propagation in the medium can be visualized as images reflecting the displacement of spins; these images are called “wave images”.

### **2.1.3 Shear modulus estimation**

Quantitative values of shear stiffness can be estimated from the shear waves propagation using equations of motion [3] [23], that will be described more in detail further on.

As said before, the viscoelasticity of the tissue at each location corresponds to a precise propagating wave local wavelength, so the images of shear waves are processed to obtain quantitative maps, called elastograms, depicting local quantitative values of the imaginary and real parts of the shear stiffness of tissues. Shear wavelength in tissue-like materials extends from mm to tens of mm for frequencies typically used in MRE.

## CHAPTER 3

### ANATOMY AND PHYSIOLOGY OF SKELETAL MUSCLE

The investigated tissue, skeletal muscle, has the principal mechanical properties of soft tissues which are in between those of solids and fluids. The values of coefficient of Poisson are very close to that of incompressibility: 0.5, because of the large difference between bulk modulus and shear elasticity. Being very close to the incompressibility condition the shear modulus  $\mu$  and the Young modulus  $E$  show an approximate difference given by a scaling factor of 3:

$$E=3\mu. \quad (3.1)$$

The density is very similar to that of water ( $\sim 1 \frac{Kg}{dm^3}$ ) [24]. In addition, the bulk modulus of most soft tissues are within 15% to that of water [25]. Finally, soft tissues typically exhibit anisotropic, non-Hookean (for large amplitude deformation), viscoelastic and non-homogeneous behavior.

#### **3.1 Anisotropy and fractal structure of skeletal muscle**

Skeletal muscle is a viscoelastic, anisotropic and hierarchically organized soft tissue. The microstructural arrangement in fascicles characterized by parallel fibers aligned in series is what gives muscle anisotropy.

Since different components of the microstructure interact and deform under load, leading to the resultant response characteristic of muscle mechanical behavior, the bundles need to be organized, at different length scales, in a complex hierarchical structure [26]. This self-similar geometrical replication of identical geometrical patterns, that rules over a continuum of hierarchical levels, means that mathematically skeletal muscle can be considered as a fractal structure.

The myofibrils constitute the muscle fibers that in turn form the fascicles. The myofibrils and the muscle fibers are disposed along the muscle fiber axis. Myofibrils are in turn composed of series of sarcomeres.

Three types of connective tissue sheaths support this organization, starting from the inner:

- The endomysium surrounds each muscle fiber and has connections with the perimysium [1].



- The perimysium has connections with the epimysium and separates muscle fascicles. Furthermore, inside the perimysium nerve fibers and blood vessels are present.
- The epimysium surrounds the muscle and is a collagenous layer that separates muscles from each other and from other tissues.

### 3.2 Fibers and sarcomeres

In Figure 7 it is possible to see that a muscle fiber is the structural unit of the skeletal muscle: it is a single cylindrical muscle cell also known as myocyte. Muscle fibers have a length from 1 to 30 cm and a thickness from 10 to 100  $\mu\text{m}$ . A single skeletal muscle may be made up of hundreds or even thousands of myocytes bundled together and wrapped in a connective tissue covering.

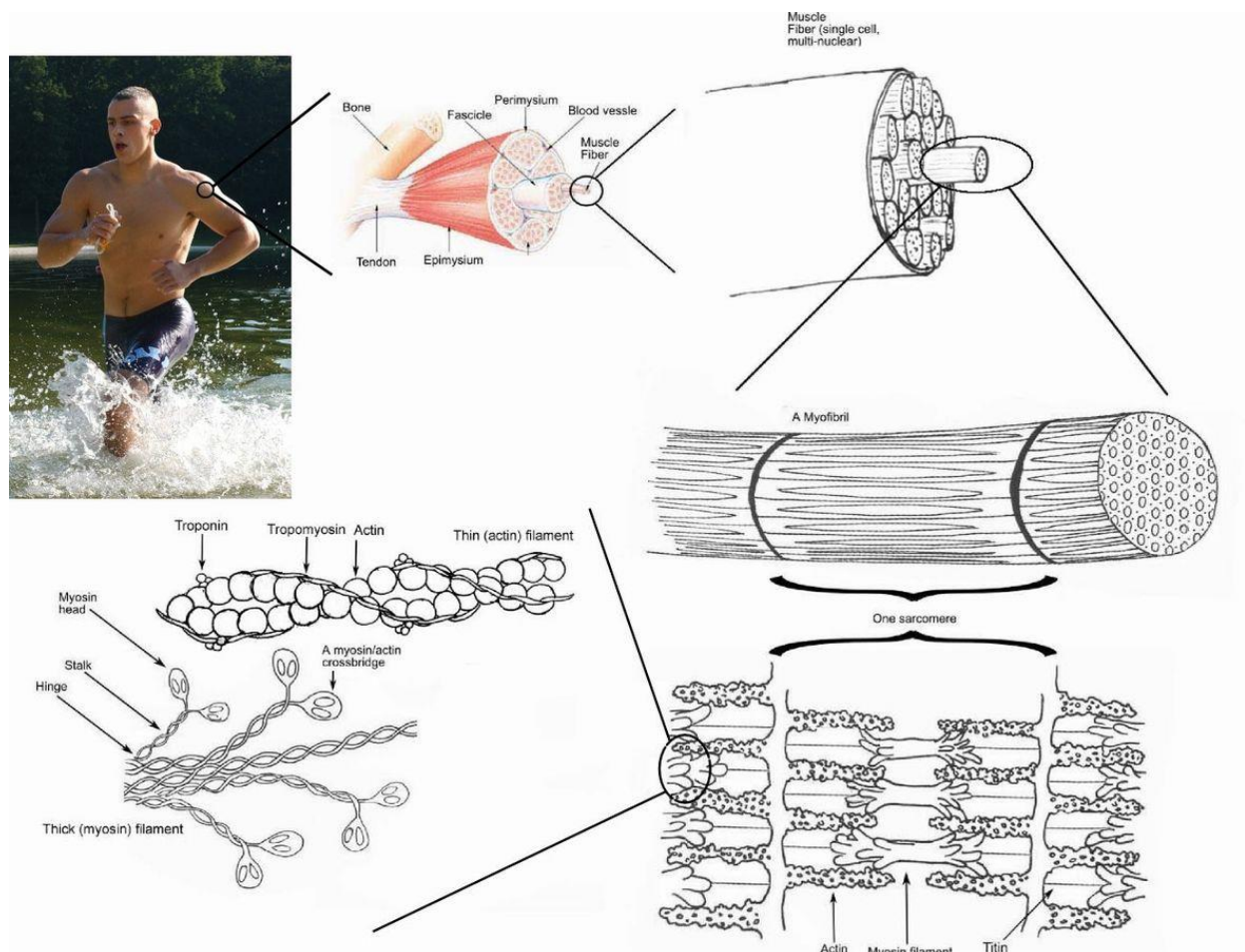


Figure 7: Hierarchical levels in skeletal muscle tissue. "Skeletal muscle" photo montage created by Raul654 and Rama, licensed under PD-USGov, GFDL.

The systematic arrangement of the myofibrils, invested by a delicate plasma membrane called the sarcolemma, gives skeletal muscle its typical striated pattern. The repetitive unit in this pattern is called sarcomere and it is the contractile unit of a muscle [26].

A sarcomere goes from Z-line to Z-line and comprises overlapping myosin and actin filaments called respectively thick and thin filaments. In humans, thin filament diameters and lengths appear to be about 5 nm and 1.27  $\mu\text{m}$  respectively. The corresponding values for thick filament are about 15 nm and 1.6  $\mu\text{m}$ , which are nearly constant among many animal species [27]. The alternation of actin and myosin characterizes the so called striation typical of skeletal muscle fibers.

To different areas correspond different names: the A-band is the dark region where myosin and actin overlap, and it is split in two; the I-band is the area where thick myosin filaments are not present and it is centered about the Z-line; the H-band instead consists principally of connections of myosin filaments with the M-line [1].

### **3.3 Muscle proteins**

In the sarcomere there are also large proteins that provide structural stability. These are titin and nebulin, which have implications in the passive elasticity of the muscle.

Titin is nearly 1  $\mu\text{m}$  in length and has an important role when a muscle is stretched above its resting length since it anchors myosin filaments at the center of the sarcomere; thanks to elastic energy release due to elongation, titin allows the muscle to go back to its resting length.

Nebulin is a protein extending from the Z disk that provides reinforcement to the thin actin filaments.

Two additional proteins, troponin and tropomyosin, are important constituents of actin, because they seem to regulate the breaking and making of links between the myosin and actin during contraction.

Finally, the heads on the myosin body (bridges) attach to the thin filament to form a cross-bridge [26].

Not only cytoskeletal elements inside the sarcomere provide myocellular structural support, but there are also networks of intermediate filaments surrounding the sarcomere. Their name is given by the fact that they have intermediate dimensions between actin and myosin filaments.

Two important intermediate filaments are desmin, that forms a network surrounding the sarcomere enabling force transmission between adjacent myofibrils, and skelemin, surrounding the sarcomere, which interlinks the extracellular network interacting at the M line with myosin and nebulin.

There are also tubular systems constituting the network of cytoskeletal elements that provide cellular and organelle motility and structural support. They are the sarcoplasmic reticulum and the transverse tubules [1]. The former forms a net of channels surrounding myofibrils and transports the  $\text{Ca}^{2+}$  required to trigger muscle excitation, while the latter are responsible for the transmission of electric impulses at the level of the neuromuscular junction [1].

### 3.3.1 Mechanical behavior

Whereby stiffness increases with applied stretch, muscles show the characteristic nonlinear length–tension curve of most soft biological tissues (Figure 8).

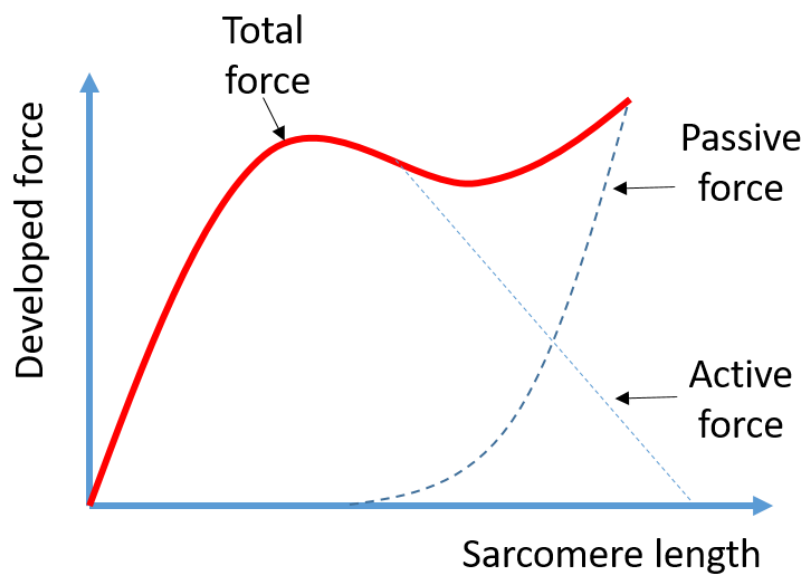


Figure 8: Tension developed by a sarcomere with respect to the length of the sarcomere.

Large passive movements contribute in reducing the increase in stiffness. The mechanical complex behavior of muscular tissues must be taken into account when measuring muscle mechanical properties,

particularly when measurements at different muscle lengths or joint positions are taken, where the influence of the nonlinear behavior influences any measures not considering the full nonlinear behavior [28].

## CHAPTER 4

### MECHANICAL WAVES AND INVERSE AND DIRECT PROBLEMS IN MRE

In MRE mechanical waves are induced in the solid sample and images of the wave propagation are obtained. This chapter focuses on the propagation of mechanical waves in solids, while no mention will be made to electromagnetic and vibro-acoustic inputs necessary to generate and measure these waves.

In a discrete mass-spring system, a disturbance applied to a mass particle is transferred to the following mass and, due to the presence of interconnecting springs, the disturbance is soon transferred to a remote point, despite any given particle of the system is moved only by a relatively small amount. If the stiffness of the connecting springs is increased or the particle masses decreased, or both, the speed of motion transfer would be expected to increase. In case of a continuous medium the mass and elastic parameters are distributed in terms of mass density and the elastic moduli and a point disturbance spreads outward in a three-dimensional sense.

There is a classification of waves depending on three factors: propagation mode, properties of the medium and nature of any boundaries of the propagation medium. Within an isotropic elastic medium there are compressional (longitudinal) and shear (transversal) wave types. If a boundary to the medium exists this can give rise to additional wave types, including Rayleigh and Love [29].

In soft biological tissues compressional waves propagate at a velocity around 1500 m/s, comparable to their propagation speed in water. Shear waves are typically much slower with velocity amplitudes from 1 to 10 m/s[30].

As a consequence of this nominally three order of magnitude difference in velocity between shear and compressional waves, and given the typical frequency range used in MRE, compressional waves present too large wavelengths in biological tissues and thus they are not displayable in the region of interest (ROI). Therefore, we prefer to remove compressional wave effects in any measurement, before displaying shear wave images. This is done by applying the curl operator to the equation of motion or using a high pass spatial filter.

#### 4.1 Longitudinal and transverse waves

Since elastography relies on the analysis of the wave propagation pattern through a given tissue, a brief overview of the equations and definitions concerning mechanical waves is due.

Longitudinal waves can be defined, starting from the general Navier's equation for a linear elastic homogeneous isotropic continuum [31], in absence of body forces:

$$\mu u_{i,jj} + (\lambda + \mu) u_{j,ji} + X_i = \rho \frac{\partial^2 u_i}{\partial t^2} \quad (4.1)$$

as a motion such as:

$$u_i = A \sin \frac{2\pi}{l} (x \pm ct) \quad \text{if } i = 1, \quad u_i = 0 \text{ otherwise} \quad (4.2)$$

where  $\rho$  is the material density,  $\mu$  and  $\lambda$  are the two Lamé parameters,  $A$  and  $l$  are respectively the amplitude and the wavelength of the wave, and  $c$  is the wave speed. It is immediate to verify, by substituting (4.2) in (4.1), that this solution is possible if  $c$  is given by the following formula:

$$c_L = \sqrt{\frac{\lambda + 2\mu}{\rho}} = \sqrt{\frac{E(1-\nu)}{(1+\nu)(1-2\nu)\rho}} \quad (4.3)$$

$c_L$  is the phase velocity, and it is the rate at which the wave propagates in space. Namely, a given component of the wave (a crest or a valley) will be travelling through space at phase velocity.

Likewise, transverse waves can be defined as a solution where:

$$u_i = A \sin \frac{2\pi}{l} (x \pm ct) \quad \text{if } i = 2, \quad u_i = 0 \text{ otherwise} \quad (4.4)$$

and  $c$  assumes the value

$$c_T = \sqrt{\frac{\mu}{\rho}} \quad (4.5)$$

where  $c_T$  is the transverse wave speed. In both cases the wave velocity is directly proportional to the square root of the material elasticity and inversely proportional to the square root of the density [32].

The shear modulus, in the simplest case of an elastic, homogeneous and isotropic medium, with no attenuation, is given by  $\mu = \rho c_T^2$  [33].

An incident transverse or longitudinal wave is reflected and refracted in a combination of transverse and longitudinal waves. In general boundary problems can be solved by properly combining transverse and longitudinal waves, satisfying the boundary conditions [31].

## **4.2 Introduction to the inverse problem**

Elastography comprises different techniques whose goal is to estimate mechanical properties of a tissue based on the mechanical wave images. The propagation of the waves inside the material is described by the wave equation and, knowing the map of displacements in the tissue subject to harmonic excitation, the mathematical problem consists in, essentially, inverting the wave equation to estimate the material mechanical properties.

The estimation of mechanical properties of a tissue starting from MR imaging is an inverse problem: indeed, the displacement amplitude field is known along with the geometry of the body and boundary conditions while the constitutive parameters of the tissue are unknown. The governing equations are the partial differential wave equations. Instead, in direct problems the material mechanical properties are known and the displacement, stress and strain fields, are the unknown fields to be determined. Traditionally inverse problems have been solved through scalar Helmholtz inversion, which will be discussed further on [33]. In more recent studies it has been shown that inverse problems can also be solved by means of optimization algorithms through which an error function, that represents the difference between experimental displacement data and those estimated through a model, is minimized; the constitutive parameters governing the model are the available variables for minimization [34].

Traditionally the inverse problem in MRI imaging is solved through simplifying assumptions: local homogeneity, elasticity and isotropy. Under these assumptions, direct local inversion of the displacement data acquired during three directed cyclic deformations as function of time in the whole imaged area, allows to recover viscoelastic properties of tissues, without the necessity to consider boundary conditions or estimate the stress field. This procedure will be further illustrated in the following paragraphs.

The mechanical quantities that are to be characterized are those relating stress and strain; for most soft tissues the displacements in magnetic resonance elastography are on the order of microns (strain < 1%), and so a linearized constitutive relationship is used.

### 4.3 Equation of motion for an isotropic linear continuum

The wave equation is derived from the equilibrium between volume and surface forces in the continuum.

$$\rho \frac{\partial^2 u_i}{\partial t^2} = \frac{\partial \sigma_{ij}}{\partial x_j} \quad (4.6)$$

Infinitesimal deformations and the hypothesis that the displacement from pre-stressed states depends only on additional stress are the starting assumptions.

The stiffness tensor relating stress to strain for an isotropic linear medium, because of the conservation of elastic deformation energy and of the symmetry of the stiffness tensor, is the following:

$$\mathbf{C} = \begin{bmatrix} (2\mu + \lambda) & \lambda & \lambda & 0 & 0 & 0 \\ \lambda & (2\mu + \lambda) & \lambda & 0 & 0 & 0 \\ \lambda & \lambda & (2\mu + \lambda) & 0 & 0 & 0 \\ 0 & 0 & 0 & 2\mu & 0 & 0 \\ 0 & 0 & 0 & 0 & 2\mu & 0 \\ 0 & 0 & 0 & 0 & 0 & 2\mu \end{bmatrix} \quad (4.7)$$

with

$$\varepsilon_{ij} = \begin{bmatrix} \varepsilon_{xx} \\ \varepsilon_{yy} \\ \varepsilon_{zz} \\ \varepsilon_{yz} \\ \varepsilon_{xz} \\ \varepsilon_{xy} \end{bmatrix} \quad \text{and} \quad \sigma_{ij} = \begin{bmatrix} \sigma_{xx} \\ \sigma_{yy} \\ \sigma_{zz} \\ \sigma_{yz} \\ \sigma_{xz} \\ \sigma_{xy} \end{bmatrix} \quad \text{and} \quad \varepsilon_{ij} = \frac{(u_{i,j} + u_{j,i})}{2}$$



where  $\mu$  and  $\lambda$  are, for a viscoelastic material, complex numbers. Therefore, the stress-strain relation in index notation is the following:  $\sigma_{ij} = \lambda\theta\delta_{ij} + 2\mu\varepsilon_{ij}$  where  $\theta$  is the trace of  $\varepsilon$  so that it is equal to  $u_{j,ji}$  and  $\delta_{ij}$  is the delta of Kronecker which is equal to 1 if  $i=j$  while it is 0 if  $i \neq j$ .

The result of this substitution is:

$$\rho \frac{\partial^2 u_i}{\partial t^2} = \lambda \frac{\partial \theta}{\partial x_j} + 2\mu \frac{\partial \varepsilon_{ij}}{\partial x_j} \quad (4.8)$$

considering the hypothesis of local homogeneity (spatial derivative of  $\lambda$  and  $\mu$  are zero as these parameters are locally constant in space).

By introducing the strain-displacement differential relationship, the equilibrium equation in terms of displacement becomes:

$$\rho \frac{\partial^2 u_i}{\partial t^2} = \mu u_{i,jj} + (\lambda + \mu) u_{j,ji} \quad (4.9)$$

The solution of this equation is called plane wave solution:

$$\mathbf{u}(\mathbf{x}, t) = u_o e^{(i\omega(t - \frac{\mathbf{n} \cdot \mathbf{x}}{c}))} \mathbf{e}_u \quad (4.10)$$

Where  $\omega$  is the angular frequency,  $c$  is the wave speed ( $c = \frac{\omega\lambda}{2\pi}$ ),  $u_o$  is the displacement amplitude,  $\mathbf{x}$  is the position vector,  $\mathbf{n}$  is the vector normal to the plane wave wavefront and  $\mathbf{e}_u$  is the unit vector in displacement direction.  $\mathbf{e}_u$  is parallel to  $\mathbf{n}$  in the case of compression waves, while is perpendicular to it in case of shear waves.

The solution is different in case of compression wave or shear wave since the wave speed is different.

Mathematical inversion algorithms of displacement data starting from wave equations, with simplifying assumptions (isotropy, incompressibility and homogeneity) lead to the estimation of mechanical properties.

If local homogeneity is assumed,  $\mu$  and  $\lambda$  no more vary depending on position, and the equation above becomes an algebraic matrix equation. Through direct inversion a solution to this equation can be found as described below:

$$-\rho\omega^2 u_i = \mu u_{i,jj} + (\lambda + \mu) u_{j,ji} \quad (4.11)$$

### 4.3.1 Scalar Helmholtz inversion

In soft tissues,  $\lambda$  is consistently larger than shear modulus  $\mu$  (typically  $10^4$  or more larger) [31], and for this reason the simultaneous calculation of both constants is impractical; but, thanks to that it is possible to decouple the two constants. However,  $\lambda$  can be neglected if the excitation is primarily shear, otherwise applying high pass filters to longitudinal waves or curl operators [33], since it is embedded in very low spatial frequencies.

To get rid of  $\lambda$ , it is possible to assume incompressibility that means to consider that displacements relative to the longitudinal wave are almost null. Consequently, it is possible to assume that

$$u_{j,ji} = 0 \quad (4.12)$$

With this assumption the equation reduces to the scalar Helmholtz equation:

$$[\mu(u_{i,j} + u_{j,i})]_{,j} = -\rho\omega^2 u_i \quad (4.13)$$

Now every component satisfies separately the equation since the terms that involve orthogonal directions components are decoupled.

Thus, in order to determine  $\mu$ , it is sufficient to estimate the Laplacian of the considered component and perform measures in only one sensitization direction. Finally, the exact scalar solution, known as scalar Helmholtz inversion, is obtained:

$$\mu = -\rho\omega^2 \frac{u_i}{u_{i,jj}} \quad (4.14)$$

This kind of inversion was used in 2D elastography, employed with narrow geometries where the information from a slice of the volume prove sufficient [33].

### 4.3.2 Algebraic Inversion of the Differential Equations (AIDE)

It is possible to rewrite equation 4.11, as

$$-\rho\omega^2 \begin{bmatrix} u_1 \\ u_2 \\ u_3 \end{bmatrix} = A \begin{bmatrix} \mu \\ \lambda \end{bmatrix} \quad (4.15)$$

where A is the following 3 x 2 matrix:

$$A = \begin{bmatrix} u_{1,ii} + u_{i,i1} & u_{i,i1} \\ u_{2,ii} + u_{i,i2} & u_{i,i2} \\ u_{3,ii} + u_{i,i3} & u_{i,i3} \end{bmatrix} \quad (4.16)$$

The unknown vector containing the model parameters is  $\mathbf{m} = \begin{bmatrix} \mu \\ \lambda \end{bmatrix}$  and the data vector is  $\mathbf{g} = \begin{bmatrix} u_1 \\ u_2 \\ u_3 \end{bmatrix}$ .

Since the number of unknown is smaller than that of the data, this over-determined system can be solved as a linear system, finding an approximate solution instead of the exact unique solution[35].

It is possible to use a least square approximation algorithm that minimizes the summation of the square error  $\varepsilon_i$  between the data and the model:

$$E(m_1, m_2) = \sum_{i=1}^3 (\varepsilon_i)^2 \quad (4.17)$$

where

$$\varepsilon_i = g_i - \sum_{j=1}^2 A_{ij} m_j \quad (4.18)$$

In order to minimize the error, it is possible to compute the derivative of  $\varepsilon$  with respect to the model parameters as follows:

$$\frac{\partial \varepsilon}{\partial m_k} = 2 \sum_{i=1}^3 (g_i - \sum_{j=1}^2 A_{ij} m_j) (-A_{ij}) = 0 \quad (4.19)$$

where  $k=1,2$

$$\sum_{j=1}^2 (\sum_{i=1}^3 A_{ij} A_{ik}) m_j = \sum_{i=1}^3 g_i A_{ik} \quad (4.20)$$

If  $\mathbf{g}$  is 3 x 1 vector,  $\mathbf{m}$  is 2 x 1 vector,  $A$  is a 3 x 2 matrix and  $A^T$  is 2 x 3, then  $A^T A$  will be a 2 x 2 matrix and  $A^T \mathbf{g}$  will be a 2 x 1 vector.

If

$$A^T A \mathbf{m} = A^T \mathbf{g} \quad (4.21)$$

the solution is given by

$$\mathbf{m} = (A^T A)^{-1} A^T \mathbf{g} \quad (4.22)$$

$$\begin{bmatrix} \mu \\ \lambda \end{bmatrix} = -\rho \omega^2 (A^T A)^{-1} A^T \begin{bmatrix} u_1 \\ u_2 \\ u_3 \end{bmatrix} \quad (4.23)$$

It would otherwise have been possible to get rid of  $\lambda$  starting from equation 4.11, and applying the curl operator to  $u_i$ . Defining  $q_i$  as:

$$q_i = \varepsilon_{ijk} \frac{\partial u_k}{\partial x_j}, \text{ with } \varepsilon_{ijk} = \begin{cases} 0 & \text{if } i, j \text{ or } k \text{ are equal} \\ 1 & \text{if } (i, j, k) = (1, 2, 3), (2, 3, 1) \text{ or } (3, 1, 2) \\ -1 & \text{if } (i, j, k) = (1, 3, 2), (3, 2, 1) \text{ or } (2, 1, 3) \end{cases}$$

previous equation can be rewritten as:

$$-\rho\omega^2 q_i = \mu q_{i,jj} \quad (4.24)$$

The final least square solution is given by:

$$\mu = -\rho\omega^2 [q_{i,jj}^T q_{i,jj}]^{-1} (q_{i,jj})^T q_i \quad (4.25)$$

### 4.3.3 Limitations of inversion algorithms

Both in two and three dimensions inversion algorithms require a good local approximation of the elastic waves by plane waves, otherwise it is impossible to relate in a straightforward way the local wavelengths to the underlying elasticities.

Through inversion algorithms local variations of wavelengths are associated to local variations of the isotropic shear stiffness. Based on isotropic prerequisites of inversion techniques the waves should have the same velocity irrespective of propagation direction at each point of homogeneous elastic material during propagation. This is not the case of anisotropic elastic material like skeletal muscle. In this case the wave velocity varies with the wave propagation direction.

## 4.4 Wave equation for an anisotropic viscoelastic medium

In some tissues like skeletal muscle, the previous assumption of isotropy is not valid. Muscle anisotropy is caused by its microstructural positioning of parallel fascicles of fibers arranged in series. Myofibrils are in turn are constituted by series of sarcomeres disposed in parallel [26].

Characteristics of both anisotropy and viscoelasticity must be considered. The challenge is so to try to measure direction dependent quantities in a wide dynamic range using multiple driver frequencies to assess viscoelastic properties [19].

Since only small deformations and displacements are considered, the theory is limited to small deformation in linear viscoelastic regime, and it is possible to use linearized constitutive equations.

Constituted by bundles of aligned fibers, skeletal muscle displays a preferential behavior in the direction of the fibers. Therefore, it can be represented by a transversely isotropic model with properties symmetric around an axis (along direction of muscular fibers) normal to the isotropy plane [36] [37].

In such a plane the material properties are the equal in each direction since infinite planes of symmetry are contained in the transverse plane. This model is completely characterized by five independent mechanical parameters (two Young Moduli, one shear stiffness, and two Poisson's ratios). Moreover, in the case of skeletal muscle, due to the high presence of water, it is possible to set the hypothesis of incompressibility (Poisson's ratio around 0.5), which allows to reduce the independent parameter to only three, one ratio of Young moduli, perpendicular and parallel to the fibers, and two shear moduli [38].

Indeed, starting from the compliance tensor (for which  $x_3$  is the preferential anisotropic direction), for a transversely isotropic material:

$$\begin{bmatrix} \varepsilon_1 \\ \varepsilon_2 \\ \varepsilon_3 \\ \vdots \end{bmatrix} = \begin{bmatrix} \frac{1}{E_1} & -\frac{\nu_{12}}{E_1} & -\frac{\nu_{13}}{E_3} & 0 & 0 & 0 \\ \cdot & \frac{1}{E_1} & -\frac{\nu_{13}}{E_3} & 0 & 0 & 0 \\ \cdot & \cdot & \frac{1}{E_3} & 0 & 0 & 0 \\ \vdots & \vdots & \vdots & \vdots & \vdots & \vdots \end{bmatrix} \begin{bmatrix} \sigma_1 \\ \sigma_2 \\ \sigma_3 \\ \vdots \end{bmatrix} \quad (4.26)$$

the incompressibility condition becomes:

$$\theta = \varepsilon_1 + \varepsilon_2 + \varepsilon_3 = 0 \quad (0.27)$$

$$\frac{1}{E_1} \sigma_1 - \frac{\nu_{12}}{E_1} \sigma_2 - \frac{\nu_{13}}{E_3} \sigma_3 - \frac{\nu_{12}}{E_1} \sigma_1 + \frac{1}{E_1} \sigma_2 - \frac{\nu_{13}}{E_3} \sigma_3 - \frac{\nu_{13}}{E_3} \sigma_1 - \frac{\nu_{13}}{E_3} \sigma_2 + \frac{1}{E_3} \sigma_3 = 0 \quad (4.28)$$

which is true if  $\sigma_1 \stackrel{\text{I}}{=} \sigma_2 \stackrel{\text{II}}{=} \sigma_3 \stackrel{\text{III}}{=} 0$ .

Condition III entails:  $-\frac{2\nu_{13}}{E_3} + \frac{1}{E_3} = 0 \Rightarrow \nu_{13} = \frac{1}{2}$

While condition I (which is equivalent to II) entails:  $\frac{1}{E_1} - \frac{\nu_{12}}{E_1} - \frac{1}{2E_3} = 0 \Rightarrow \nu_{12} = 1 - \frac{E_1}{2E_3}$

According to the transverse isotropic model, the tissue is characterized by two planes: plane of isotropy and plane of symmetry, normal and parallel to fibers direction respectively. Shear waves will be imaged in these two planes to recover the anisotropic shear moduli [39].

In addition, the hypothesis of elasticity is released, since soft biological tissues have strong damping characteristics and so they have to be modeled as viscoelastic. They are subject to a tiring effect (the stress

necessary to maintain a constant deformation decreases in time during a step-strain experiment) due to absorption of mechanical energy converted in heat.

For a linear viscoelastic model, the correspondence principle may be applied [40] by which, if the elastic solution is available, then the viscoelastic solution is obtained in the frequency domain by substituting the elastic moduli with the complex viscoelastic moduli. An alternative approach is to set the stress-strain relation for a viscoelastic and transverse isotropic material and substitute it into the equation of motion from the beginning.

Indeed, since a viscoelastic medium is being considered, the shear elasticity  $\mu$  is complex-valued in the frequency domain. For harmonic motion, since the time derivative of the strain is what defines the damping term, it will be replaced by the imaginary part of the complex shear stiffness  $\mu$  that could be rewritten as [41]:

$$\mu(\omega) = \mu_{Re} + \mu_{Im} \quad (4.29)$$

where  $\mu_{Im}$  is the loss modulus and  $\mu_{Re}$  is the storage modulus.

Therefore, the stress-strain relation results:

$$\sigma_{ij} = \mathbf{C}\varepsilon_{kl} + \mathbf{D}\dot{\varepsilon}_{kl} \quad (4.30)$$

where

$$\sigma_{ij} = \sigma_{ij}(\omega), \varepsilon_{kl} = \varepsilon_{kl}(\omega)$$

$$\varepsilon_{kl} = \frac{(u_{k,l} + u_{l,k})}{2} \quad \varepsilon_{kl} = \begin{bmatrix} \varepsilon_{xx} \\ \varepsilon_{yy} \\ \varepsilon_{zz} \\ \varepsilon_{yz} \\ \varepsilon_{xz} \\ \varepsilon_{xy} \end{bmatrix} \quad \sigma_{ij} = \begin{bmatrix} \sigma_{xx} \\ \sigma_{yy} \\ \sigma_{zz} \\ \sigma_{yz} \\ \sigma_{xz} \\ \sigma_{xy} \end{bmatrix}$$

and D is the damping matrix, while C is the stiffness matrix.

If the material is modeled as transversely isotropic, there will be different  $\mu$  and  $\lambda$  depending on the direction, perpendicular ( $\perp$ ) or parallel ( $\parallel$ ) to the fibers.

The stiffness matrix for a transverse isotropic material results:

$$\mathbf{C} = \begin{bmatrix} (2\mu_{\perp} + \lambda_{\perp}) & \lambda_{\perp} & \lambda_M & 0 & 0 & 0 \\ \lambda_{\perp} & (2\mu_{\perp} + \lambda_{\perp}) & \lambda_{\perp} & 0 & 0 & 0 \\ \lambda_M & \lambda_M & (2\mu_{\parallel} + \lambda_{\parallel}) & 0 & 0 & 0 \\ 0 & 0 & 0 & 2\mu_{\parallel} & 0 & 0 \\ 0 & 0 & 0 & 0 & 2\mu_{\parallel} & 0 \\ 0 & 0 & 0 & 0 & 0 & 2\mu_{\perp} \end{bmatrix} \quad (4.31)$$

where  $\mu_{\perp}$ ,  $\mu_{\parallel}$ ,  $\lambda_{\perp}$  and  $\lambda_{\parallel}$ , are the real parts respectively of  $\mu$  and  $\lambda$ , and  $\lambda_M$  is the compressional modulus that includes both  $\lambda_{\perp}$  and  $\lambda_{\parallel}$ .

The damping matrix  $\mathbf{D}$  is the same matrix, but with  $\mu_{\perp}$  and  $\mu_{\parallel}$  that are the imaginary part of  $\mu$ .

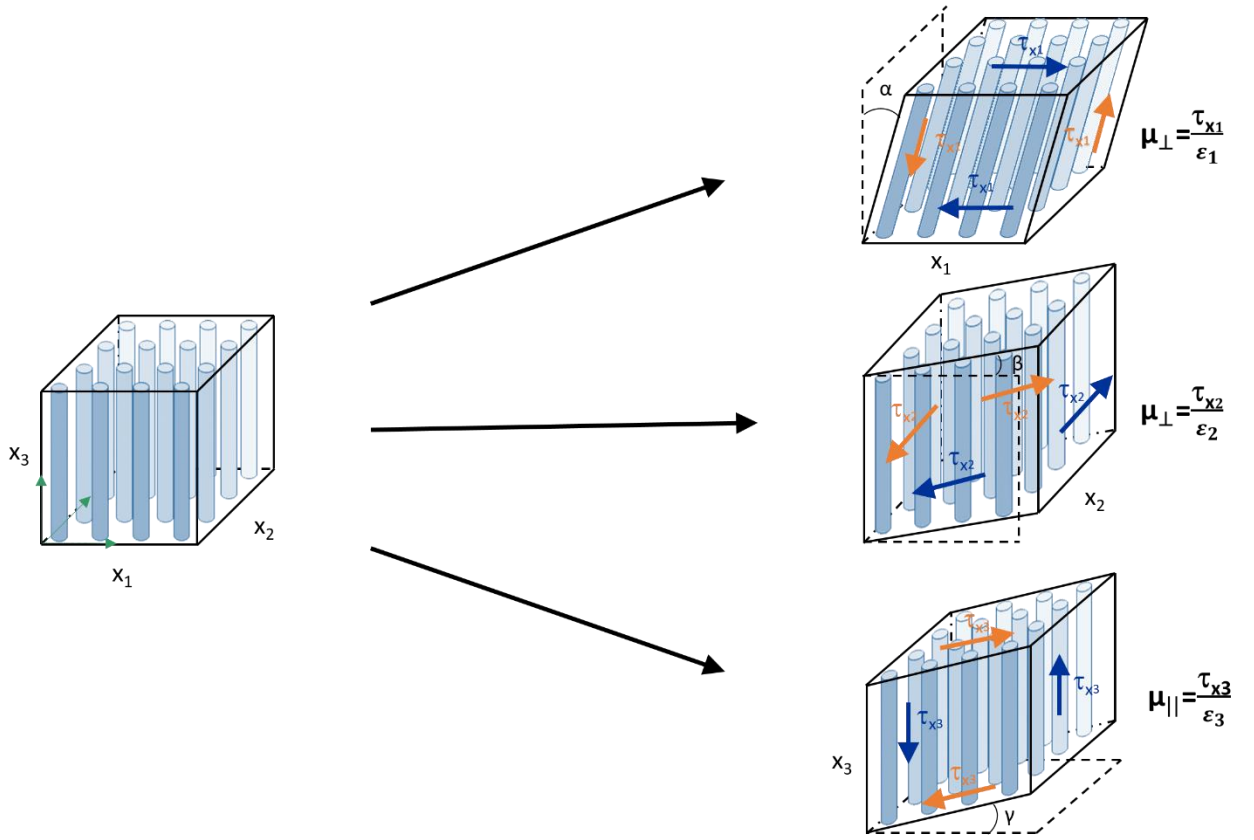


Figure 9: Ideal experiments to quantify the shear moduli of a transverse isotropic material having fibers in  $x_3$  direction: the planes of symmetry are about  $x_3$  axis and the plane of isotropy is in  $x_1$ - $x_2$  plane. First two experiments allow for the evaluation of  $\mu_{\parallel}$ , while the third returns  $\mu_{\perp}$ .

For a general viscoelastic, anisotropic and locally homogeneous material, the constitutive equation of motion describes the relation between the resultant strain due to an applied stress, and is given by two 4<sup>th</sup>

order tensors ( $C=C_{ijkl}$  and  $D=D_{ijkl}$ ) with up to 36 independent quantities with hypothesis of linearity and small deformations and up to 21 independent quantities because of symmetry [41].

Substituting equation 4.30 into equation 4.6 the following equation of motion is obtained:

$$\rho \frac{\partial^2 u_i}{\partial t^2} = \frac{\partial (C \varepsilon_{kl} + D \dot{\varepsilon}_{kl})}{\partial x_j} \quad (4.32)$$

$$\rho \frac{\partial^2 u_i}{\partial t^2} = C_{ijkl} \frac{\partial^2 u_l}{\partial x_j \partial x_k} + D_{ijkl} \frac{\partial^3 u_l}{\partial t \partial x_j \partial x_k} \quad (4.33)$$

where the indices i, j, k, l run from 1 to 3,  $\rho$  is the density of the medium and  $u_i$  denotes the  $i$ th component of the displacement vector  $u(x,t)$ .

This equation is obtained from the equilibrium above if, because of the assumption of local homogeneity, derivatives in space of the viscosity and elasticity tensors vanish.

The assessment of all the 21 unknown parameters for each tensor is above the number of equations of the MRE experiment. So it is useful to use a simplified model for the analysis, being the transverse isotropic model. If also symmetry of the viscoelastic model is assumed it is possible to reduce the number of unknowns, as said above, to 5 independent parameters ( $\mu_{\perp}$ ,  $\mu_{||}$ ,  $\lambda_{\perp}$ ,  $\lambda_{||}$ ,  $\lambda_M$ ).  $\lambda = \lambda_{\perp} = \lambda_{||} = \lambda_M$  since in biological tissues there are only one longitudinally polarized compressional wave and two transversely polarized shear waves, resulting from the Christoffel tensor eigenvectors and eigenvalues. Defining  $\tau = \mu_{||} - \mu_{\perp}$  [42], and assuming  $u_{j,ji} = 0$  because of incompressibility, the equations of motion can be rewritten as:

$$\mu u_{i,jj} + (\lambda + \mu) u_{j,ji} = \rho \frac{\partial^2 u_i}{\partial t^2} \quad (4.34)$$

$$\rho \frac{\partial^2 u_i}{\partial t^2} = \mu_{\perp} u_{i,jj} + \tau \left[ \frac{\partial^2 u_1}{\partial x_3^2} + \frac{\partial^2 u_3}{\partial x_1 \partial x_3} \right] + \eta \frac{\partial}{\partial t} u_{i,jj} \quad (4.35)$$

Applying the curl operator to eliminate the pressure term, and passing to the frequency domain, the Helmholtz type equation, that contains only shear wave contribution and permits the estimation of the shear viscoelastic parameters with third order derivatives in space, is obtained.



$$-\rho\omega^2 q_i \cong \mu_{\perp} q_{i,jj} + \tau \left[ \begin{array}{c} \frac{\partial^3 u_1}{\partial x_3^3} - \frac{\partial^3 u_3}{\partial x_1 \partial x_2^2} - \frac{\partial^3 u_3}{\partial x_1^3} \\ \frac{\partial^3 u_3}{\partial x_1^2 \partial x_2} + \frac{\partial^3 u_3}{\partial x_2^3} - \frac{\partial^3 u_2}{\partial x_3^3} \\ u_{3,jj} \end{array} \right] + i\omega\eta \frac{\partial}{\partial t} q_{i,jj} \quad (4.36)$$

$$\text{where } q_i = \varepsilon_{ijk} \frac{\partial u_k}{\partial x_j}$$

The application of the curl operator has led to have third-order spatial derivatives.

Finally, an optimization algorithm, as the one described in [34], can be used to obtain the parameters of interest.

#### **4.5 Direct problem, continuum formulation**

As mentioned in the previous sections, the inversion algorithms, in particular the Helmholtz inversion, rely on rather radical assumptions that are not met under ordinary experimental conditions, let alone in the biological environment [33]. It is thus worthwhile to gain better insight into the dynamics of wave propagation in anisotropic and viscoelastic materials by approaching the problem from the opposite point of view: understanding how the previously mentioned properties affect wave propagation in the material, instead of inferring the properties of the material from the knowledge of the displacement field and its time derivatives.

## CHAPTER 5


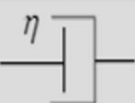
### VISCOELASTIC RHEOLOGICAL MODELS

As shown before there are two kinds of approach to the elastographic problem: direct and inverse. In the first one material mechanical properties as function of frequency are known a priori or they are fitted to a material model describing the stress-strain relation. Many real objects show a stress-strain behavior characteristic of both solids and liquids: these kind of materials are called viscoelastic. After a brief overview of the basic rheological models, the fractional Voigt model is presented. This model has been shown to be the best in the ability to fit, for a given frequency bandwidth, complex shear modulus values obtained from experiments [19].

#### 5.1 Basic rheological elements

In TABLE I two basic rheological elements are schematized. As it can be seen in the table, the correspondent stress-strain relationships in frequency domain are mathematically simple, so they can be used to build more complicated stress-strain relations of higher order rheological models.

TABLE I: CONSTITUTIVE EQUATIONS DESCRIBING STRESS-STRAIN RELATIONS OF ELEMENTARY VISCOELASTIC MODELS WHERE  $E$  AND  $\eta$  ARE RESPECTIVELY THE ELASTICITY CONSTANT AND THE DAMPING COEFFICIENT.

	Time domain	Frequency domain
<b>Spring</b> 	$s_s(t) = E e_s(t)$	$\sigma_s(\omega) = E \varepsilon_s(\omega)$
<b>Dashpot</b> 	$s_D(t) = \eta \frac{d}{dt} e_D(t)$	$\sigma_D(\omega) = i\omega\eta\varepsilon_D(\omega)$

Ideal elastic materials accumulate energy of deformation and release it without losses. This behavior can be described by the Hooke's law relative to a simple spring with a constant between stress and strain described by the elastic modulus (shear or Young's modulus depending on the kind of stress applied).

A material can also attenuate motion or mechanical energy and the energy is usually lost as heat; in this case the basic rheological element is the dashpot and its stress-strain relation obeys Newton's fluid model with a viscosity constant between stress and the time derivative of strain. It is possible to see how the derivative in time domain becomes a simple multiplication of the damping coefficient by the imaginary unit and the angular frequency in the frequency domain.


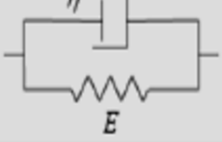


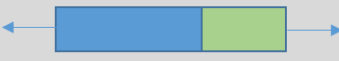
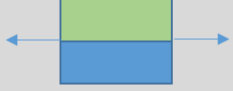
## **5.2 Complex modulus estimation for some linear viscoelastic models**

In order to derive the rheological constitutive equations for viscoelastic materials, it is possible to combine these three basic elements in series or in parallel so to obtain a more accurate description of the real behavior as shown in TABLE II.

Adding more rheological elements it is possible obtain a more accurate representation of the reality, but at the same time the stability of the problem can be lost since, to describe the complex model, a high number of independent parameters is used.

It has been demonstrated that, for elastographic experiments, a good compromise can be a model with two/three independent parameters [4].

TABLE II: SUMMATION RULES IN LINEAR VISCOELASTICITY TO FORM COMPLEX MODELS COMPOSING THE SUB-RHEOLOGICAL ELEMENTS.  $\sigma_k$  AND  $\varepsilon_k$  ARE RESPECTIVELY THE STRESS AND THE STRAIN OF SUB-RHEOLOGICAL ELEMENTS.

	Serial arrangement	Parallel arrangement
		
Rest condition		
Deformed condition		
	$\varepsilon = \sum_k \varepsilon_k$ $\sigma = \sigma_k$	$\varepsilon = \varepsilon_k$ $\sigma = \sum_k \sigma_k$

### 5.2.1 Maxwell model

The Maxwell model (Figure 10) can be exemplified with a purely viscous damper connected in series with a purely elastic spring.

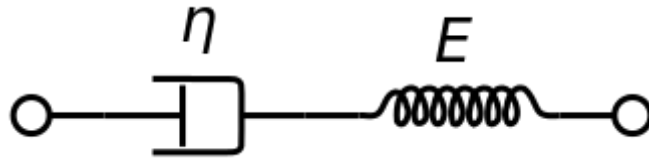


Figure 10: Maxwell Model.

The stress  $\sigma$ , the strain  $\varepsilon$  and their time derivatives, in a Maxwell material, are governed by equations of the form [43] :

$$\frac{\dot{\sigma}}{E} + \frac{\sigma}{\eta} = \dot{\varepsilon} \quad (5.1)$$

Since the total strain is the summation of the individual elements strain:

$$\varepsilon = \varepsilon_S + \varepsilon_D = \frac{\sigma_S}{E} + \frac{\sigma_D}{i\omega\eta} = \sigma \left( \frac{1}{E} + \frac{1}{i\omega\eta} \right) \quad (5.2)$$

$$\mu = \frac{\sigma}{\varepsilon} = \frac{1}{\left( \frac{1}{E} + \frac{1}{i\omega\eta} \right)} = \frac{Ei\omega\eta}{i\omega\eta + E} \quad (5.3)$$

with the real and imaginary part of G being:

$$\mu_R = \frac{\omega^2\eta^2 E}{E^2 + \omega^2\eta^2} \quad (5.4)$$

$$\mu_I = \frac{\omega\eta E^2}{E^2 + \omega^2\eta^2} \quad (5.5)$$

### 5.2.2 Voigt model

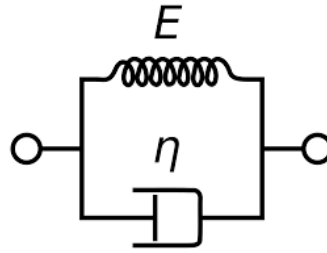


Figure 11: Voigt Model.

The Voigt model (Figure 11) can be described by a purely elastic spring in parallel with a purely viscous damper. In this case the material's governing equation is [43]:

$$\sigma(t) = E\varepsilon(t) + \eta \frac{d\varepsilon(t)}{dt} \quad (5.6)$$

The total stress is shared between the two elements:

$$\sigma = \sigma_S + \sigma_D = E\varepsilon_S + i\omega\eta\varepsilon_D = (E + i\omega\eta)\varepsilon \quad (5.7)$$

$$\mu = E + i\omega\eta \quad (5.8)$$

with the real and imaginary part of G being:

$$\mu_R = E \quad (5.9)$$

$$\mu_I = \omega\eta \quad (5.10)$$

### 5.3 Fractional viscoelasticity and springpot model



Figure 12: Springpot model (single fractional element).

A material can also have an intermediate behavior between ideal elastic and purely viscous. Rather than arranging the viscous and elastic elements in series or in parallel, the stress strain relationship could also be described through the Springpot model (Figure 12). It generalizes these elements by defining a constitutive law in which the stress in the element is directly proportional to the  $\alpha$ -th order derivative of the strain [44] (Figure 13):

$$\sigma(t) = V \frac{d^\alpha \varepsilon(t)}{dt^\alpha} \quad (5.11)$$

where  $V$  is a proportionality constant. Passing to Laplace domain, it is possible to write the relaxation modulus  $m$  of the material as [44] [45]:

$$m(s) = \frac{\sigma(s)}{\varepsilon(s)} \quad (5.12)$$

and, assuming that the viscoelastic material has a power-law response such as:

$$\mu(t) = \frac{E}{\Gamma(1-\alpha)} \left(\frac{t}{\tau}\right)^{-\alpha} \quad (5.13)$$

where the Gamma function is defined as:

$$\Gamma(z) = \int_0^{+\infty} t^{z-1} e^{-t} dt \quad (5.14)$$

The relaxation modulus and the stress expressions respectively become:

$$m(s) = E(s\tau)^\alpha \left(\frac{1}{s}\right) \quad (5.15)$$

$$\sigma(t) = E\tau^\alpha \frac{d^\alpha \varepsilon(t)}{dt^\alpha} \quad (5.16)$$

where  $s$  is the ratio of the shear viscosity to Young modulus.

The Springpot model is formally proposed as a three parameters model, but actually it is a two parameters model, because one of the three material properties is kept constant. The three parameters are  $\mu$ ,  $\eta$  (usually the one kept constant) and  $\alpha$ . The last parameter has a value comprised between 0 and 1 since it can be

interpreted as an interpolation constant parameter between the true elastic (if  $\alpha = 0$ ) and the viscous (if  $\alpha = 1$ ) cases.

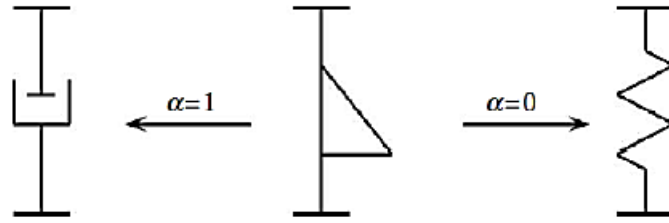


Figure 13: The Springpot model can be seen as an element whose behavior approaches a spring or a dashpot for  $\alpha$  that respectively goes to 0 or to 1.

This model can be also reformulated as a two parameters model introducing the parameter  $k$ :

$$k = \mu \eta^{\frac{\alpha}{1-\alpha}} \quad (5.17)$$

and in this case the Springpot power-law in the compressed notation is

$$\mu = k(i\omega)^{\alpha} \quad (5.18)$$

Viscosity parameters are linked to geometry as branches shape and their organization in the hierarchical network and the network shape, while the global effective elastic modulus gives how much the diseases can modify the number and the strength of crosslinks of the biological tissue mechanical matrix.

The two viscoelastic power-law constants of the Springpot model provide a relation between tissue structure and network topology [46].

The Springpot model, with only two parameters,  $\alpha$  and  $k$ , describes the increase of two functions in function of frequency  $\omega$ , the loss modulus ( $\mu_I$ ) and the storage modulus ( $\mu_R$ ).

In the frequency domain the constitutive equation becomes:

$$\sigma(\omega) = \mu_{\alpha}^{1-\alpha} (i\omega\eta)^{\alpha} \varepsilon(\omega) \quad (5.19)$$

$\mu_{\alpha}$  and  $\alpha$  can be related to structural changes patterns; therefore, these parameters have a physical meaning related to the structural properties of the material, outlining a relationship between histology and elastography parameters (Figure 14).

The Springpot describes the link between fractal geometry of structures and the measured complex shear stiffness.

Structures with fractal characteristics present self-similar geometrical replication in different hierarchical levels of a continuum. This identical geometrical pattern repetition in a continuity of scales can be easily treated with a mathematical representation of complex structures in hierarchical systems.

If the tissue is structured in a fractal way,  $\mu_\alpha$  is defined as viscoelastic connectivity between the individual elements and it increases as the tissue gets stiffer. On the other hand,  $\alpha$  is defined as matrix geometry and is related to the geometrical reordering of the structure. In the case of the skeletal muscle, it increases if the muscle is in an active state with respect to the passive one due to the additional cross-links generated during the fibers recruitment. Instead, this parameter doesn't increase in case of stiffening of the tissue. Matrix connectivity can therefore be interpreted as a measure of the geometrical alignment of the basic rheological elements at the multiscale [4].

This approach can be useful in the case of elastographic mathematical modeling, since it is a multiscale technique.

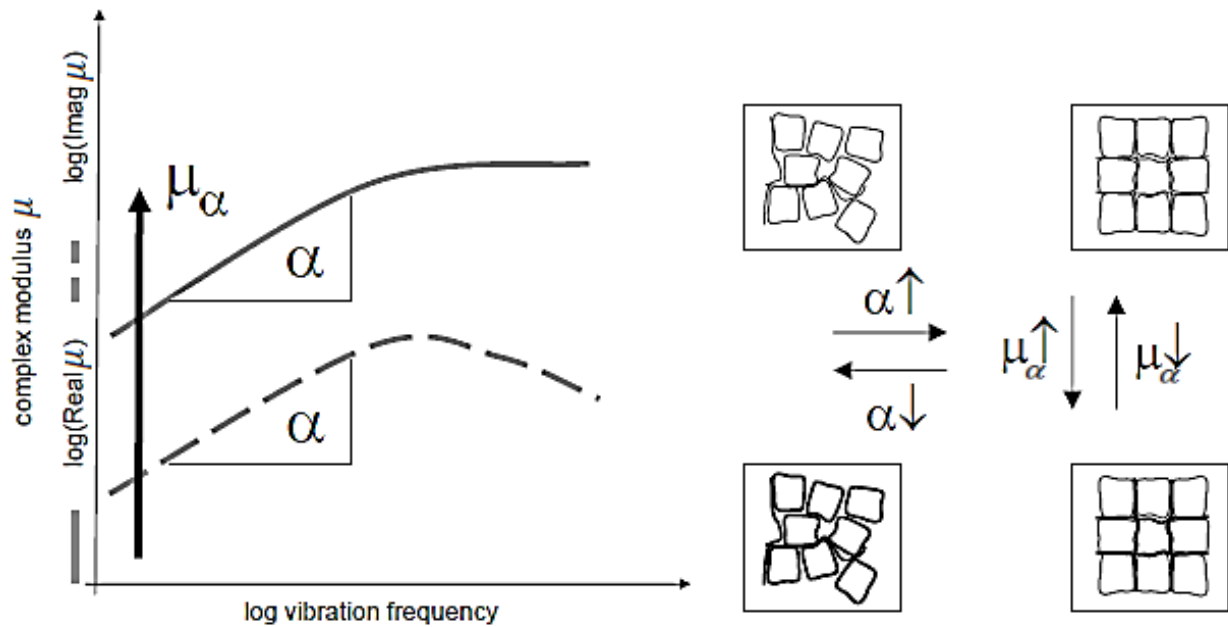


Figure 14: The parameters  $\mu_\alpha$  (viscoelastic connectivity) and  $\alpha$  (matrix geometry) of the Springpot model can be seen as describing the structural properties of the material: while  $\mu_\alpha$  is akin to an ordinary stiffness,  $\alpha$  describes the matrix geometry: values of  $\alpha$  closer to 1 indicate a more organized and structured material. Provided by Ingolf Sack.



The real and imaginary parts of  $\mu$  for the Springpot model are:

$$\mu_R = \mu_\alpha \omega^\alpha \cos\left(\frac{\pi}{2}\alpha\right) \quad (5.20)$$

$$\mu_I = \mu_\alpha \omega^\alpha \sin\left(\frac{\pi}{2}\alpha\right) \quad (5.21)$$

### 5.3.1 Fractional Voigt model

The newly defined Springpot element can be arranged in series or parallel with springs and/or dashpots: indeed, the fractional order Voigt model (Figure 15) is the conventional Voigt model, in which the dashpot has been substituted with a Springpot.

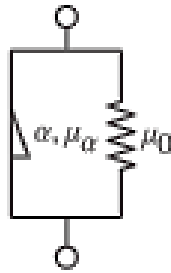


Figure 15: Fractional Voigt model.

In this case the storage and the loss moduli are defined as [47]:

$$\mu_R = \mu_0 + \mu_\alpha \omega^\alpha \cos\left(\frac{\pi}{2}\alpha\right) \quad (5.22)$$

$$\mu_I = \mu_\alpha \omega^\alpha \sin\left(\frac{\pi}{2}\alpha\right) \quad (5.23)$$

## CHAPTER 6

### MATERIALS AND METHODS

#### 6.1 Sample preparation

Three kinds of sample were examined for MRE experiments:

1. Isotropic homogeneous Gelatin hydrogel 10% w/v phantom.
2. Isotropic homogeneous Poly Vinyl Alcohol hydrogel 10% w/v phantom.
3. Anisotropic phantom composed by two parts:
  - Internal phantom: cylindrical sample consistent in a composite material made of a poly vinyl alcohol hydrogel 10% w/v matrix and four inclusions of Spandex fibers (*Stretch Magic Bead and Jewelry Cord by Pepperell, diameter of 0.5 mm*).
  - External matrix: homogeneous Gelatin hydrogel 10% w/v.

##### 6.1.1 Internal phantom construction for anisotropic sample

The preparation of the anisotropic sample is divided into different steps:

- Use a glass tube (*Soda line glass, outer diameter of 9.5 mm and inner diameter of 8 mm by Dispo® culture tubes*) with bottom removed and put two plastic caps on both ends. The top cap must have five drilled holes, four in order to make way for the fibers to be positioned inside the tube and one to pour the PVA hydrogel after the positioning of the fibers. Instead the bottom cap must have only four drilled holes.
- Using a capillary (diameter of 0.6 mm approximately), stick the Spandex fiber inside the tube starting from the top end. Repeat the sewing procedure in the opposite direction from the bottom and then tie a knot of the two extremities of the thread on the top cap. Repeat the procedure another time in order to position the four fibers in straight way inside the tube.

- So to avoid that the mixture spills out from the tube bottom, the last one is placed vertically and the bottom is sealed using some clay and laboratory parafilm (BEMIS®, WI, USA). They are removed after the two cycles of freezing/thawing before taking out the sample from the test tube.
- Prepare the matrix solution to pour around the fibers. A water-soluble synthetic polymer (*Poly(vinyl alcohol)*, Consolidated Chemicals & Solvents LLC, 44.05 g/mol) was selected as matrix for the anisotropic phantom construction due to its reasonable stability over time, durability and tissue mimicking properties. Moreover, PVA sticks well to Spandex fibers and it is easy to remove from the glass tube, despite some disadvantages due to the fact that it forms a lot of bubbles and it is time consuming to prepare since it needs two freezing/thawing cycles. 10% w/v PVA gel is prepared in 20 ml of distilled water (Refreshe, purified by steam distillation, filtered and ozonated to ensure quality) stirring on a hotplate at 80-90 °C for 5 minutes. Since it becomes solid in few minutes, it must be poured when it is still liquid inside the test tube.
- Inject slowly the liquid solution of PVA from the fifth hole on the top cap using a needle of PTFE (1 ½" long, gauge 16, McMaster-CARR®) with a 5 ml syringe in order to minimize air bubbles forming into the sample.
- Before removing the caps and the sample from the test tube, perform two cycles of freezing and thawing on the sample.

### **6.1.2 External matrix construction for anisotropic sample**

10% w/v Gelatin gel is prepared in 20 ml of distilled water (Gelatine, Knox, original unflavored) stirring on a hotplate at 80-90 °C for 5 minutes.

### **6.1.3 Assembling of the external matrix with the internal phantom**

For the MRE experiment a glass tube (*Soda line glass, outer diameter of 9.5 mm and inner diameter of 8 mm by Dispo® culture tubes*) is used. Gelatin solution is poured until a certain height (about 0.5 cm from the bottom in order to reach the field of view) and is let solidify, then a slice of the anisotropic phantom with fibers is cut and positioned so that the fibers lay horizontally. Subsequently other Gelatin solution is poured in order to fill the empty spaces and the tube up to the top.

A picture of the final test tube is reported in Figure 16, while a schematization of the same configuration is provided in Figure 17.



Figure 16: Picture of the anisotropic phantom inside the test tube. Externally the transparent gelatin matrix, inside the PVA matrix with four Spandex fibers inside positioned horizontally.

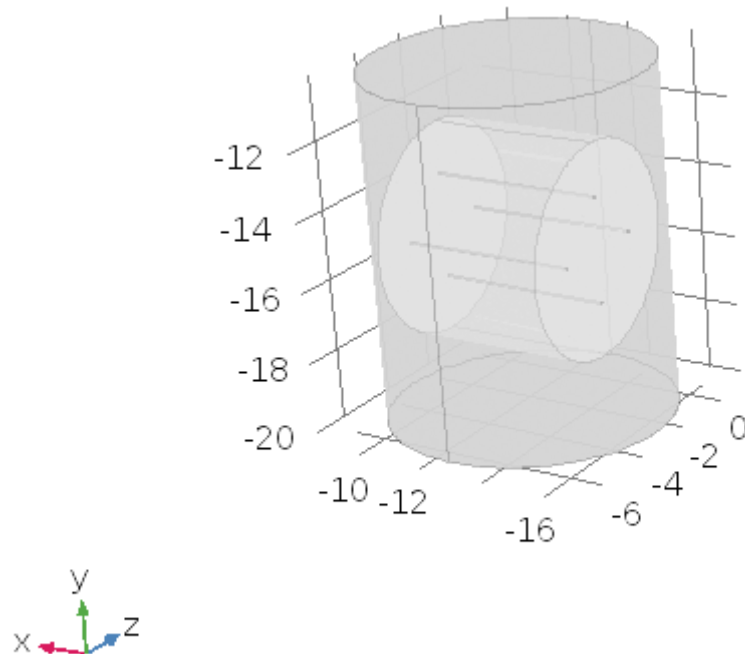


Figure 17: Schematization of the model for anisotropic phantom reported in Figure 16. Externally the transparent gelatin matrix, inside the PVA matrix with four Spandex fibers inside positioned horizontally.

## **6.2 Electro-mechanical setup and mechanical actuation**

A 56-mm vertical bore MR scanner was used for MRE experiments (Bruker 11.74 Tesla, Billerica, MA).

It has a 10 mm RF coil and 19 mm gradient coils (3000 mT/m of maximum strength or 2000).

The samples positioned inside a test tube of 8.8 mm of diameter were scanned for a 1 kHz to 8 kHz frequency range with spacing of 1 kHz with a Bruker RF coil having a 10 mm seat.

The lower frequency limit is determined by the ratio between the diameter of the sample and the shear wavelength so to have an interpretable shear wave propagation pattern, while the upper frequency limit is due to increased attenuation because of high frequency waves with consequently decrease in the SNR of the wave image.

For the experiment was selected a piezoceramic stack actuator (6.5×.5×18 mm, Thor Labs. Inc) providing 11.6  $\mu\text{m}$  displacement amplitude at 100 Volts.

The piezoelectric actuator is mounted on an assembly constituted by a plastic cradle that, through a tube holder and a plastic rod, connects to the test tube.

The MRI system generates a trigger signal that is fed into the “Trigger Input” of the function generator (Function Waveform Generator, 33250A, 80 MHz, Agilent Technologies Test and Measurement, Englewood, CO). Then a precise number of sinusoidal waveforms is sent to the power amplifier (Power Amplifier, P3500S, Yamaha Corporation of America, Buena Park, CA).

In order not to damage the piezoelectric actuator with a negative voltage across its terminals it is necessary to add a DC bias to the output of the power amplifier through connection in series with a DC supply (Power Supply, E3634A 200W, Agilent Technologies Test and Measurement, Englewood, CO).

The configuration is thus the following one: the DC power supply negative terminal is connected to the piezo stack negative terminal while the power amplifier positive terminal is connected to the piezo positive terminal.

The actuator excites the entire test tube vertically and this motion generates shear waves that circularly propagate in a focusing fashion from the external boundary of the sample to the center of the test tube since the Gelatin clings well to the test tube wall after curing process.

In order to minimize the compression wave effect MRE analysis was conducted on cylindrical tubes with both ends open. The test tube chosen for the experiment was the Borosilicate Glass NMR tube since it has high stiffness which implies high resonant frequencies with respect to experimental mechanical frequencies of MRE. In this way the tube acts as a rigid body oscillating axially.

The MRE experiment was performed using Paravision 4 (Bruker, Billerica, MA, USA).

A gradient echo SLIM MRE pulse sequence system [48] was chosen for studies in the 11.74 T. The imaging parameters were the following: image acquisition matrix=128×128, FOV=10 mm for sample of 8.8 mm of diameter, slice thickness=1 mm, MEG strength = 1200 mT/m and eight time offsets.

The actuator was triggered 20 ms previously the activation of the MEG pulse so that the sample reaches steady states.

While parameters like MEG duration and gradient power on slice direction, repetition time (TR), flip angle (FA) and time echo (TE) were set for each frequency as reported below:

TABLE III: SETTING PARAMETERS FOR MRE EXPERIMENT.

Frequency range [Hz]	Repetition time TR [ms]	Echo time TE [ms]	Flip angle FA [degrees]	Gradient power [Gauss/cm]	MEG duration [ms]
1000-3500	120	3.95	30	75	2
4000-7500	150	3.95	30	75	2
8000	150	3.95	30	75	1

This kind of study allows the simultaneous acquisition (SLIM) MRE [48] pulse sequence able to get 3D motion in one scan but, since in this case the interest was limited to observe wave propagation in the plane perpendicular to z direction (excitation direction), the motion was encoded concentrating the gradient power all in the slice direction (50%).

Basing on geometrical focusing method, the cylindrical tube is subject to steady state harmonic vertical motion,  $u_z = u_{za} e^{j\omega t}$  and it creates shear waves that propagate from the wall of the cylinder towards the central axis of the cylinder. Exploiting this kind of cylindrical wave propagation, characteristic of geometrical focusing phenomenon, it is possible to contrast the attenuation occurring in planar wave propagation and even to obtain an amplification of the wave at the center of the cylinder.

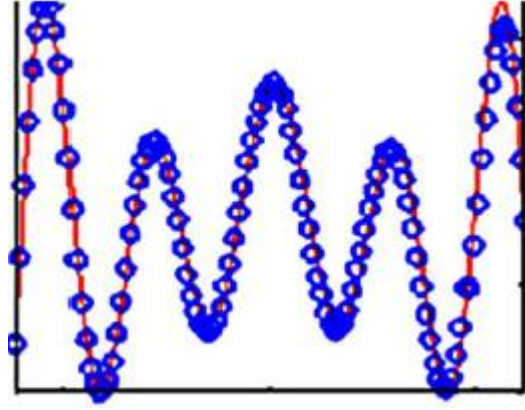


Figure 18: Exemplificative example in which geometrical focusing phenomenon is visible.

For a viscoelastic, isotropic and homogeneous medium the displacement, far enough from the tube ends and seen as in function of the radial position, is given by the following formula:

$$u_z(r, t, k_\beta) = u_{za} \frac{J_0(k_\beta r)}{J_0(k_\beta a)} e^{j\omega t} \quad (6.1)$$

with  $k_\beta = \omega \sqrt{\frac{\rho}{\mu_R + j\mu_I}}$  being the surface wave number and  $J_0(z)$  being the Bessel function of the first kind 0<sup>th</sup> order, with  $j = \sqrt{-1}$ ,  $\rho$  the density and  $\mu_I$  and  $\mu_R$  the imaginary and real part of the shear stiffness [49].

For isotropic homogeneous phantoms 8 line profiles crossing the center spaced of 22.5° (see Figure 19) in the slice direction encoded complex wave image were saved for all the frequencies so to estimate the complex shear stiffness of the sample.

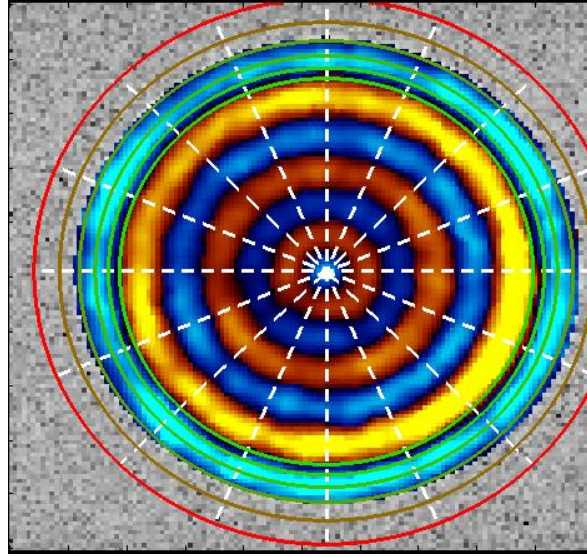


Figure 19: Screenshot of MRE deviant software for MRE experiments postprocessing in which 8 line profiles crossing the center spaced of  $22.5^\circ$  are taken [49].

Line profiles were matched with the analytical closed form solution of the cylindrical coordinate wave equation reported in equation 6.1. This way it is possible to calculate at every frequency imaginary and real parts of the complex shear stiffness through a customized Matlab code using “Global Optimization” toolbox to perform a nonlinear curve fitting routine for GFS (geometrical focusing surface waves) with a number of trials of 100.

Every profile is fit individually and then an average of both real and imaginary parts of the shear modulus for the 8 profiles at each frequency is taken.

The algorithm uses the objective function present in the work by Yasar et al [49]:

$$\hat{f}(r, \mu, \theta, \beta, s, \delta) = s * u_z(r + \delta, t, k_\beta(\mu)) * e^{-j\theta} + \beta \quad (6.2)$$

It takes into account some uncertainties such as:

- $s$ , the amplitude scale
- $\theta$ , the phase of the wave propagation to correct measurements made not at zero starting phase
- $\delta$ , symmetry shift, offset of the spatial position of the center of the experimental line profile since the central point of the wave pattern can be shifted by out of phase piezos
- $\beta$ , zero offset, bias represented by a complex value that compensates for reflected compression waves.



In the algorithm the nonlinear fitting function `lsqcurvefit` exploiting levenberg-marquardt method is implemented. It minimizes the following error function defined as the sum of the square of the absolute difference between estimated cylindrical wave equation closed form solution and the experimental data as an error function given by:

$$Err(\mu, \theta, \beta, s, \delta) = \frac{\sum_{n=-N}^N |f(r_n) - \hat{f}(r_n, \mu, \theta, \beta, s, \delta)|^2}{2N+1} \quad (6.3)$$

where  $r_n = \frac{n}{N}a$  with  $a$  that is the internal radius of the cylinder,  $2N+1$  that, considering the linear profile, is the total number of data points and  $n$  that indicates each data point.

This algorithm allows to estimate complex and unbounded parameters. Since significant attenuation at high frequencies occurred, due to the low SNR of experimental data and the high number of parameters, to stay away from any local minima, multiple random start points were chosen.

### **6.3 Computational simulation of MRE experiments**

In the present section a direct approach of MRE problem (section 4.5) will be analyzed thus modeling the geometry of the previously mentioned phantoms, assigning the material properties of the materials obtained from postprocessing of MRE experiments on the phantoms themselves and simulating the wave propagation using COMSOL Multiphysics® 5.2a (Stockholm, Sweden) in order to obtain as output the wave images in the phantoms sections to compare with experimental MRE wave images.

In the case of isotropic and homogeneous phantoms as reported in point 1 and 2 in section 6.1 was possible to reduce computational time building the cylindrical model as a 2D rectangular axisymmetric model.

In the case of isotropic homogeneous Gelatin hydrogel 10% w/v phantom the following model of an axisymmetric cylinder with radius of 4 mm was implemented.

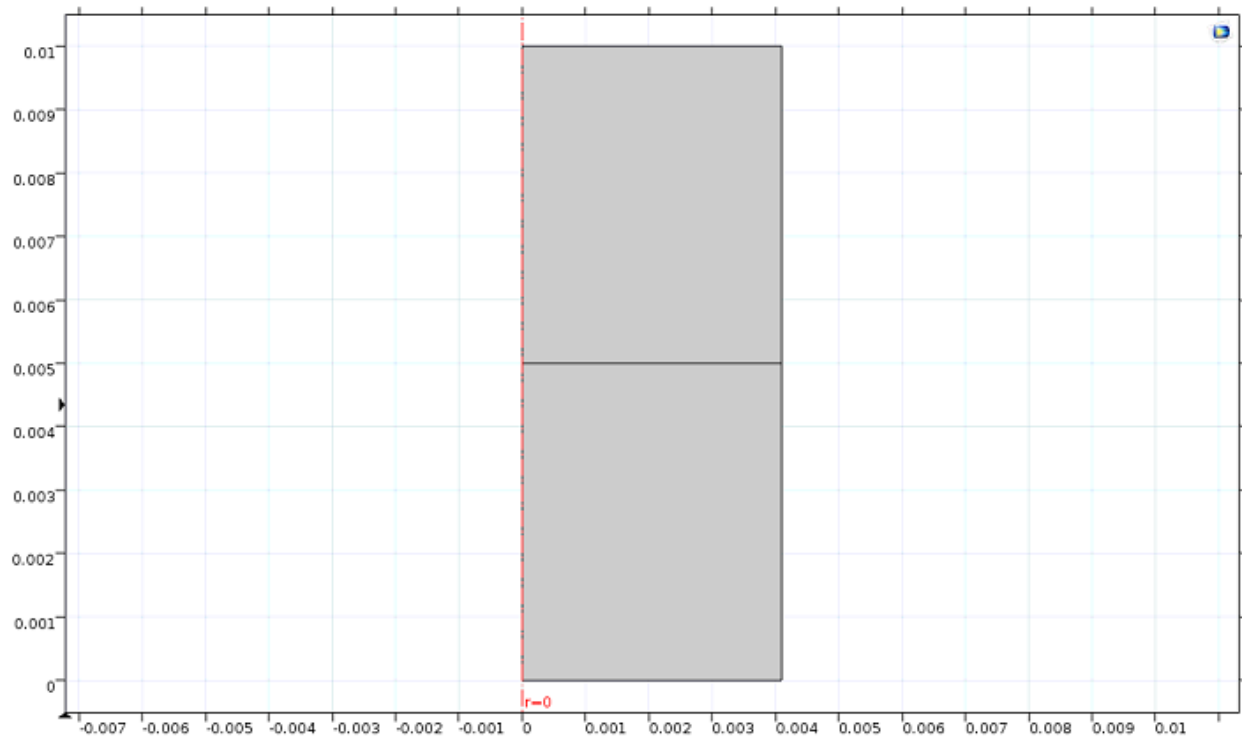


Figure 20: Model of an axisymmetric cylinder with radius of 4 mm for homogeneous isotropic gelatin. In the model geometry a line is taken at half height for postprocessing purposes.

A mesh of 10324 triangular elements with 5304 vertices was applied on the axisymmetric surface.

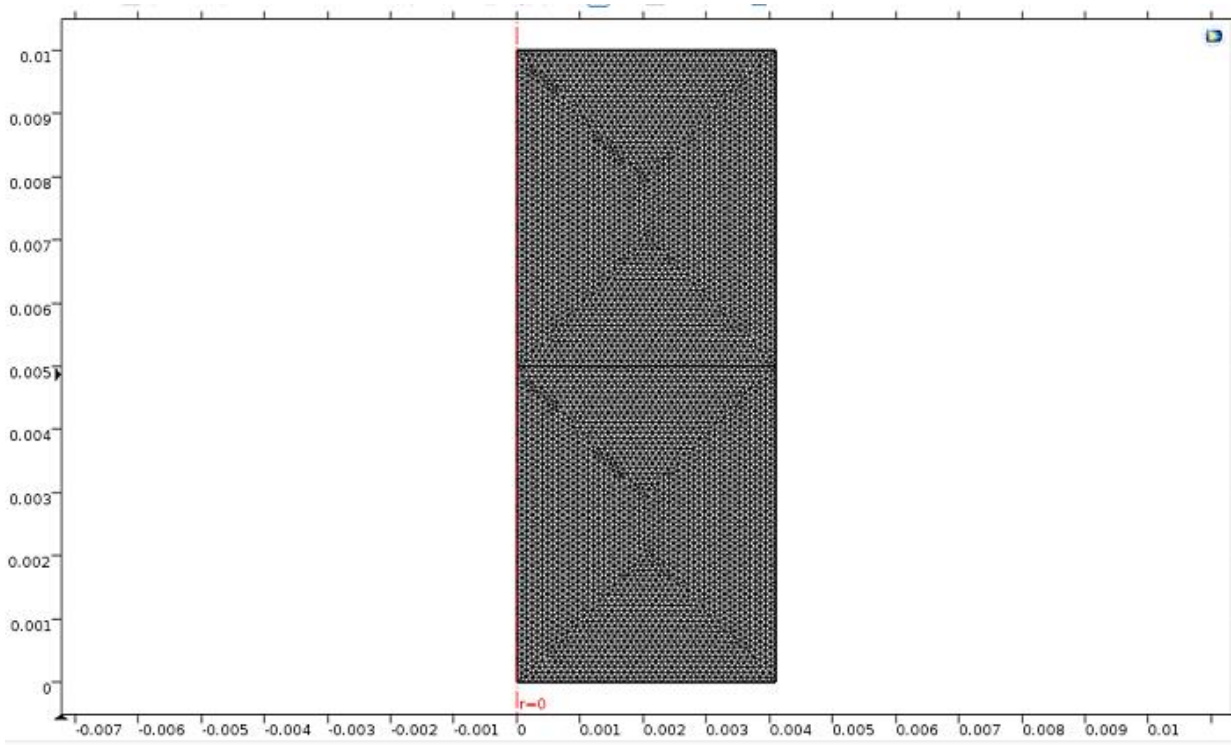


Figure 21: Mesh of 10324 triangular elements with 5304 vertices for model of an axisymmetric cylinder with radius of 4 mm for homogeneous isotropic gel.

The material properties associated to this model were obtained from postprocessing of MRE experiment on the phantom itself, thus following the direct approach of MRE problem.

In the case of the isotropic homogeneous Poly Vinyl Alcohol hydrogel 10% w/v phantom exactly the same geometric model was implemented applying on it different material properties.

In the case of the anisotropic phantom described in point 3 of section 6.1 the entire geometry was modeled using Solidworks (Dassault Systèmes, 1995) and then imported in Comsol Multiphysics 5.2a in which different material properties were assigned for the different parts (PVA, Gelatin and Fibers).

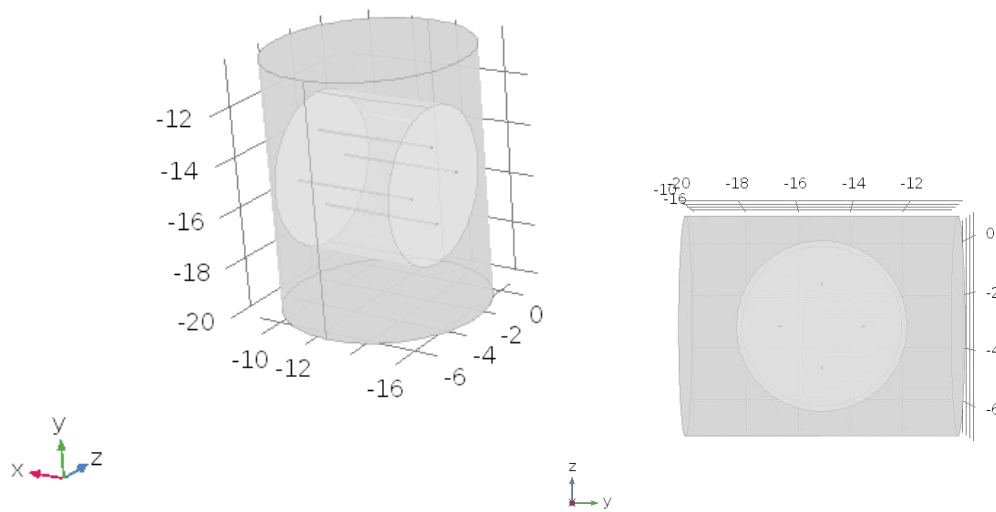


Figure 22: 3D model for anisotropic phantom with four fibers.

A mesh of 1131198 tetrahedral and 53112 triangular elements for the shell of the mesh was applied on the model.

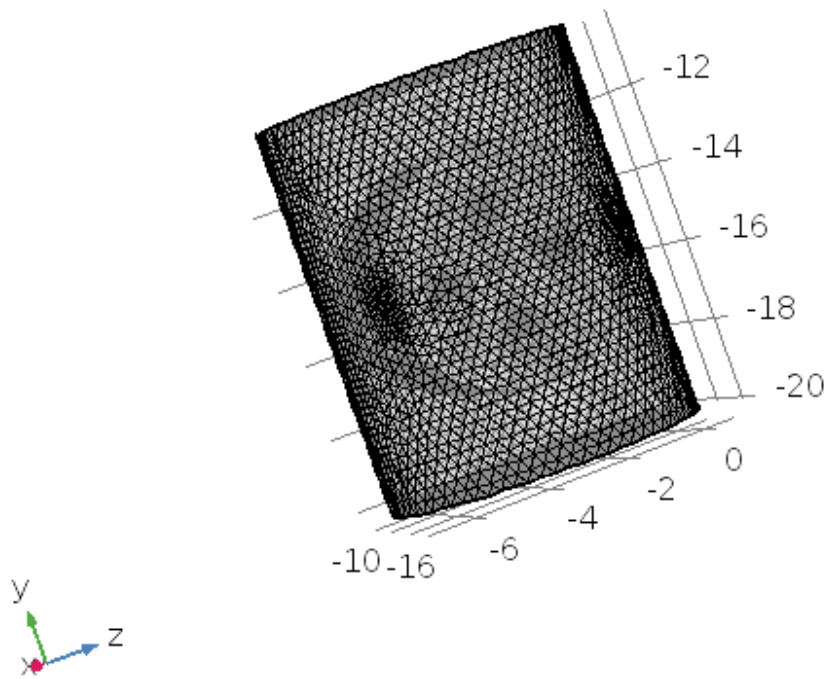


Figure 23: Mesh of 1131198 tetrahedral and 53112 triangular elements for anisotropic phantom with four fibers.

## CHAPTER 7

### RESULTS AND DISCUSSION

#### 7.1 Homogeneous and isotropic gelatin

The first sample analyzed was the homogeneous and isotropic gelatin described in point 1 of section 6.1.

In TABLE IV are reported the resultant wave images in slice direction from 1000 to 5000 Hz spaced by 1000 Hz.

As expected the wavefronts are circular and concentric; increasing the frequency of excitation the wavelengths are shorter so it is possible to see a higher number of wavefronts in the section of the sample.

In Figure 24 the shapes of the displacement curves in the direction perpendicular to the slice plane and relative to the different wave images for each frequency are reported. Values are normalized with respect to the maximum.

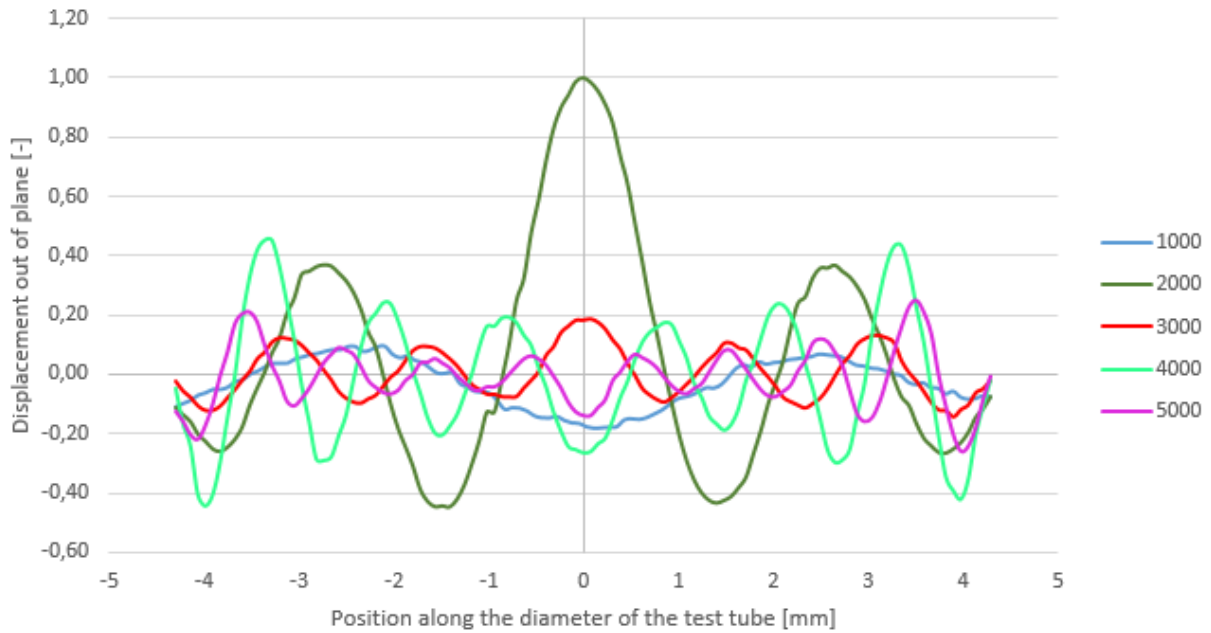


Figure 24: Experimental displacement profiles for homogeneous and isotropic gelatin in direction perpendicular to the slice plane along the diameter of the test tube.

The wave profiles are postprocessed as described in section 6.2 in order to obtain the values of  $\mu_R$  and  $\mu_I$  at each frequency as shown in Figure 25.

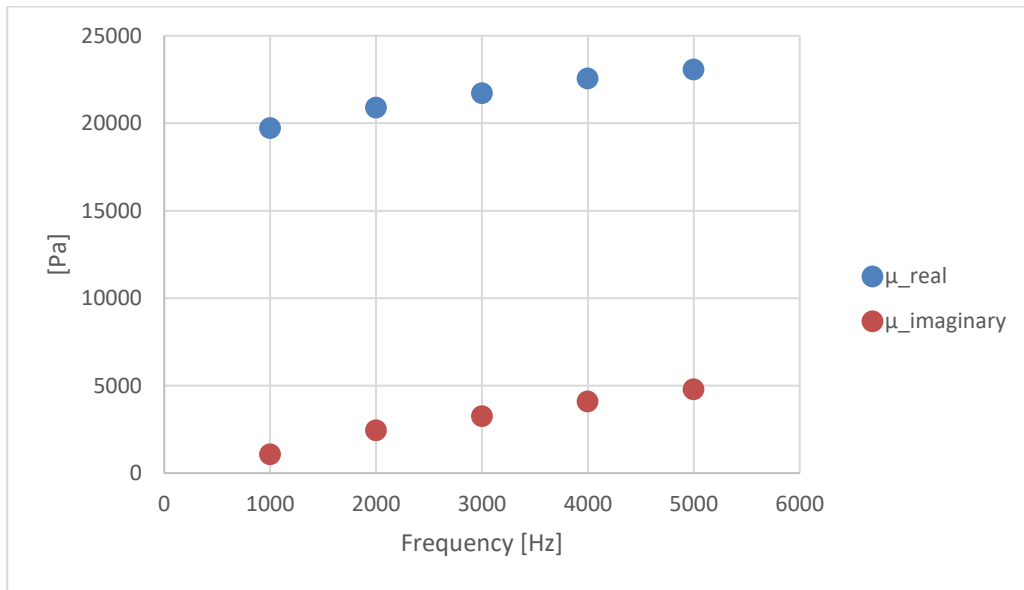


Figure 25: Identified values of  $\mu_R$  and  $\mu_I$  versus frequency for homogeneous and isotropic gelatin (see section 6.2).

The curves of  $\mu_R$  and  $\mu_I$  were separately fitted with a parabolic polynomial function to get the equation of each curve in function of frequency taking into consideration the standard deviation for each data point.

The standard deviations are due to the fact that in the MRE image slice 8 displacement profiles passing through the center of the slice are extracted for each frequency; each experimental profile is fitted separately with the closed form solution of the wave equation obtaining the correspondent  $\mu_R$  and  $\mu_I$  in that direction. Then the values for the 8 profiles are averaged in order to obtain a single value of  $\mu_R$  and  $\mu_I$  for each frequency.

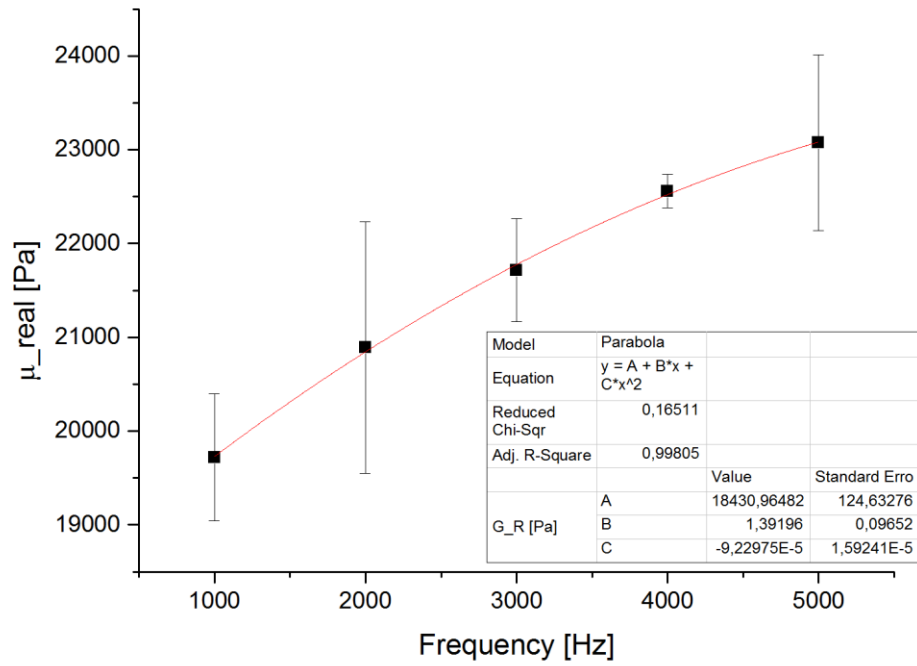


Figure 26: Curve fitting of the experimental data of  $\mu_R$  for homogeneous and isotropic gelatin with a parabolic curve.

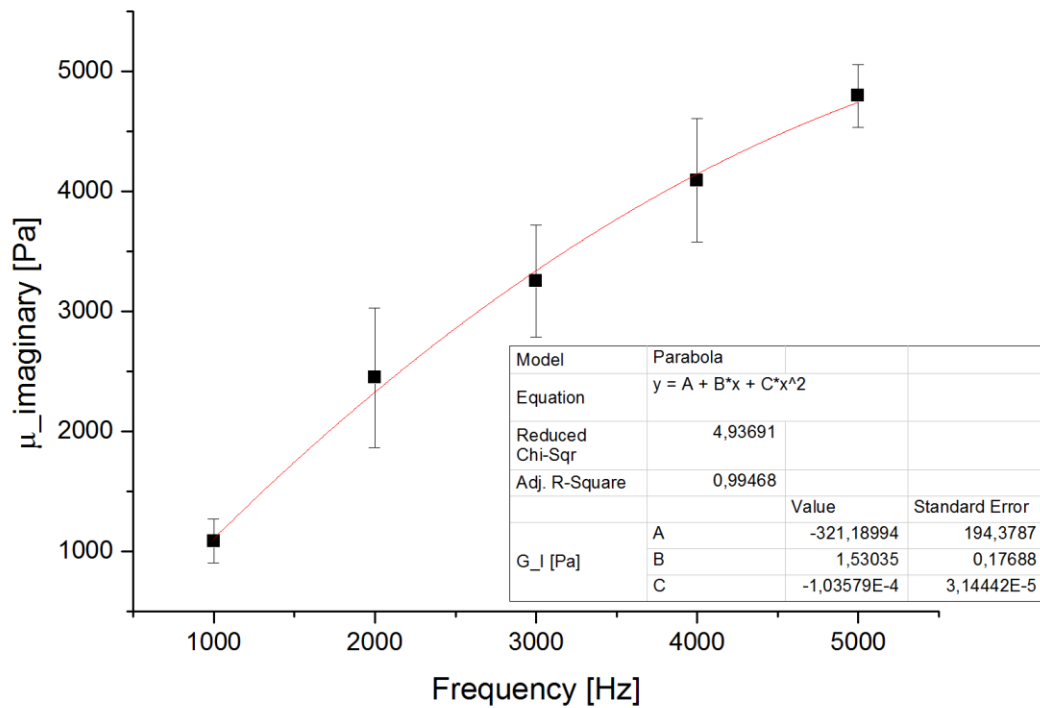


Figure 27: Curve fitting of the experimental data of  $\mu_I$  for homogeneous and isotropic gelatin with a parabolic curve.

In order to set the direct problem in Comsol to compare the wave images obtained from experiment with the computational ones, the resultant parabolic curves describing the behavior of  $\mu_R$  and  $\mu_I$  as a function of frequency were used as input for the material properties of the model implemented in Comsol.

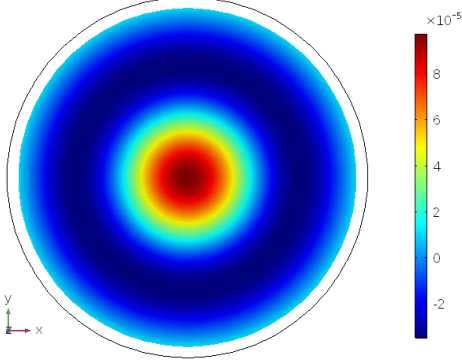
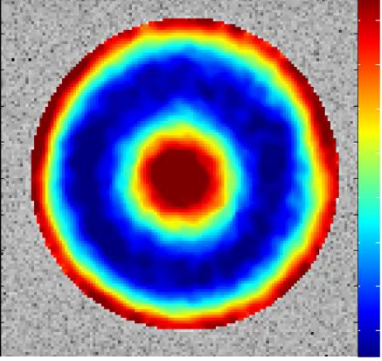
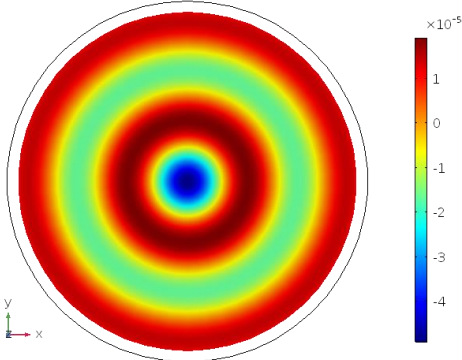
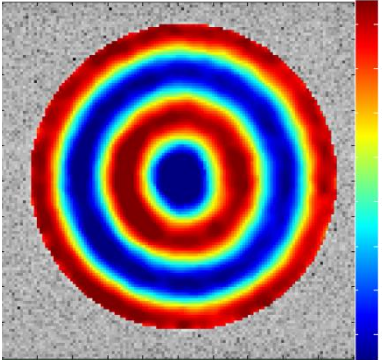
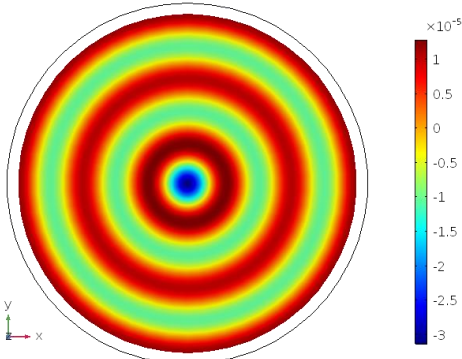
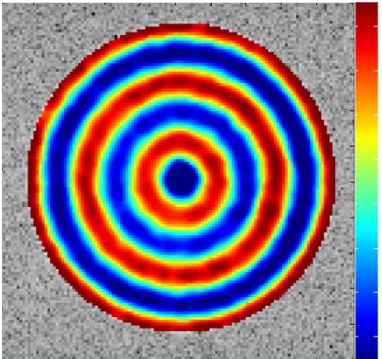
Setting a frequency domain simulation, it was possible to obtain the displacement field in time at different frequencies, induced by a harmonic displacement on the external boundary of the cylinder (amplitude=11.6  $\mu\text{m}$ ), in the entire volume of the phantom. By sectioning the model in several slices in the xy plane along the z axys, it is possible to acquire the displacement maps that can be compared with those of an experimental MRE.

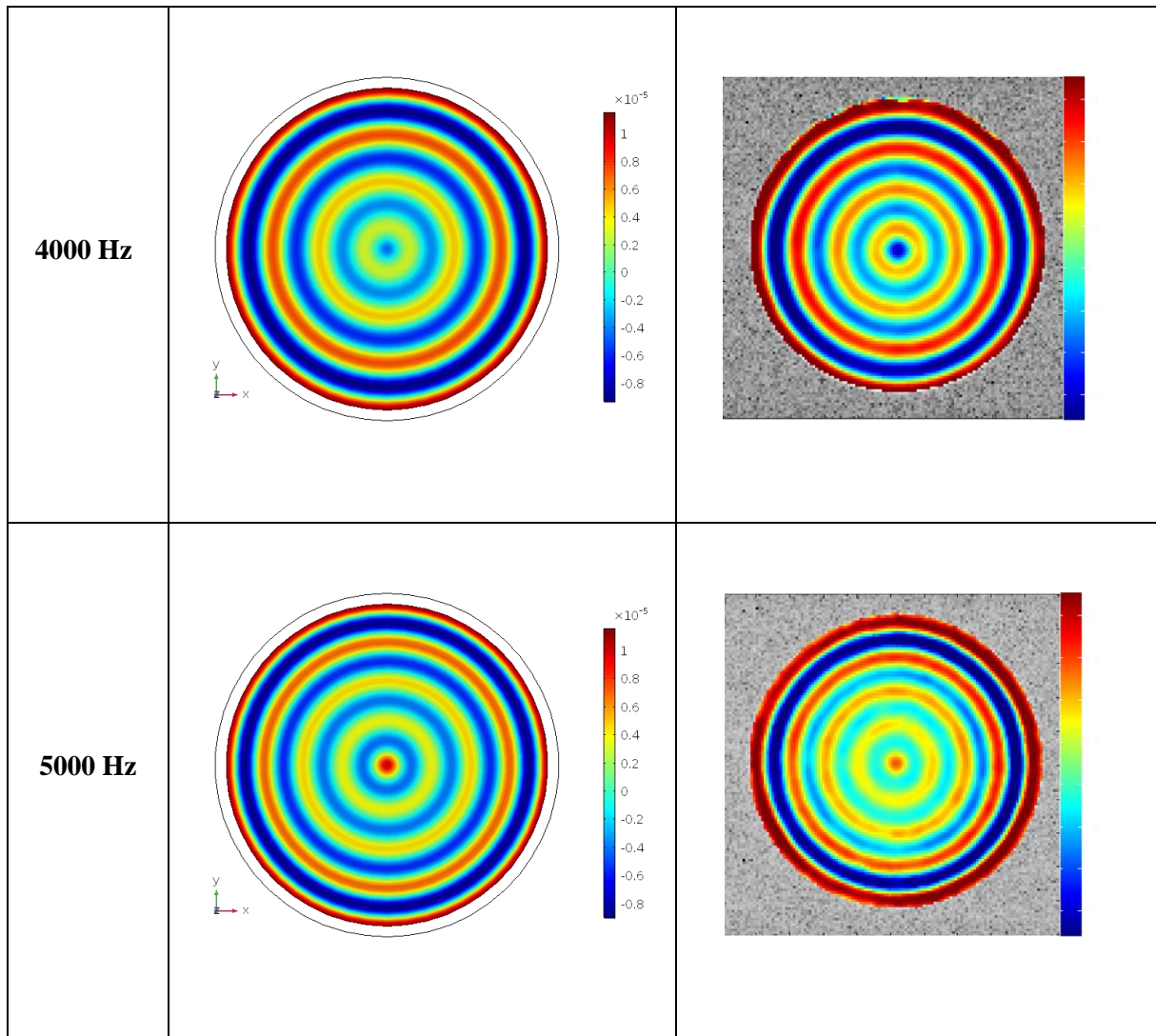
The mesh of the model could adequately capture the wave shape up to 5000 Hz, since the resolution is enough to properly represents the wave's crests and valleys.

A sweep of frequency from 1000 to 5000 Hz in step of 1000 Hz was run in Comsol obtaining the wave images shown on the left of the TABLE IV (displacement values are expressed in mm). They are comparable with the wave images previously obtained from MRE experiment shown on the right.



TABLE IV: COMPARISON BETWEEN COMPUTATIONAL (ON THE LEFT) AND EXPERIMENTAL (ON THE RIGHT) WAVE IMAGES FOR HOMOGENEOUS AND ISOTROPIC GELATIN.

Frequency	Computational wave images	Experimental wave images
1000 Hz		
2000 Hz		
3000 Hz		



Comsol wave images in output match quite well with the experimental ones excluding the boundary value of 1000 Hz and, since Comsol wave images are produced setting the material properties with values obtained from experimental postprocessing, this comparison also validates the MRE experimental postprocessing.

Comparing the displacement profiles from experiment with the computational ones it is possible to visualize the same behavior as a function of frequency between computational and experimental results. In Figure 28 the computational profiles are represented only for half of the diameter since the model implemented was axisymmetric, differently from the experimental profiles in Figure 24 plotted along the entire diameter.

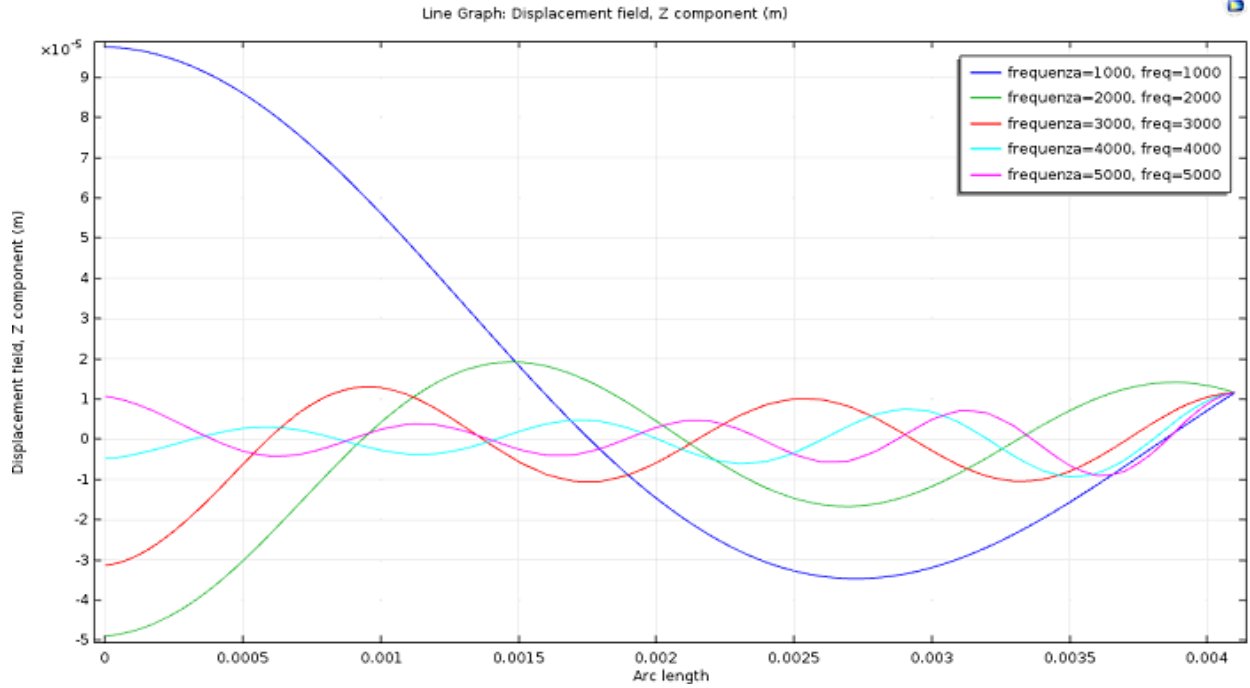


Figure 28: Computational displacement profiles for homogeneous and isotropic gelatin in direction perpendicular to the slice plane along the radius of the test tube.

## 7.2 Homogeneous and isotropic PVA

The same procedure was followed for the homogeneous and isotropic PVA phantom described in point 2 of section 6.2 obtaining the wave images reported in TABLE V.

Differently from gelatin, PVA wave images are more rough and noisy probably due to the presence of bubbles or heterogeneities of the material.

In Figure 29 the shapes of the displacement curves in the direction perpendicular to the slice plane and relative to the different wave images for each frequency are reported. Values are normalized with respect to the maximum.

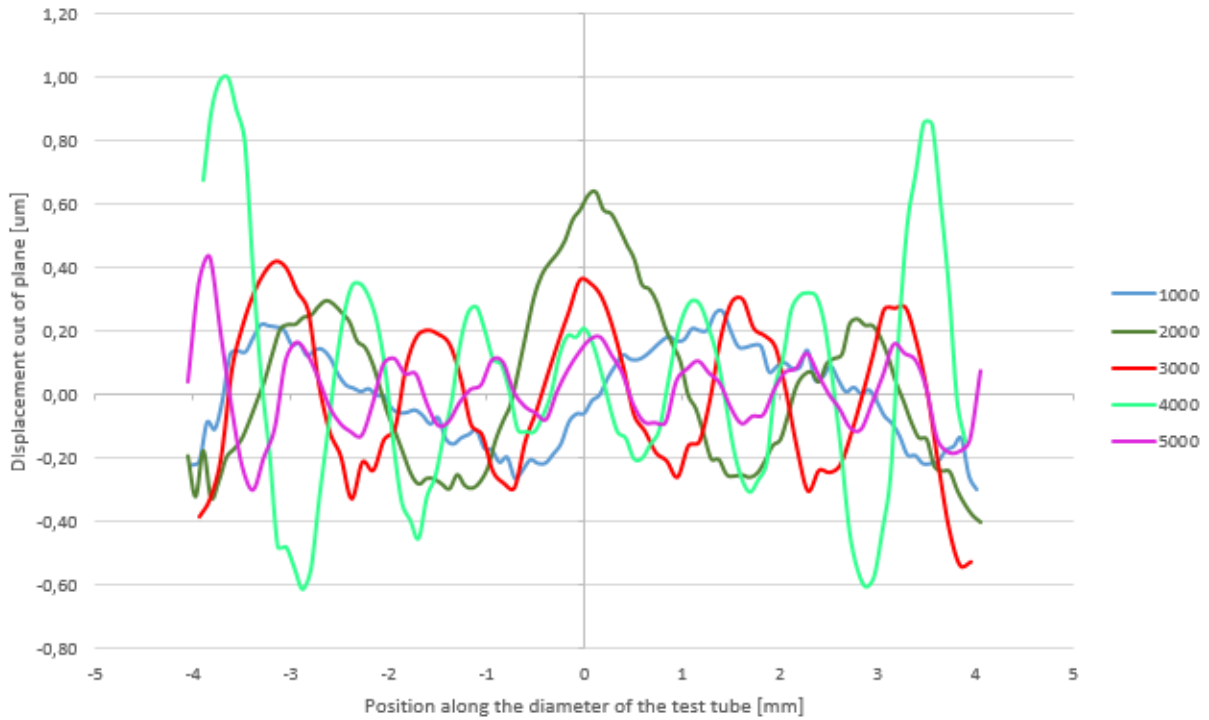


Figure 29: Experimental displacement profiles for homogeneous and isotropic PVA in direction perpendicular to the slice plane along the diameter of the test tube.

Even in this case the wave profiles are postprocessed as described in section 6.2 in order to obtain the values of  $\mu_R$  and  $\mu_I$  at each frequency as shown in Figure 30.

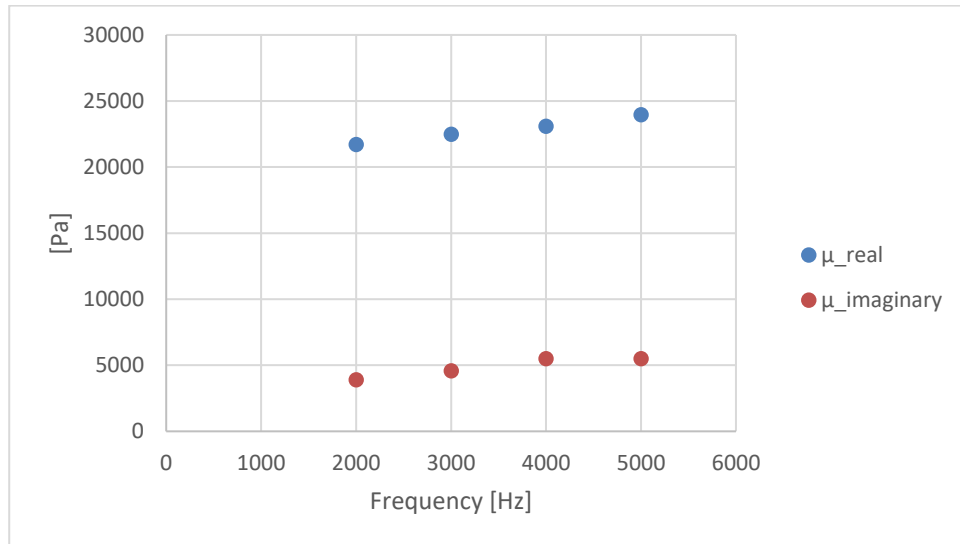


Figure 30:  $\mu_R$  and  $\mu_I$  curves in function of frequency for homogeneous and isotropic PVA.

The curves of  $\mu_R$  and  $\mu_I$  were separately fitted with a parabolic polynomial function to get the equation of each curve in function of frequency taking into consideration the standard deviation for each data point.

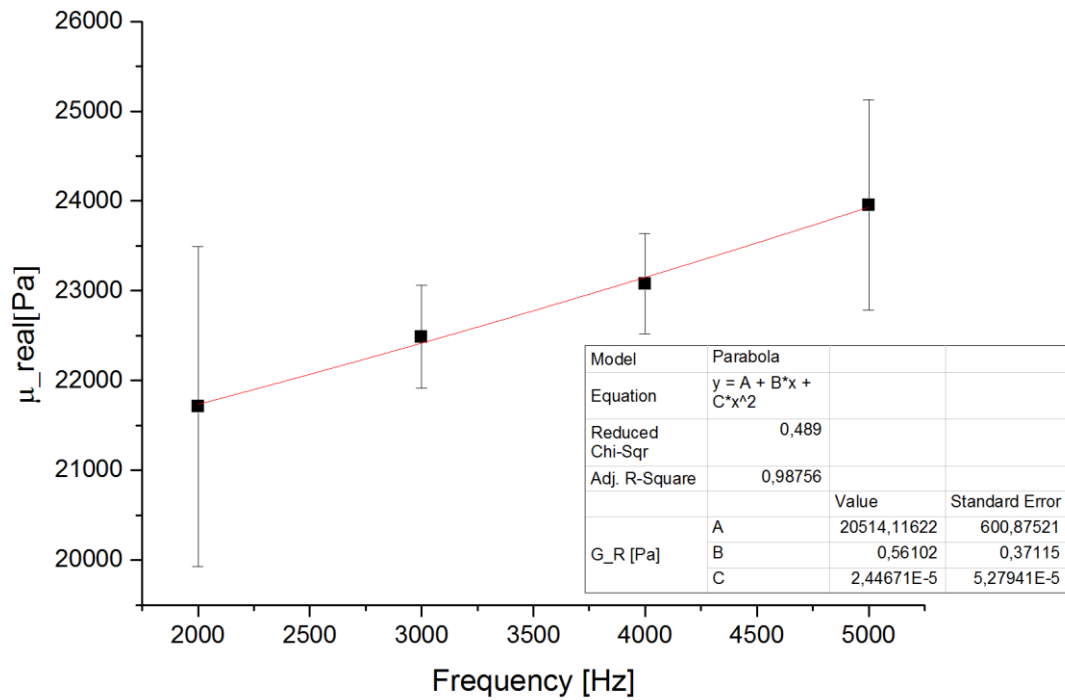


Figure 31: Curve fitting of the experimental data of  $\mu_R$  for homogeneous and isotropic PVA with a parabolic curve.

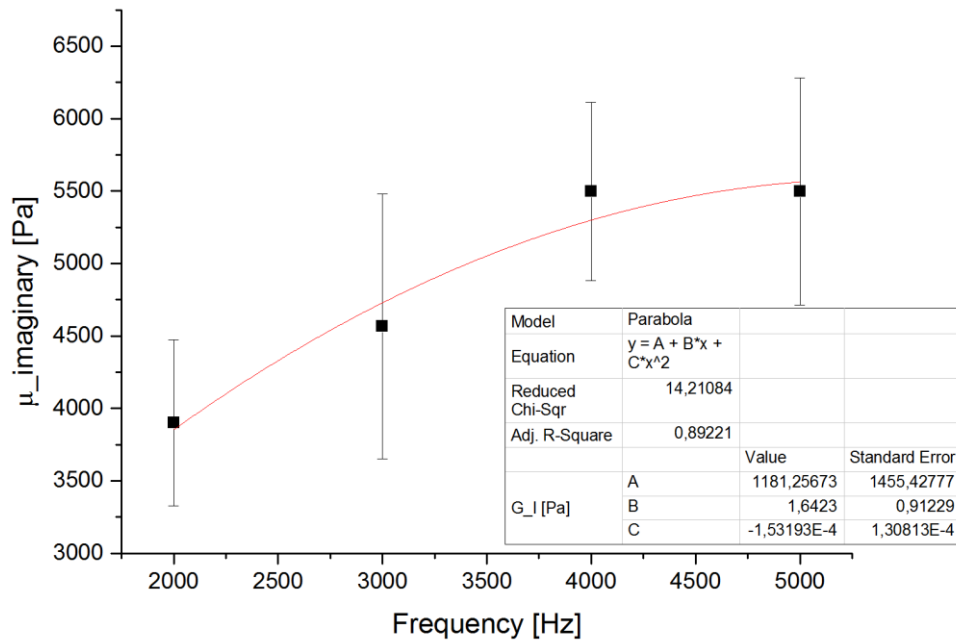


Figure 32: Curve fitting of the experimental data of  $\mu_I$  for homogeneous and isotropic PVA with a parabolic curve.

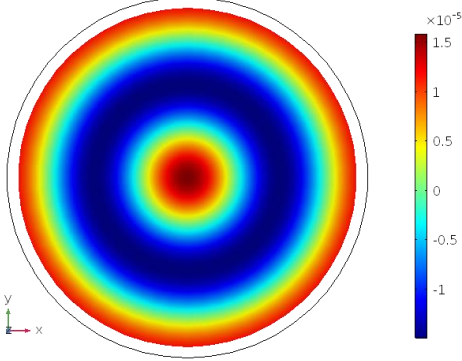
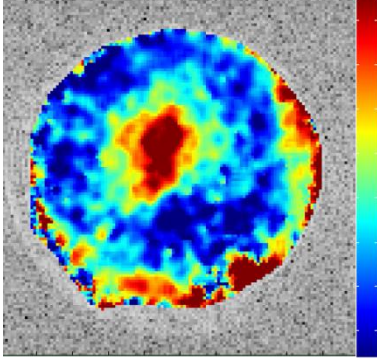
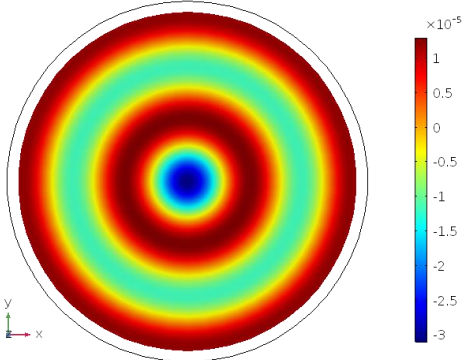
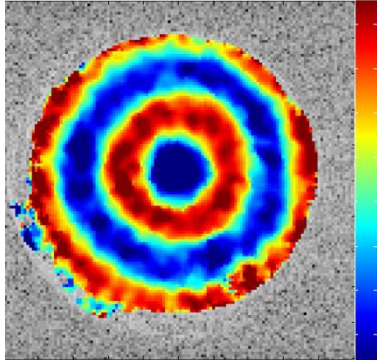
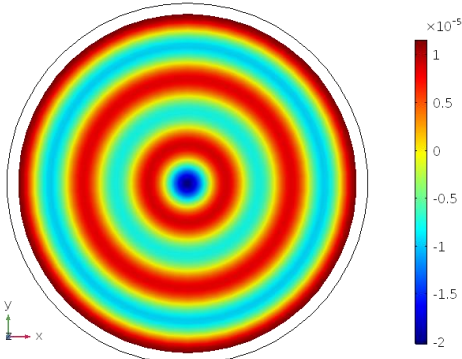
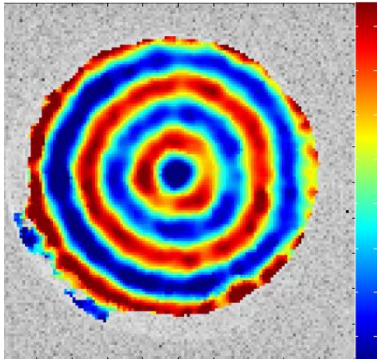
In order to set the direct problem in Comsol to compare the wave images obtained from experiment with the computational ones, the resultant parabolic curves describing the behavior of  $\mu_R$  and  $\mu_I$  in function of frequency were used as input for the material properties of the model implemented in Comsol.

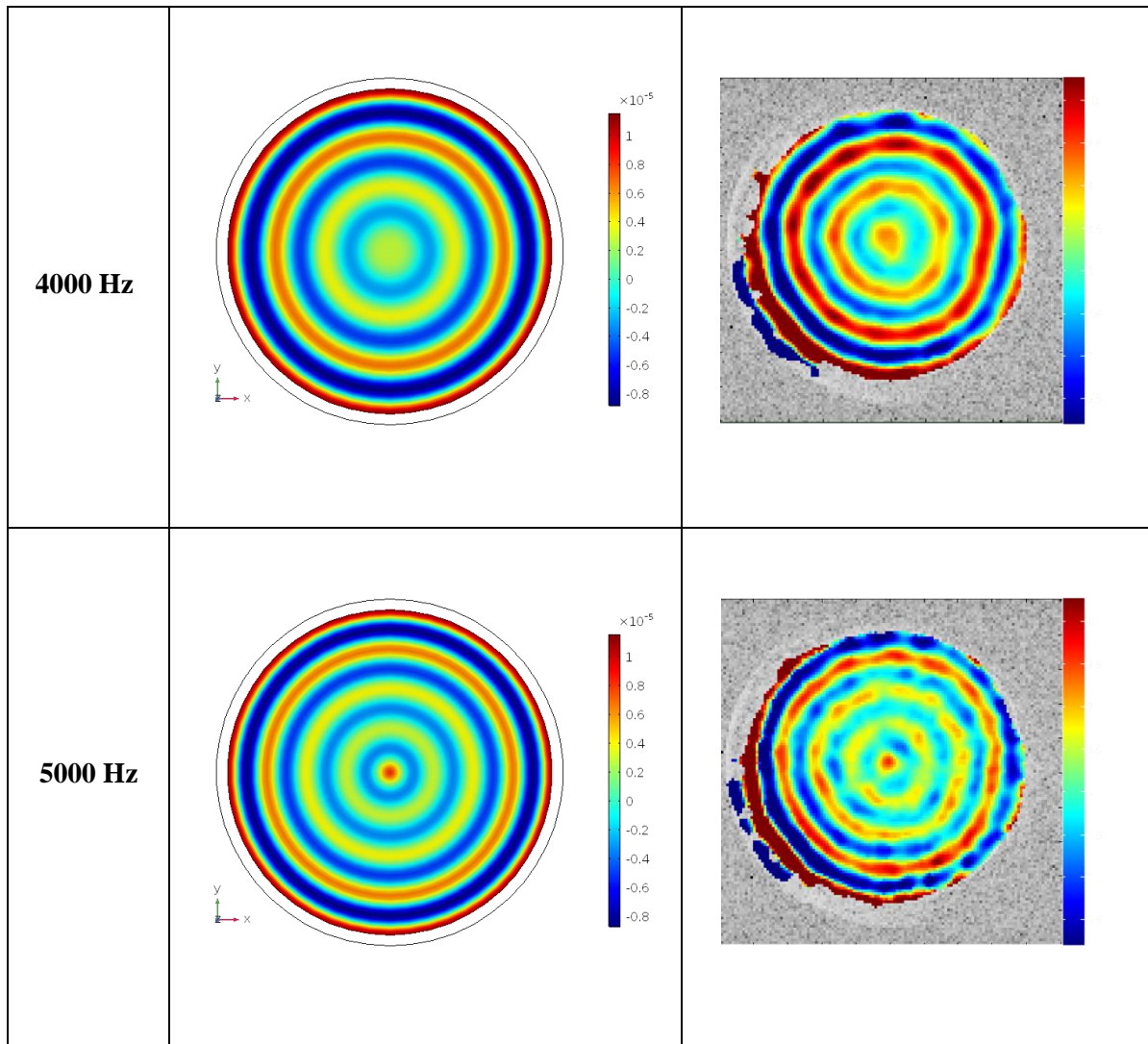
Also for PVA the displacement field in the entire volume of the phantom was obtained, inducing a harmonic displacement on the boundary (amplitude=11.6  $\mu\text{m}$ ) replicating the MRE experiment. By sectioning the model in several slices in the xy plane along the z axys, it is possible to acquire the displacement maps that can be compared with those of an experimental MRE.

The same mesh of the previous gelatin sample was built and a sweep of frequency from 1000 to 5000 Hz in step of 1000 Hz was run in Comsol obtaining the wave images shown on the left of TABLE V. They are comparable with the wave images previously obtained from MRE experiment shown on the right.



TABLE V: COMPARISON BETWEEN COMPUTATIONAL (ON THE LEFT) AND EXPERIMENTAL (ON THE RIGHT) WAVE IMAGES FOR HOMOGENEOUS AND ISOTROPIC GELATIN.

Frequency	Computational wave images	Experimental wave images
1000 Hz		
2000 Hz		
3000 Hz		



Also for PVA there is a good match between computation and experimental wave images apart the boundary value of 1000 Hz.

The match is visible from the displacement profiles. In Figure 33 are represented the computational profiles only for half of the diameter since the model implemented was axisymmetric.



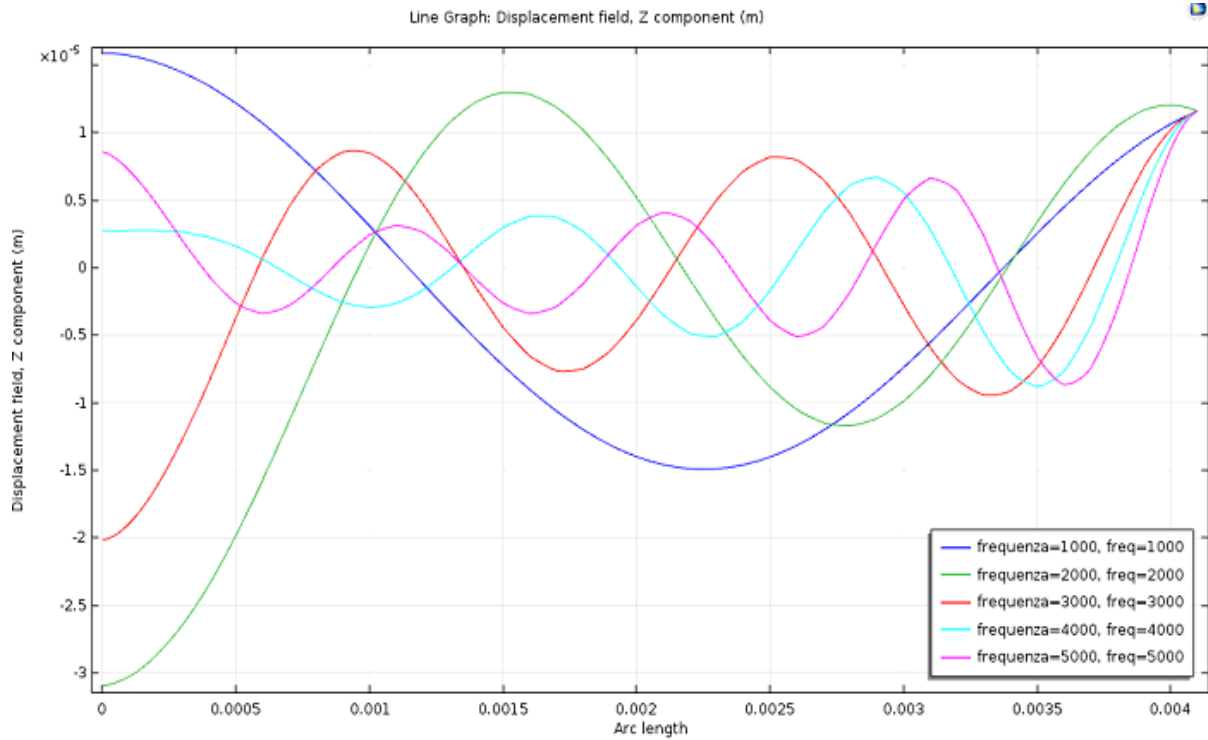


Figure 33: Computational displacement profiles for homogeneous and isotropic PVA in direction perpendicular to the slice plane along the radius of the test tube.

### 7.3 Spandex fibers

In order to be able to simulate in Comsol the anisotropic phantom, constituted by both gelatin and PVA but also from Spandex fibers, a static tension- extension experiment was performed assuming a linear elastic behavior of the polymer at least in the first range of the stress-strain curve.

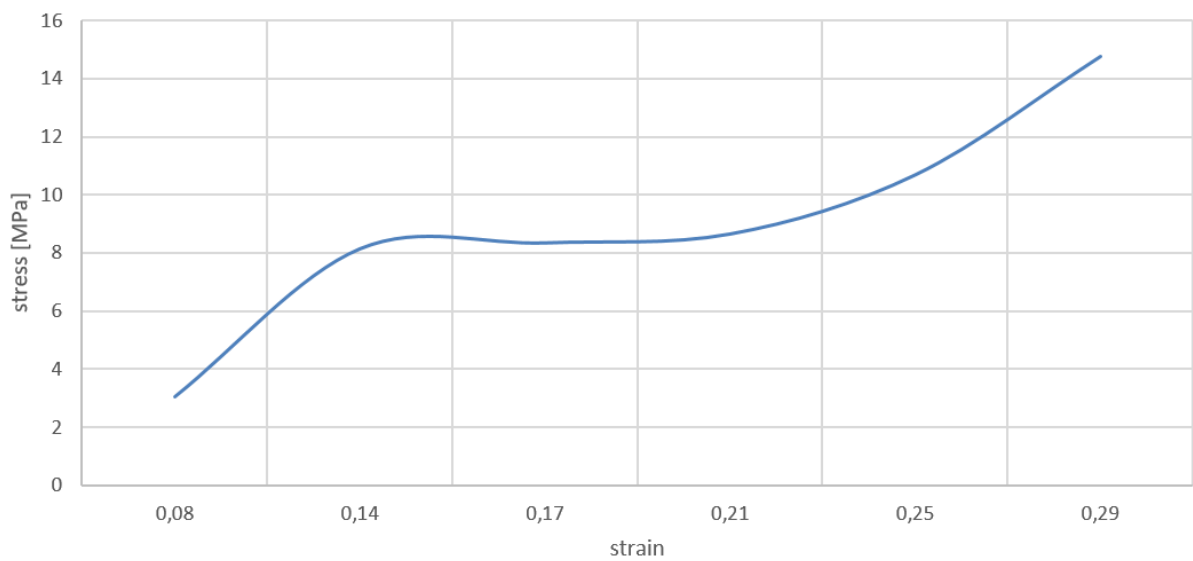


Figure 34: Stress-strain plot for Spandex fibers.

The calculated value of Young modulus  $E=77$  MPa is consistent with the values found in literature[50].

The density for the Spandex fibers used for the simulation is  $1300 \text{ Kg/m}^3$ , while for PVA and gelatin is supposed to be equal to water density of  $1000 \text{ Kg/m}^3$ .

#### **7.4 Transverse isotropic phantom with 4 fibers**

The previous material properties found for homogeneous gelatin, homogeneous PVA and spandex fibers were used as input in Comsol simulation to set the direct problem of elastography.

A sweep of frequency from 1000 to 5000 Hz in step of 1000 Hz was run in Comsol obtaining the wave images shown on the left of TABLE VI (units are in mm). On the right instead the resulting wave images from MRE experiment on the anisotropic phantom are reported.

MRI image slice in Figure 35 shows fibers position, used as a guide for TABLE VI.

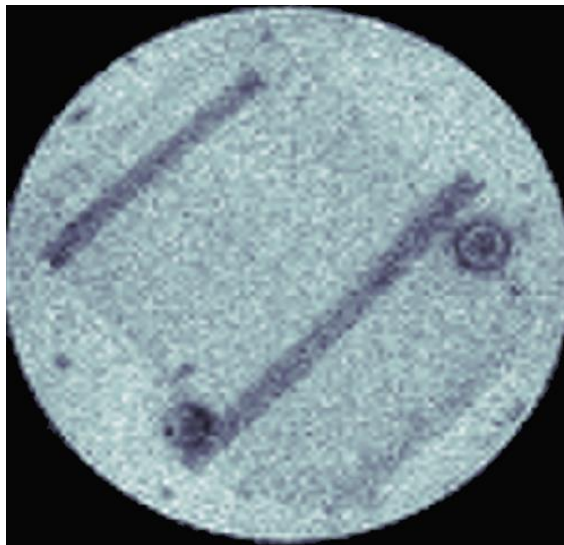
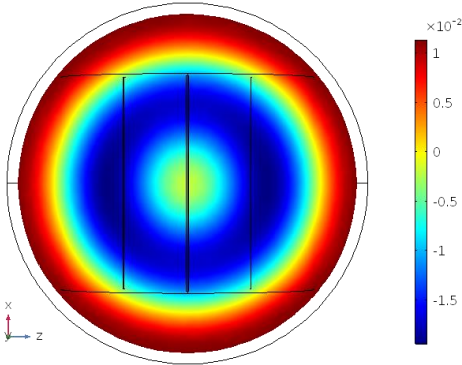
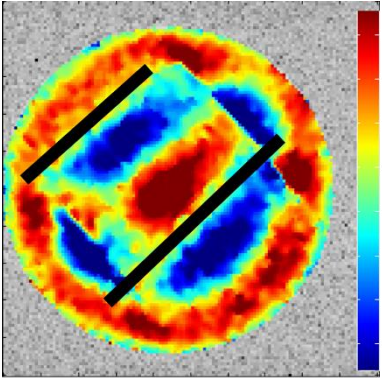
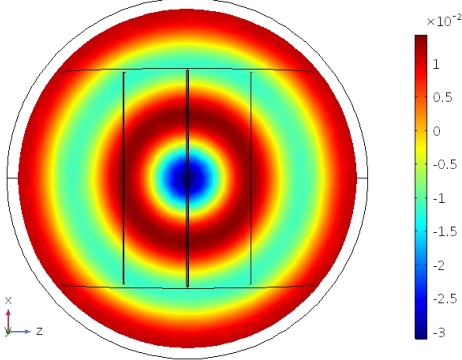
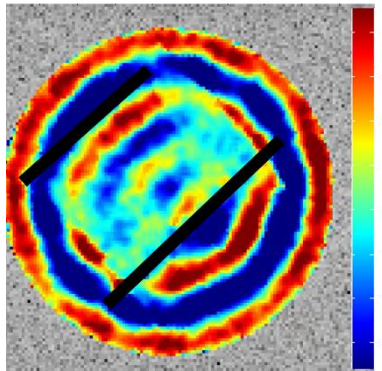
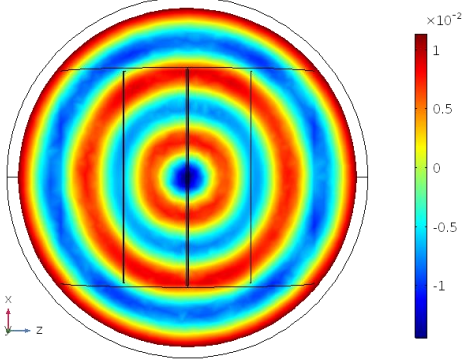
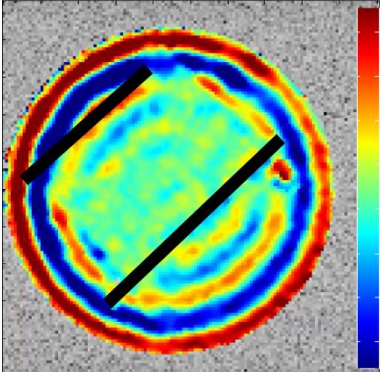
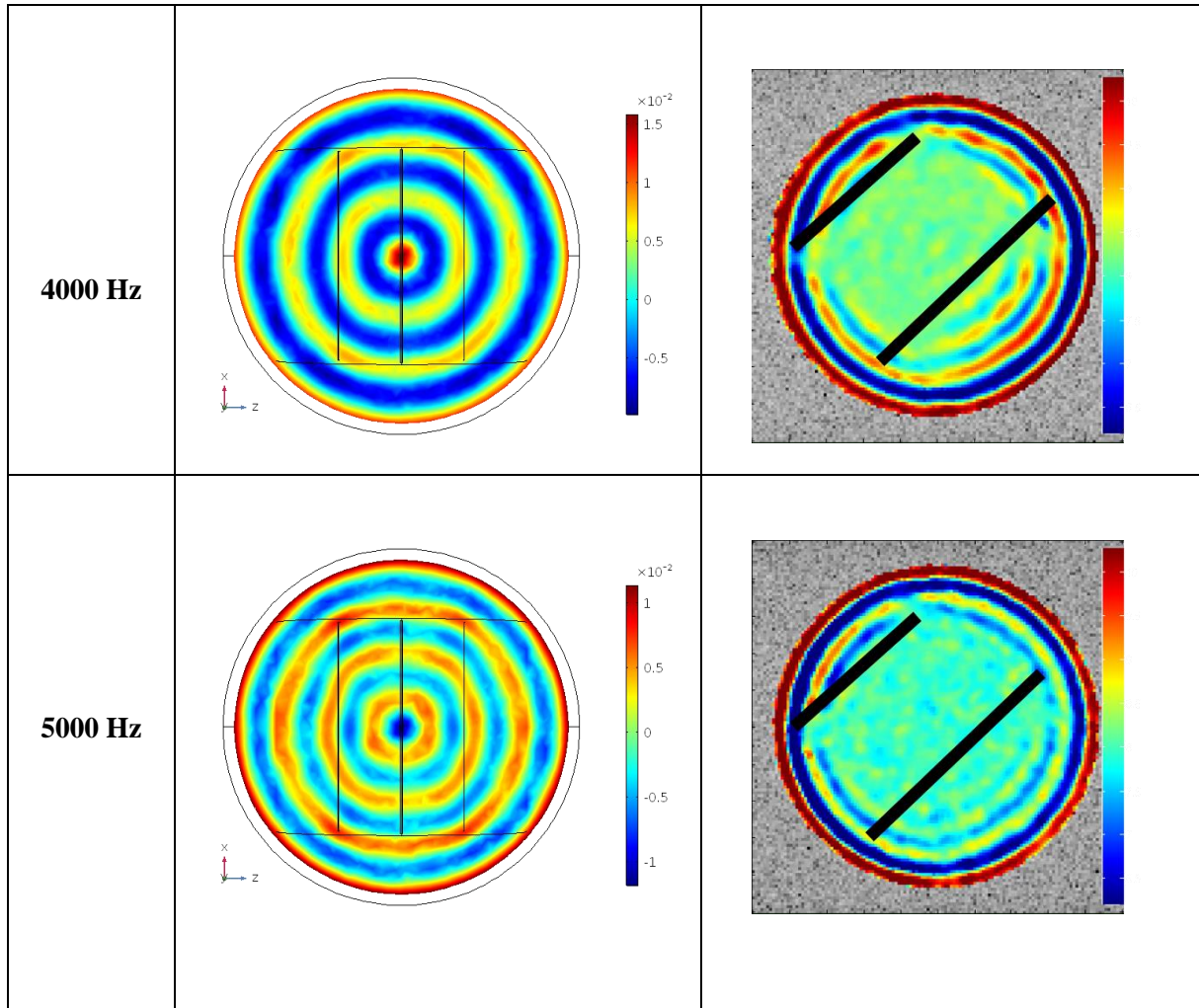


Figure 35: MRI slice of anisotropic phantom with 4 fibers taken in order to see the position of the fibers.

TABLE VI: COMPARISON BETWEEN COMPUTATIONAL (ON THE LEFT) AND EXPERIMENTAL (ON THE RIGHT) WAVE IMAGES FOR ANISOTROPIC PHANTOM WITH 4 FIBERS.

Frequency	Computational wave images	Experimental wave images
1000 Hz		
2000 Hz		
3000 Hz		



At low frequency of excitation the anisotropy, in terms of elongation of the wavefronts in the direction of the fibers, is not pronounced while, both for computational and experimental wave images, as expected discontinuity in correspondence of the fibers can be noticed. These discontinuities happen at the interfaces where stiffness mismatch occurs. In fact internal PVA is a little bit stiffer than the external gelatin. Also fibers are denser and stiffer with respect to gelatin. This shows how an MRE experiment can successfully be used to detect non-homogeneities in a phantom or tissue.

Wavefronts are no more clear at frequencies over 3000 Hz in the experimental wave images.

Moreover in the displacement fields a slight elongation of the wavefronts is visible assuming the characteristic “V-shape” [51] due to the material’s anisotropy: the waves will propagate faster along the directions where the material is stiffer, hence the elongated shape.

This kind of pattern can be detected through MRE experiments in skeletal muscle as well [38], and as such can be taken as a signal that the phantom meets some of the requirements of mimicking skeletal muscle's response under harmonic excitation.

At low frequencies, the wave exhibits only one crest, and it is not possible to witness enough the phenomenon of wave focusing [49], that can generally be detected in phantoms for elastography. To obtain multiple wave crests a possibility is to increase the excitation frequency, indeed at higher frequencies, from 3000 Hz, the wave focusing phenomenon is more relevant.

In Figure 36 are reported the displacement profiles in the out of plane direction with respect to the slice plane extracted from the computational wave images.

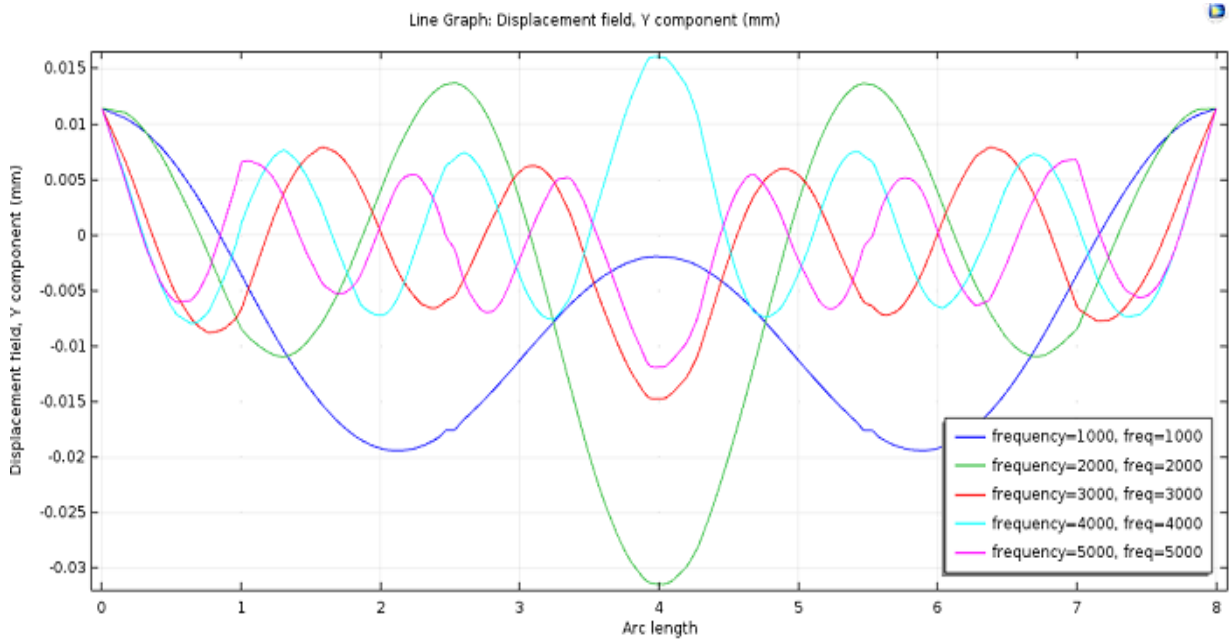


Figure 36: Computational displacement profiles in direction perpendicular to the slice plane along the diameter of the test tube for anisotropic phantom with 4 fibers (direction parallel to fibers).

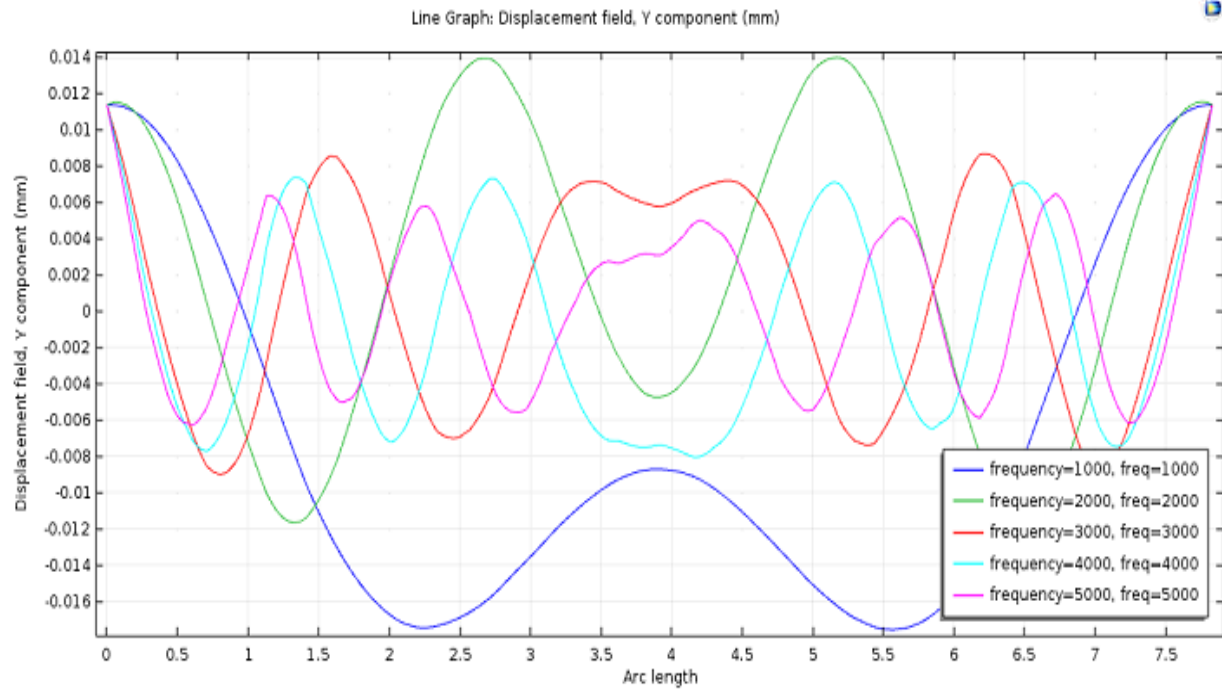


Figure 37: Computational displacement profiles in direction perpendicular to the slice plane along the diameter of the test tube for anisotropic phantom with 4 fibers (direction perpendicular to fibers).

Discontinuities in presence of the fibers can be noticed also from the wave profiles plots.

## 7.5 Transverse isotropic phantom with higher number of fibers

The geometry of the simulated model with more fibers is reported in Figure 38.



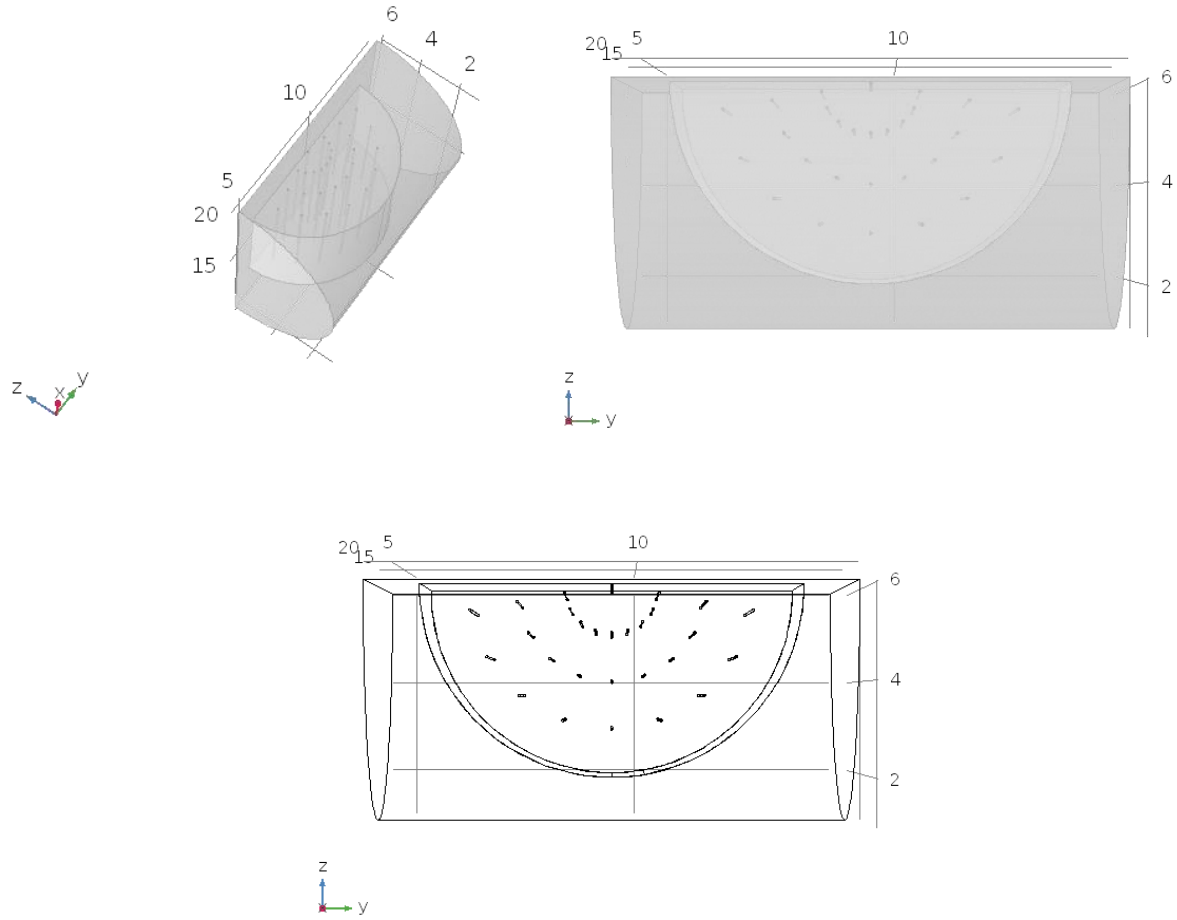


Figure 38: 3D model of the anisotropic phantom with an intermediate number of fibers.

In order to speed up the computational time only half geometry was simulated exploiting the symmetry of the model (Figure 39). This way the mesh was constituted by 1107985 tetrahedral elements and 68037 triangular elements.

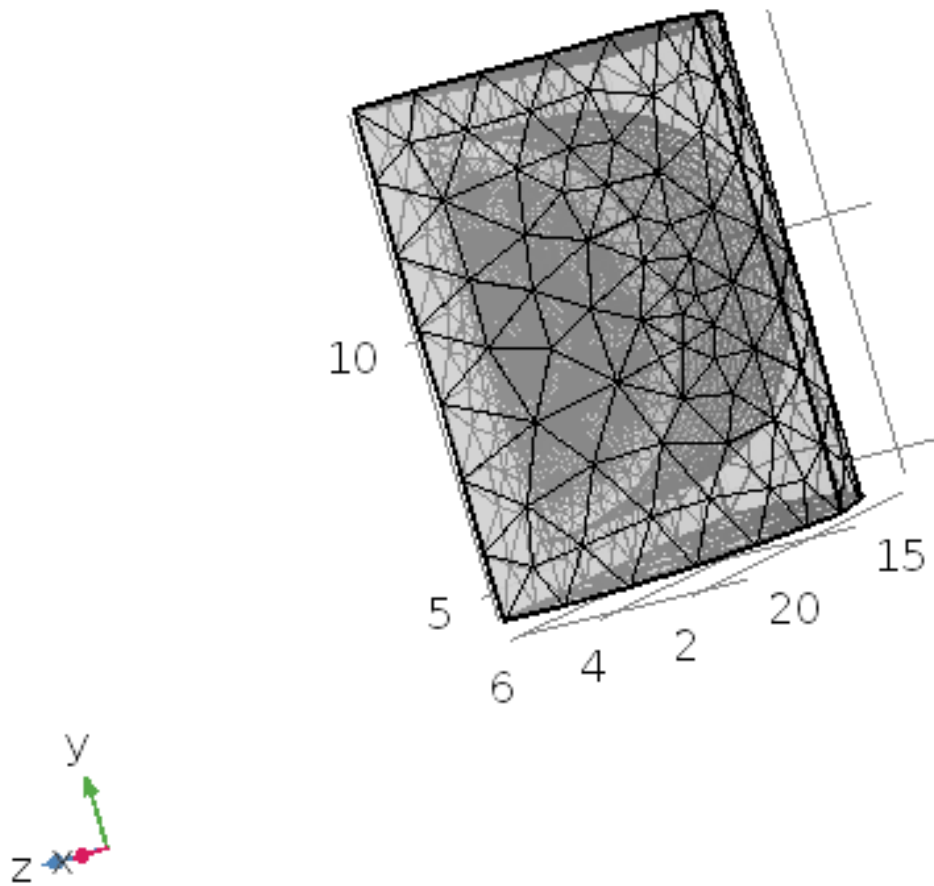
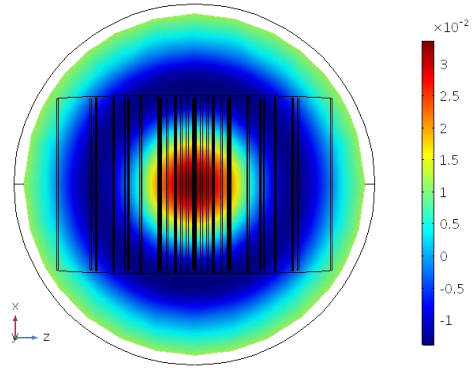
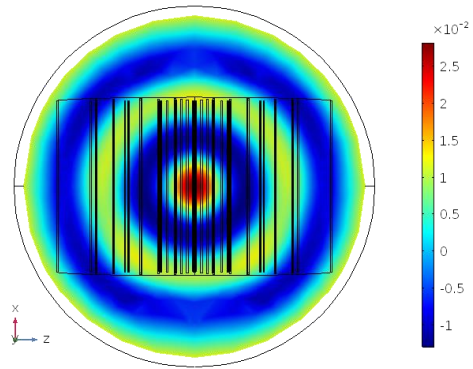
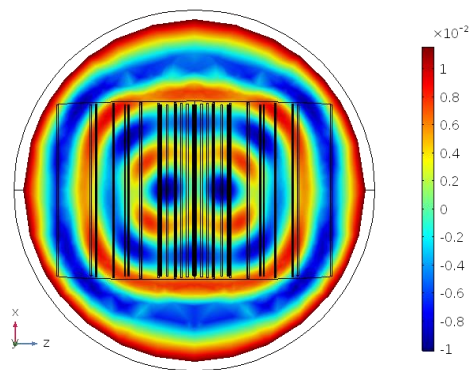


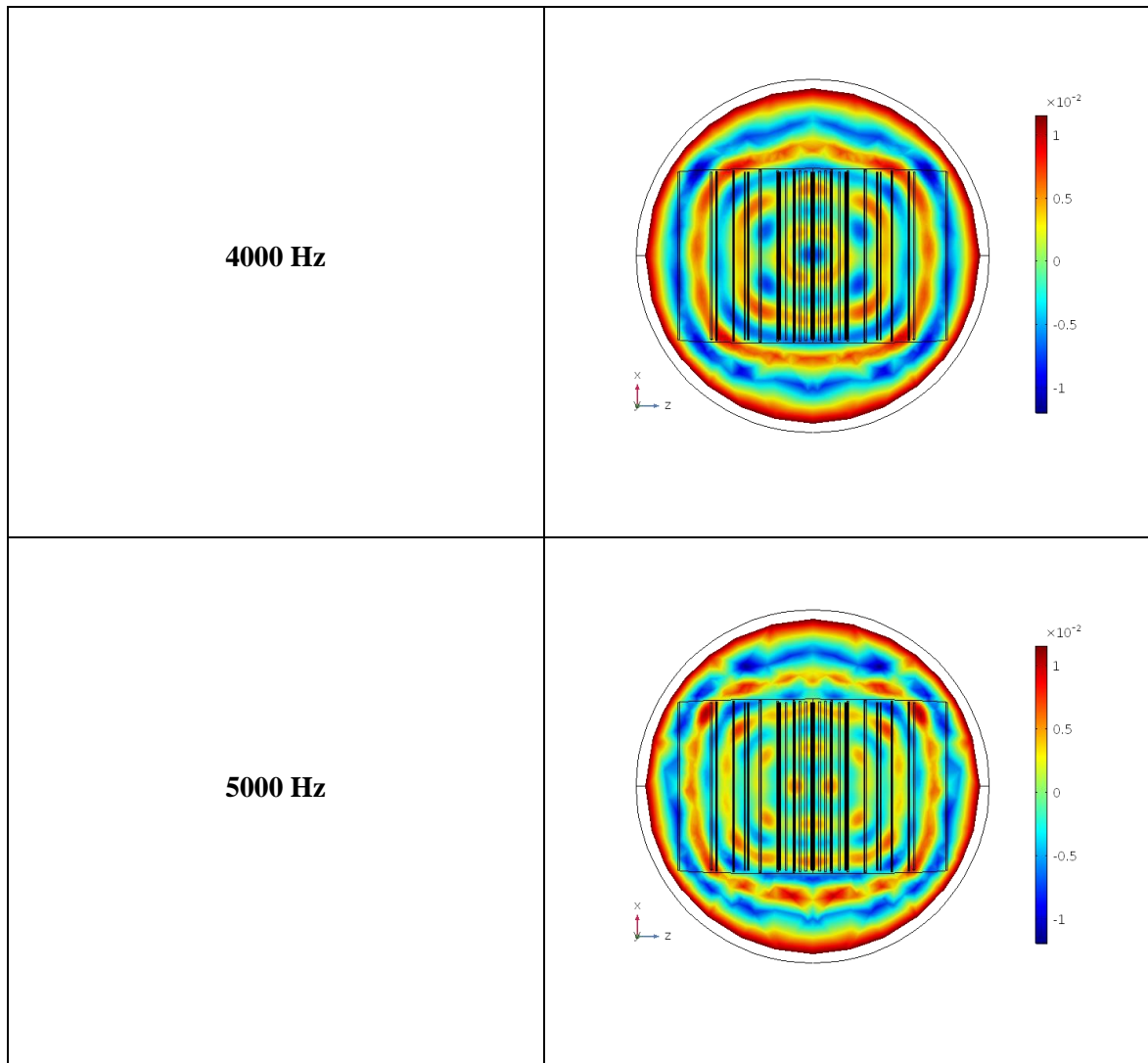
Figure 39: Mesh of the 3D model for the anisotropic phantom with an intermediate number of fibers.

A sweep of frequency from 1000 to 5000 Hz in step of 1000 Hz was run in Comsol obtaining the wave images shown in TABLE VII.



TABLE VII: COMPUTATIONAL WAVE IMAGES FOR ANISOTROPIC PHANTOM WITH INTERMEDIATE NUMBER OF FIBERS.

	Wave images
1000 Hz	 <p>Wave image at 1000 Hz. The image shows a circular cross-section with a central rectangular region. The color scale ranges from -1 to 3 (multiplied by <math>10^{-2}</math>). The image shows a central bright spot with concentric rings and a rectangular region of high intensity.</p>
2000 Hz	 <p>Wave image at 2000 Hz. The image shows a circular cross-section with a central rectangular region. The color scale ranges from -1 to 2.5 (multiplied by <math>10^{-2}</math>). The image shows a central bright spot with concentric rings and a rectangular region of high intensity.</p>
3000 Hz	 <p>Wave image at 3000 Hz. The image shows a circular cross-section with a central rectangular region. The color scale ranges from -1 to 1 (multiplied by <math>10^{-2}</math>). The image shows a central bright spot with concentric rings and a rectangular region of high intensity.</p>



At low frequency the anisotropy is not visible while from 3000 Hz discontinuities in presence of the fibers can be discerned.

Differently from what could be expected in the case of a transverse isotropic material, an elongation of the wavefronts is evident in the direction perpendicular to fibers. Moreover, instead of an elliptical shape of the wavefronts, they are more squared shaped. This can be due to the material properties of PVA and gelatin or to the fact that a vertical symmetry has been used in the model to speed up the simulation time.

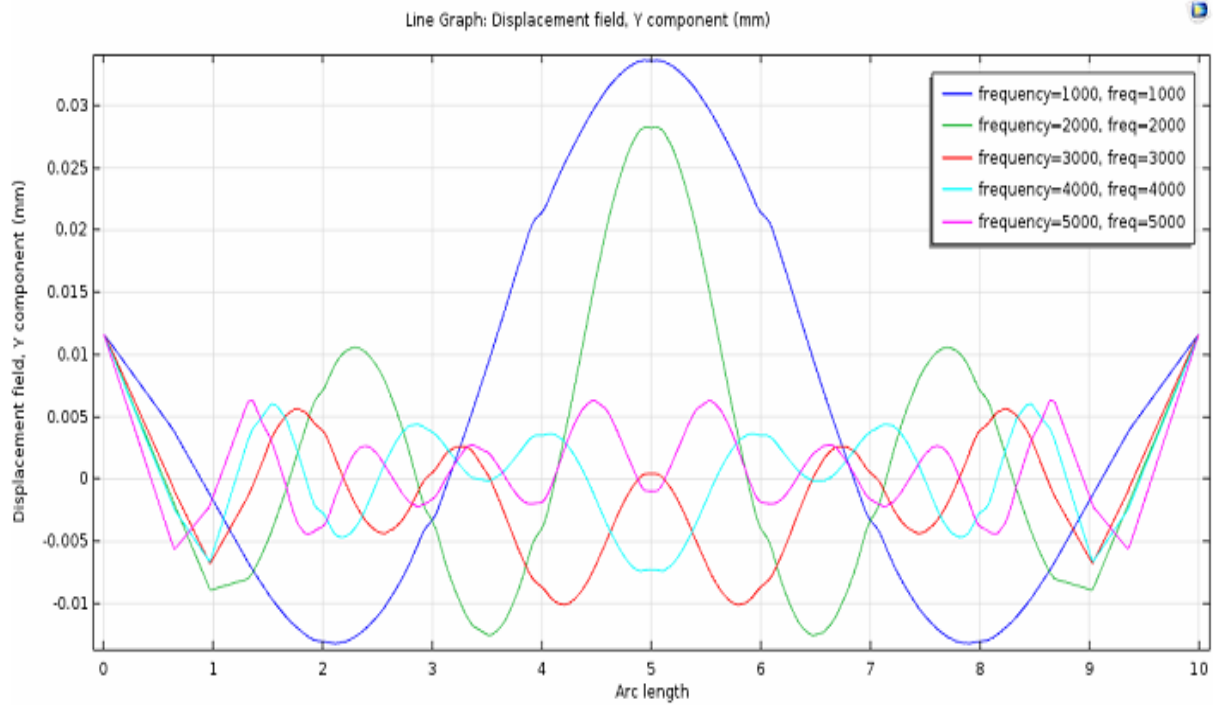


Figure 40: Computational displacement profiles in direction perpendicular to the slice plane along the diameter of the test tube for anisotropic phantom with intermediate number of fibers (direction perpendicular to fibers).

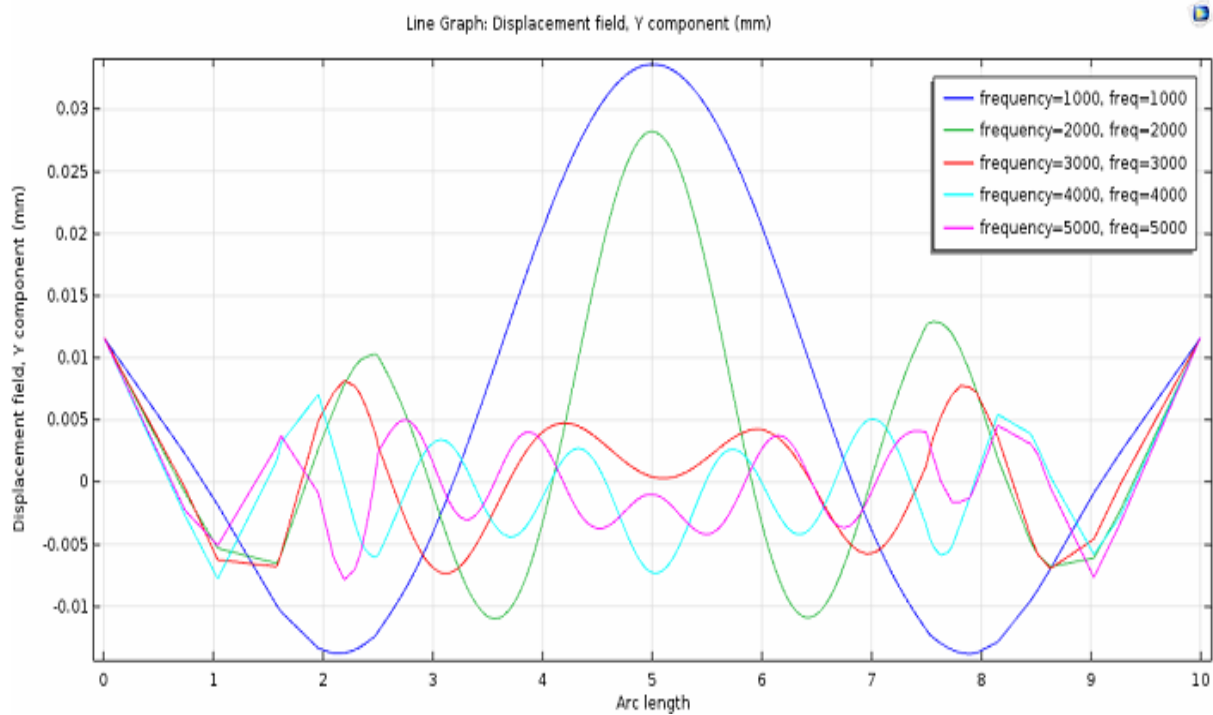


Figure 41: Computational displacement profiles in direction perpendicular to the slice plane along the diameter of the test tube for anisotropic phantom with intermediate number of fibers (direction parallel to fibers).

## 7.6 Transverse isotropic phantom with high number of fibers

The geometry of the simulated model with more fibers is reported in Figure 42.

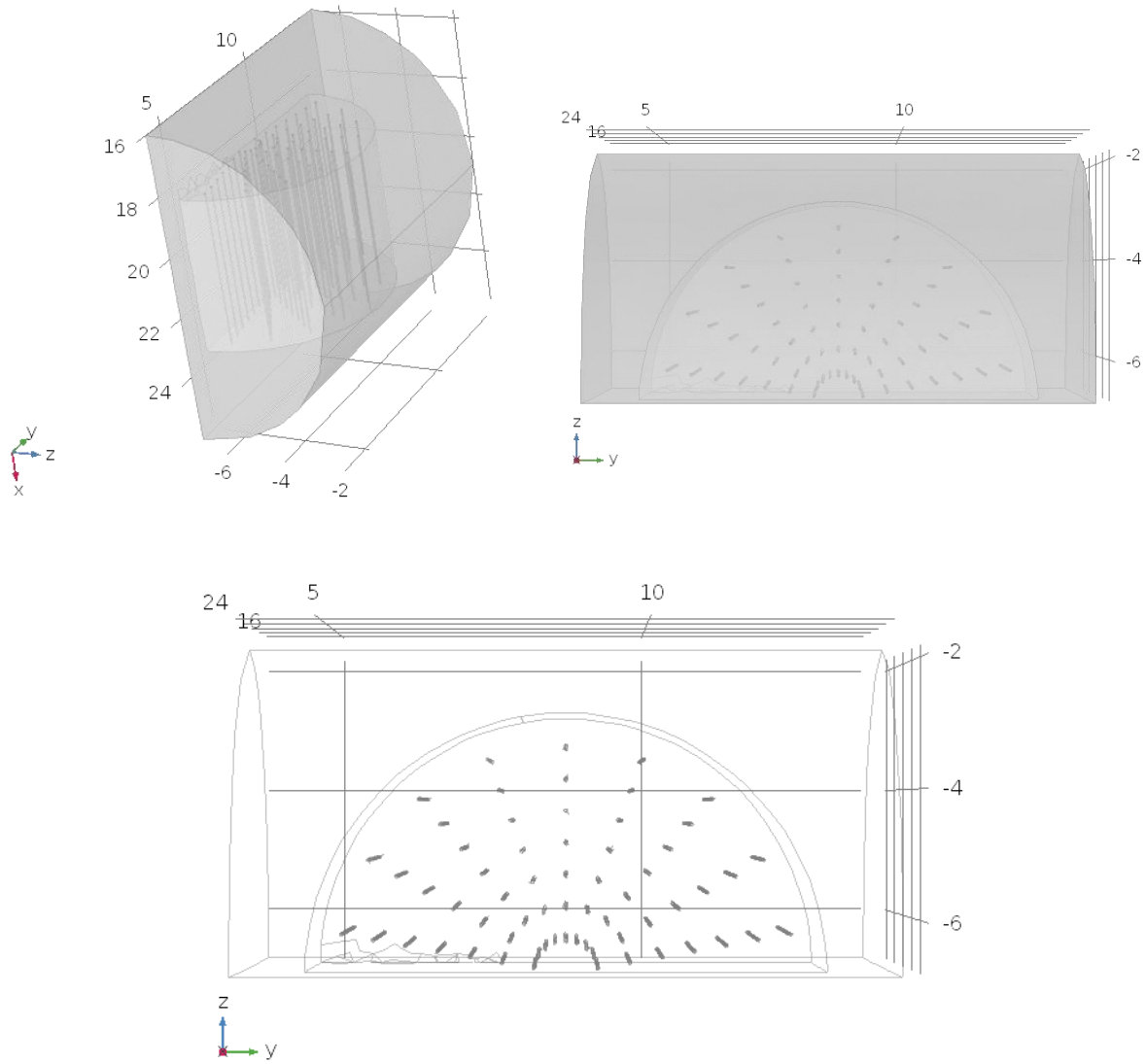


Figure 42: 3D model of the anisotropic phantom with high number of fibers.

In order to speed up the computational time only half geometry was simulated exploiting the symmetry of the model (Figure 43). This way the mesh was constituted by 1153007 tetrahedral elements and 162461 triangular elements.

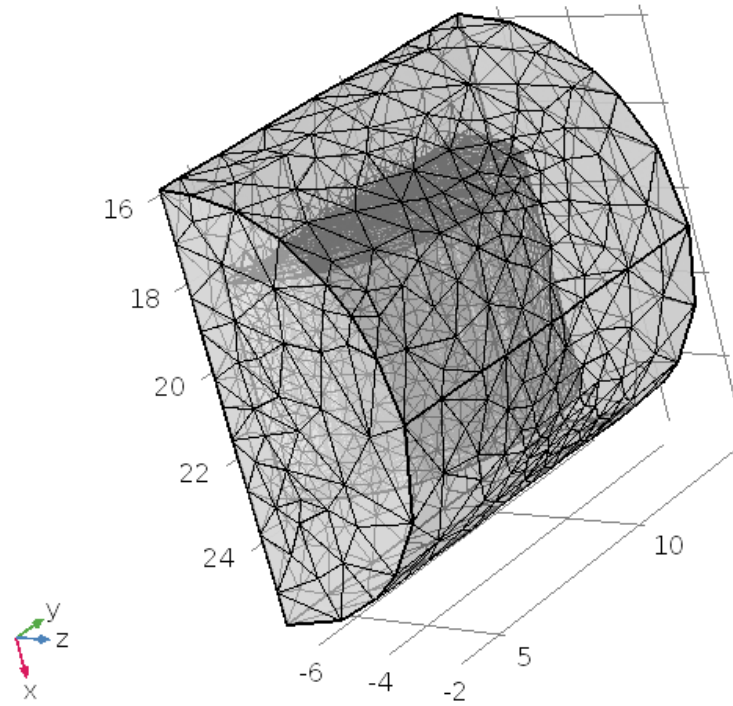
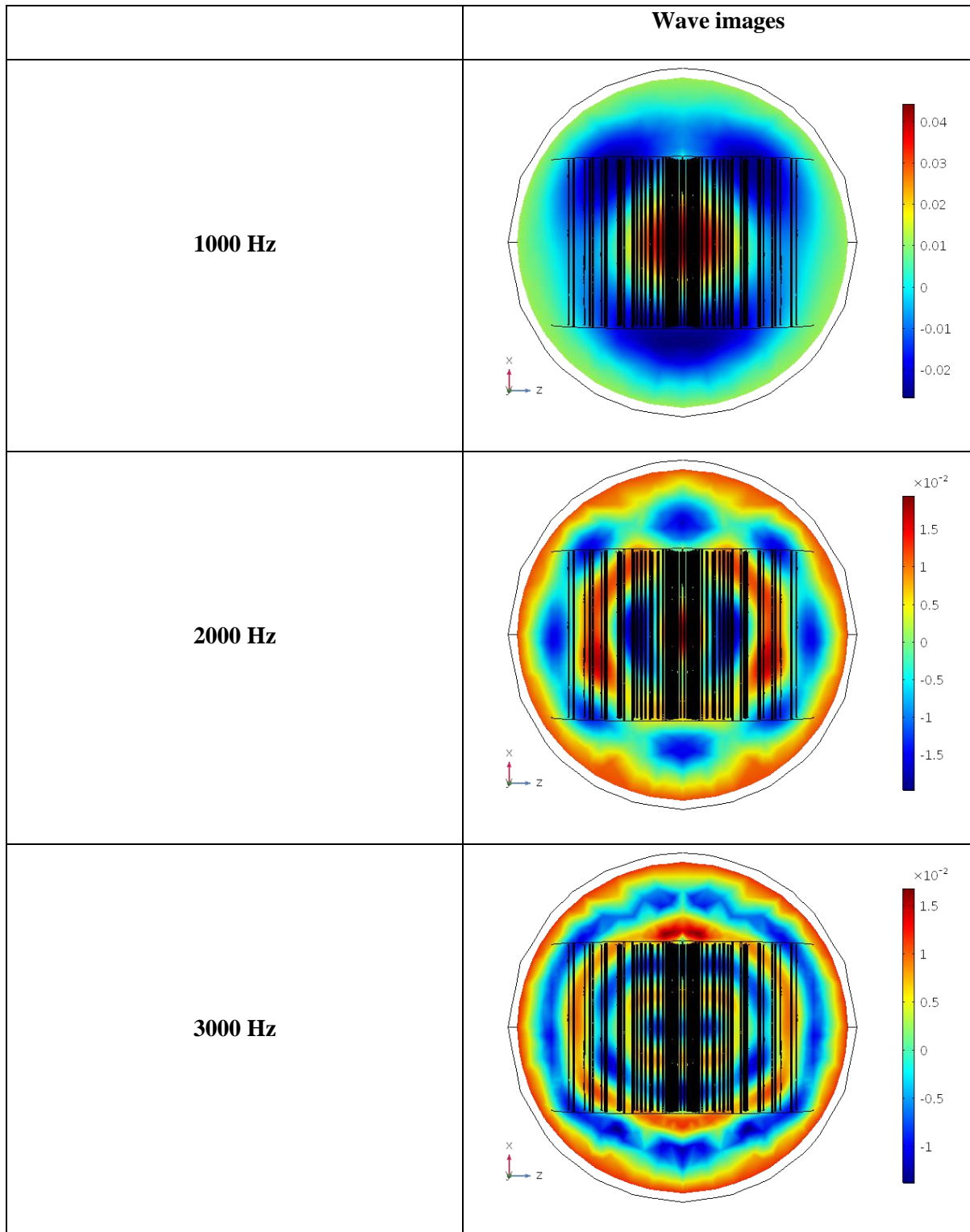
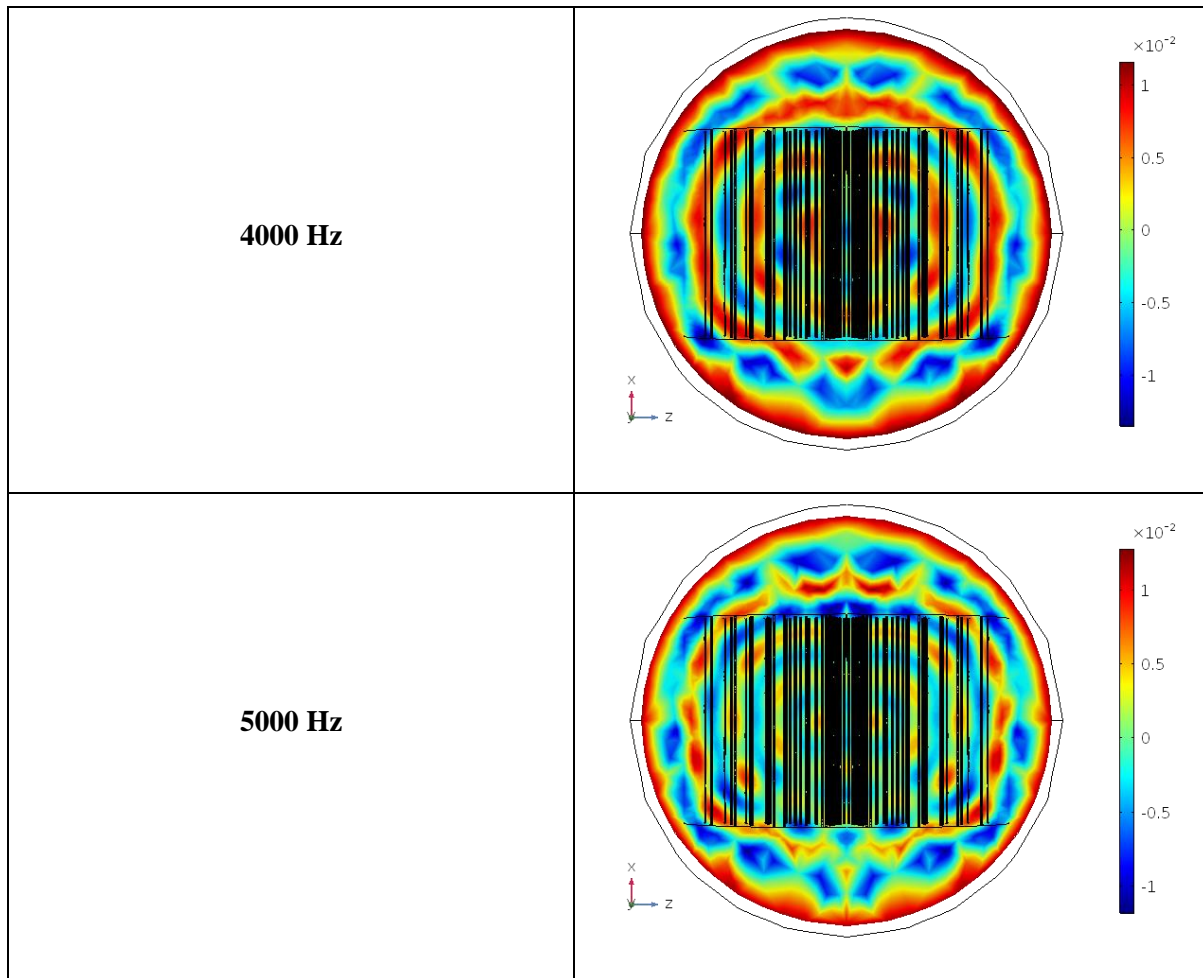


Figure 43: Mesh of the 3D model for the anisotropic phantom with high number of fibers.

A sweep of frequency from 1000 to 5000 Hz in step of 1000 Hz was run in Comsol obtaining the wave images shown in TABLE VIII (units are in mm).

TABLE VIII: COMPUTATIONAL WAVE IMAGES FOR ANISOTROPIC PHANTOM WITH HIGH NUMBER OF FIBERS.





Even in this case at low frequency the anisotropy is not visible while from 3000 Hz discontinuities in presence of the fibers can be discerned.



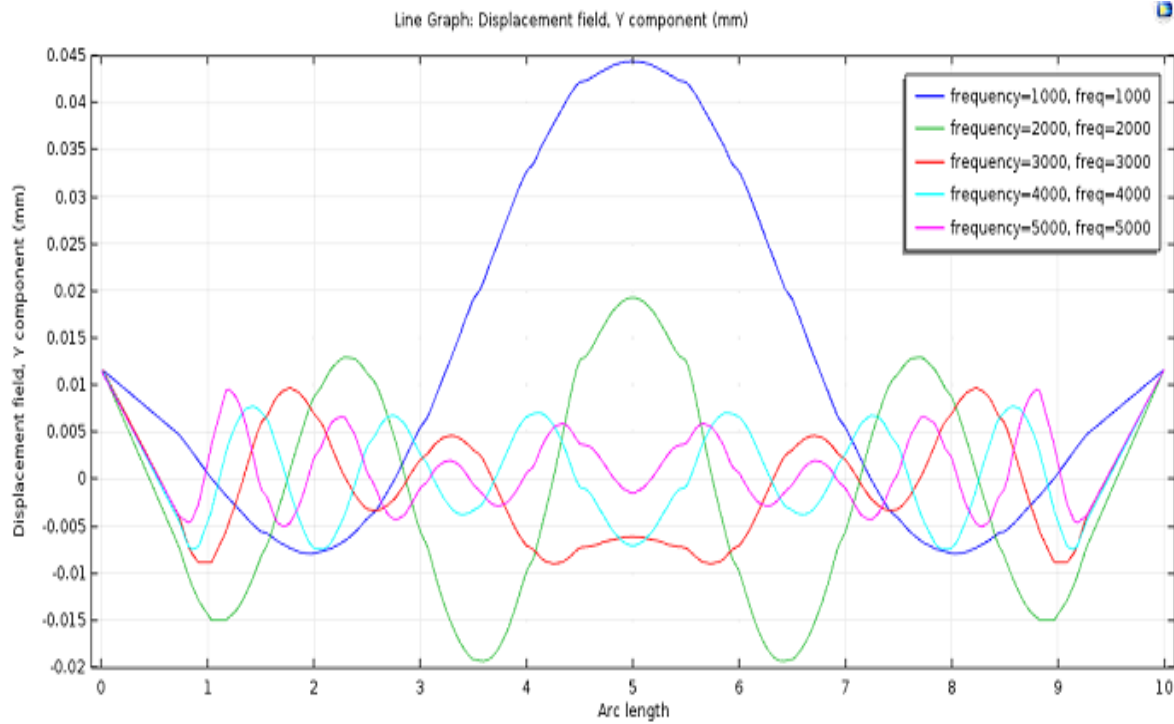


Figure 44: Computational displacement profiles in direction perpendicular to the slice plane along the diameter of the test tube for anisotropic phantom with high number of fibers (direction perpendicular to fibers).

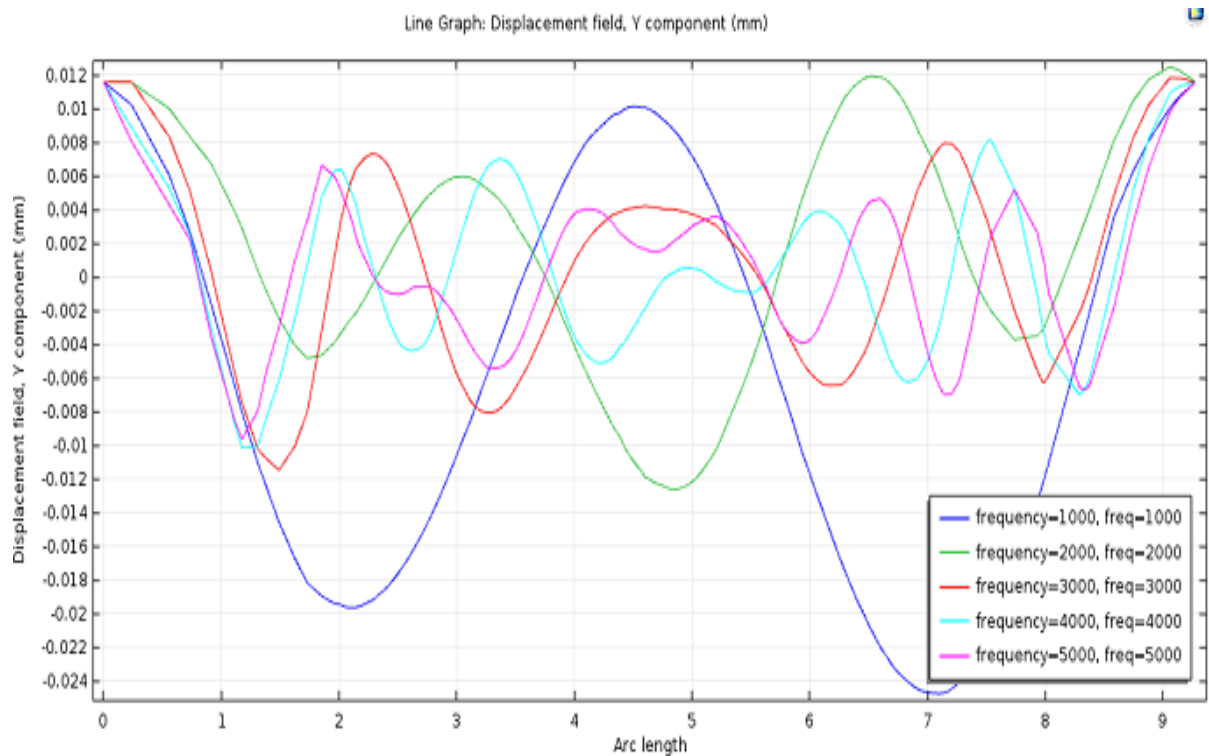


Figure 45: Computational displacement profiles in direction perpendicular to the slice plane along the diameter of the test tube for anisotropic phantom with high number of fibers (direction parallel to fibers).

The profiles are not completely symmetric due to asymmetries in the mesh.



As in the case of the phantom previously analyzed, an elongation of the wavefronts in the direction perpendicular to fibers and a squared shape of the wavefronts can be observed.

More simulations would be necessary to sort out the effect of anisotropy on the wavefronts propagation shape. In particular homogenized anisotropic models (representative of a densely populated fiber reinforced material having fibers distance much smaller than the wave-length) should be investigated.

Other simulations can be run changing the material properties, the geometry of the phantom or trying to simulate the entire phantom without the using of symmetries for the computation.

## CHAPTER 8

### CONCLUSION AND FUTURE DEVELOPMENTS

The assessment of muscular tissue stiffness finds relevant applications both in diagnostic and in more basic studies aiming at better understanding muscle's physiological and pathological behavior [7] [52] [9]. Magnetic Resonance Elastography exploits the conventional MRI technique to identify, by means of an inverse procedure, the shear stiffness of a tissue when mechanical wave propagation is detectable. As it is currently being extended to study anisotropic and viscoelastic properties of the tissues, it is nowadays subject of many research efforts [34] [4]. Different inverse methodologies are currently used to assess mechanical properties of tissues through the MRE technique; all of them are based on common assumption on materials' constitutive equations and rheological models. Numerous literature works on inverse problems of MRE are nowadays available with increasingly complex material models releasing simplifying assumptions on isotropy and linear elasticity [19] [38] [39] [40]. A deeper understanding of the direct problem, on how anisotropy and viscoelasticity affect the wave propagation, could greatly benefit the research on the optimization of the inversion algorithms.

In the present work, finite element simulations have been used to simulate the stationary propagation of waves in homogeneous and fiber reinforced material samples and comparison with MRE on laboratory samples subject to mechanical waves have been performed. The material parameters used in the numerical simulations were obtained through an identification process performed on experiments carried out on homogeneous material samples.

The anisotropic phantoms were supposed to mimic muscles mechanical properties, and as such they had a microstructure aimed to grant a transversely isotropic response, and were made with viscoelastic materials.

For future developments of this work new geometries for experimental phantoms can be realized through 3D printing. This technique would allow to obtain more accurate anisotropic material models with uniform and controlled anisotropic properties.

Would be interesting to find a way to postprocess the MRE experimental data in the case of anisotropic phantom since it is not possible to fit the displacement profiles with the closed form solution of the wave equation.

New inverse approaches may be considered. For example, the limitations introduced in the scalar Helmholtz inversion for viscoelastic anisotropic materials (in which an isotropic damping is used) may be more conveniently extended to anisotropic damping by introducing an additional unknown. In other words, the displacement fields obtained through the computational simulations, could be validated by performing an inversion algorithm on them and comparing the resulting elastograms with the known model's input material properties. Accounting for its anisotropy, for example it could be possible to perform a scalar Helmholtz inversion with the expression of the out of plane displacement, and thus to obtain respectively  $\mu_{\perp}$  and  $\mu_{\parallel}$ , as described in section 4.3.1 of the present work. It should be noted that the algorithm described in section 4.4, that is nothing but an extension of Helmholtz inversion for transversely isotropic, viscoelastic materials, could prove inaccurate in determining the actual material properties, as it assumes isotropic damping, to simplify the equations and obtain solution 4.36. This is done in the passage from equation 4.34 to equation 4.35, where what should be, in general, two unknowns (the imaginary parts of  $\mu_{\perp}$  and  $\mu_{\parallel}$ ), are collected into a single unknown (the imaginary part of  $\mu = i\omega\eta$ ). In other words, equation 4.36 should more exhaustively be written as equation 8.1:

$$-\rho\omega^2 q_i \cong \mu_{\perp} q_{i,jj} + \tau \left[ \frac{\partial^3 u_1}{\partial x_3^3} - \frac{\partial^3 u_3}{\partial x_1 \partial x_2^2} - \frac{\partial^3 u_3}{\partial x_1^3} \right] + \eta_{\perp} \frac{\partial}{\partial t} q_{i,jj} + \psi \frac{\partial}{\partial t} \left[ \frac{\partial^3 u_1}{\partial x_3^3} - \frac{\partial^3 u_3}{\partial x_1 \partial x_2^2} - \frac{\partial^3 u_3}{\partial x_1^3} \right] \quad (8.1)$$

$$u_{3,jj}$$

where  $\psi = \eta_{\parallel} - \eta_{\perp}$ .

FEM approach to modeling of the direct problems can also be the basis for new inverse approaches: it could be for example possible to proceed through the minimization of an error function defined as the difference between a displacement field calculated with FEM and the field obtained from the MRE experiment. Once the finite element approach has been perfected, it could prove instrumental in the validation of MRE technique for materials that exhibit frequency dependent behavior: indeed, the test commonly used to validate MRE, rheometry, is ineffective for this purpose. This is because rheometry

tests are undertaken at frequencies around 10 Hz [14], lower than the conventional range for elastography (10-1000 Hz), and comparison with rheometry is thus only viable if viscoelasticity is not accounted for.

## CITED LITERATURE

- [1] P. Bowker, *Physical properties of tissue*, vol. 13, no. 5. 1991.
- [2] Y. K. Mariappan, K. J. Glaser, and Richard L Ehman, “Magnetic Resonance Elastography: a Review,” *Clin. Anat.*, vol. 23, no. 5, pp. 497–511, 2010.
- [3] M. a Dresner, G. H. Rose, P. J. Rossman, R. Muthupillai, a Manduca, and R. L. Ehman, “Magnetic resonance elastography of skeletal muscle.,” *J. Magn. Reson. Imaging*, vol. 13, pp. 269–276, 2001.
- [4] I. Sack, K. Jöhrens, J. Würfel, and J. Braun, “Structure-sensitive elastography: on the viscoelastic powerlaw behavior of in vivo human tissue in health and disease Emerging Area Soft Matter Background: springpot and viscoelastic scaling,” *Soft Matter*, vol. 9, pp. 5672–5680, 2013.
- [5] J. P. Emmanuel, N., Callé, S., Remenieras, “Generating shear waves in the human brain for ultrasound elastography: a new approach,” *Phys. Procedia*, 2015.
- [6] R. L. Lieber, S. Steinman, I. A. Barash, and H. Chambers, “Structural and functional changes in spastic skeletal muscle,” *Muscle and Nerve*, vol. 29, no. 5, pp. 615–627, 2004.
- [7] M. a Alnaqeeb, N. S. Al Zaid, and G. Goldspink, “Connective tissue changes and physical properties of developing and ageing skeletal muscle.,” *J. Anat.*, vol. 139 ( Pt 4, pp. 677–689, 1984.
- [8] J. R. Basford, T. R. Jenkyn, K. N. An, R. L. Ehman, G. Heers, and K. R. Kaufman, “Evaluation of healthy and diseased muscle with magnetic resonance elastography,” *Arch. Phys. Med. Rehabil.*, vol. 83, no. 11, pp. 1530–1536, 2002.
- [9] V. Johns, R. J., Wright, “Relative importance of various tissues in joint stiffness,” *J. Appl. Physiol.*, 1962.
- [10] M. Shinohara, K. Sabra, J. L. Gennisson, M. Fink, and M. L. Tanter, “Real-time visualization of muscle stiffness distribution with ultrasound shear wave imaging during muscle contraction,” *Muscle and Nerve*, vol. 42, no. 3, pp. 438–441, 2010.

### CITED LITERATURE (continued)

- [11] A. Nordez, J. L. Gennisson, P. Casari, S. Catheline, and C. Cornu, "Characterization of muscle belly elastic properties during passive stretching using transient elastography," *J. Biomech.*, vol. 41, no. 10, pp. 2305–2311, 2008.
- [12] D. G. Chernak, L. A., DeWall, R. J., Lee, K. S., Thelen, "Length and activation dependent variations in muscle shear wave speed," *Physiol. Meas.*, vol. 100, no. 2, pp. 130–134, 2012.
- [13] M. K. Chakouch, F. Charleux, and S. F. Bensamoun, "Development of a phantom mimicking the functional and structural behaviors of the thigh muscles characterized with magnetic resonance elastography technique," *Proc. Annu. Int. Conf. IEEE Eng. Med. Biol. Soc. EMBS*, vol. 2015–Novem, pp. 6736–6739, 2015.
- [14] E. C. Qin *et al.*, "Combining MR elastography and diffusion tensor imaging for the assessment of anisotropic mechanical properties: A phantom study," *J. Magn. Reson. Imaging*, vol. 37, no. 1, pp. 217–226, 2013.
- [15] S. Papazoglou, J. Braun, U. Hamhaber, and I. Sack, "Two-dimensional waveform analysis in MR elastography of skeletal muscles.," *Phys. Med. Biol.*, vol. 50, no. 6, pp. 1313–1325, 2005.
- [16] J. Bercoff, M. Tanter, and M. Fink, "Supersonic Shear Imaging : A New Technique," *IEEE Trans. Ultrason. Ferroelectr. Freq. Control*, vol. 51, no. 4, pp. 396–409, 2004.
- [17] R. L. Kruse, Scott A., Rose, Gregory H., Glaser, Kevin J., Manduca, Armando, Felmlee, Joel P., Jack, Clifford R., Ehman, "Magnetic Resonance Elastography of the Brain," *Neuroimage*, vol. 11, no. 5, pp. 447–453, 2009.
- [18] P. Y. Xu, L., Lin, Y., Han, J. C., Xi, Z. N., Shen, H., Gao, "Magnetic resonance elastography of brain tumors: preliminary results," *Acta radiol.*, 2007.
- [19] T. K. Liu, Yifei, Yasar, T. J. Royston, and R. L. Magin, "Ultra Wideband (0.5 – 16 kHz) MR Elastography for Robust Shear Viscoelasticity Model Identification," *Magn. Reson. Med.*, vol. 70, no. 2, pp. 479–489, 2013.

### CITED LITERATURE (continued)

- [20] T. Wu, J. P. Felmlee, J. F. Greenleaf, S. J. Riederer, and R. L. Ehman, "MR imaging of shear waves generated by focused ultrasound.," *Magn. Reson. Med.*, vol. 43, no. 1, pp. 111–115, 2000.
- [21] R. L. Manduca, A., Muthupillai, R., Rossman, P. J., Greenleaf, J. F., Ehman, "LOCAL WAVELENGTH ESTIMATION FOR MAGNETIC RESONANCE ELASTOGRAPHY," *Curr. Med. Imaging Rev.*, pp. 4–9, 1996.
- [22] B. C. Goss, K. P. McGee, E. C. Ehman, a Manduca, and R. L. Ehman, "Magnetic resonance elastography of the lung: technical feasibility.," *Magn. Reson. Med.*, vol. 56, no. 5, pp. 1060–1066, 2006.
- [23] L. Sandrin *et al.*, "Transient elastography: a new noninvasive method for assessment of hepatic fibrosis.," *Ultrasound Med. Biol.*, vol. 29, no. 12, pp. 1705–1713, 2003.
- [24] J. Burlew, M. M, Madsen, E. L., Sum, S. W., Zagzebski, "A new ultrasound tissue-equivalent material," *Artic. Radiol.*, no. 134(2), pp. 517–520, 1980.
- [25] A. Goss, W. M., Matthews, H. E., Winnberg, "High-resolution Observations of the W33 Complex at 2.8, 6, 18 and 21 cm," *Astron. Astrophys.*, no. 65, pp. 307–312, 1978.
- [26] G. J. Tortora and M. T. Nielsen, *Principles of Human Anatomy*, vol. 53, no. 9. 2012.
- [27] J. D. Bronzino and D. J. Schnek, *Biomechanics principles and applications*. 2003.
- [28] L. E. Bilston and K. Tan, "Measurement of Passive Skeletal Muscle Mechanical Properties In Vivo: Recent Progress, Clinical Applications, and Remaining Challenges," *Ann. Biomed. Eng.*, vol. 43, no. 2, pp. 261–273, 2015.
- [29] K. F. Graff, *Wave Motion in Elastic Solids*. 1991.
- [30] A. Bedford and D. S. Drumheller, *Introduction to Elastic Wave Propagation*. 1996.
- [31] P. Fung, Y. C., Tong, *CLASSICAL AND COMPUTATIONAL SOLID MECHANICS*. 2001.
- [32] "Phase, Group and Signal velocity," *Mathpages.com*. .

### CITED LITERATURE (continued)

- [33] a. Manduca *et al.*, “Magnetic resonance elastography: Non-invasive mapping of tissue elasticity,” *Med. Image Anal.*, vol. 5, no. 4, pp. 237–254, 2001.
- [34] R. Sinkus *et al.*, “Imaging anisotropic and viscous properties of breast tissue by magnetic resonance-elastography,” *Magn. Reson. Med.*, vol. 53, no. 2, pp. 372–387, 2005.
- [35] R. Howard, A., Chris, *Elementary Linear Algebra*. 2005.
- [36] O. Donahue, H., Kaufman, “Transversely isotropic tensile material properties of skeletal muscle tissue,” *J. Biomech. Behav. Biomed. Mater.*, 2011.
- [37] S. L. Blemker, S.S., Delp, “Three-dimensional representation of complex muscle architectures and geometries,” *Ann. Biomed. Eng.*, 2005.
- [38] S. Papazoglou, J. Rump, J. Braun, and I. Sack, “Shear wave group velocity inversion in MR elastography of human skeletal muscle,” *Magn. Reson. Med.*, vol. 56, no. 3, pp. 489–497, 2006.
- [39] D. Klatt, S. Papazoglou, J. Braun, and I. Sack, “Viscoelasticity-based MR elastography of skeletal muscle,” *Phys. Med. Biol.*, vol. 55, no. 21, pp. 6445–6459, 2010.
- [40] J. M. Carcione, D. Kosloff, and R. Kosloff, “Wave propagation simulation in a linear viscoelastic medium,” *Geophys. J.*, vol. 95, no. 1988, pp. 597–611, 1988.
- [41] B. A. Krieger, R. E., Auld, *Acoustic fields and waves in soldis*. 1990.
- [42] E. Royer, D., Dieulesaint, *Elastic Waves in Solid I Free and Guided Propagation*. 2000.
- [43] D. Roylance, *Engineering viscoelasticity*. 2001.
- [44] R. Meral, F.C., Royston, T.J, Magin, “Fractional calculus in viscoelasticity: An experimental study,” *Commun. nonlinear Sci. Numer. Simul.*, 2009.
- [45] K. Y. C. Holten-Andersen, N., Jaishankar, A., Harrington, M.J., Fullenkamp, D.E., DiMarco, G.He, L, McKinley, G.H., Messersmith, P.B., Lee, “Metal-coordination: Using one of natures tricks to control soft material mechanics,” *J. Mater. Chem.*, 2013.



### CITED LITERATURE (continued)

- [46] O. Posnansky, J. Guo, S. Hirsch, S. Papazoglou, U. Braun, and I. Sack, “Fractal network dimension and viscoelastic powerlaw behavior: I. A modeling approach based on a coarse-graining procedure combined with shear oscillatory rheometry,” *Phys. Med. Biol. Phys. Med. Biol.*, vol. 57, no. 57, pp. 4023–4040, 2012.
- [47] F. Mainardi, *Fractional calculus and waves in linear viscoelasticity*. 2010.
- [48] M. R. L. Klatt D., Yasar T.K., Royston T.J., “Sample interval modulation for the simultaneous acquisition of displacement vector data in magnetic resonance elastography: theory and application,” vol. 58, no. 24, pp. 8663–8675, 2014.
- [49] R. L. Yasar, Temel K., Royston, Thomas J., Magin, “Wideband MR elastography for viscoelasticity model identification,” vol. 100, no. 2, pp. 130–134, 2012.
- [50] C. Dongsheng, L. I. U. Hong, Z. Qiaoling, and W. Hongge, “Effects of Mechanical Properties of Fabrics on Clothing Pressure,” no. 1, pp. 232–235, 2013.
- [51] J. Sack, I., Bernarding, J. and Braun, “Analysis of wave patterns in MR elastography of skeletal muscle using coupled harmonic oscillator simulations,” *Magn. Reson. Imaging*, 2002.
- [52] P. J. Bressel E., McNair, “The effect of prolonged static and cyclic stretching on ankle joint stiffness, torque relaxation, and gait in people with stroke,” *Phys. Ther.*, 2002.

## **VITA**

**NAME:** Martina Guidetti

**EDUCATION:** Scientific High School Diploma (2006-2011), Liceo G.B. Vico, Corsico, Milan, Italy

Bachelor of Science in Biomedical Engineering (2011-2014), Politecnico di Milano, Milan, Italy

Master of Science in Biomedical Engineering (2014-2016), Politecnico di Milano, Milan, Italy

Master of Science in Bioengineering (2016-present), University of Illinois at Chicago, Chicago, USA

**WORK EXPERIENCE:** Research assistant (2017-present) for Richard and Loan Hill Department of Bioengineering, Acoustic and Vibrations Laboratory, University of Illinois at Chicago, Chicago, USA